Biomechanical Modeling and Simulation of Human Eye Movement

BY Qi Wei

A dissertation submitted to the

Graduate School—New Brunswick

Rutgers, The State University of New Jersey

in partial fulfillment of the requirements

for the degree of

Doctor of Philosophy

Graduate Program in Computer Science

Written under the direction of

Dinesh K. Pai

and approved by

_____

_____

_____

_____

New Brunswick, New Jersey

January, 2010

ABSTRACT OF THE DISSERTATION

Biomechanical Modeling and Simulation of Human Eye Movement

by Qi Wei

Dissertation Director: Dinesh K. Pai

Studying human eye movement has significant implications for understanding the oculomotor system and treating vision disorders. Existing models of the oculomotor system either simplify the geometry and mechanics of the orbit, or are restricted to static simulation. In this dissertation, we present a novel three-dimensional (3D) biomechanical modeling framework for simulation of the oculomotor plant that addresses the above limitations. We aim to lay the foundation of a biomechanical simulator that will potentially be used for scientific research on ocular motility and clinical applications.

We first propose an efficient method for building subject-specific orbit models from magnetic resonance imaging (MRI). We reconstruct 3D geometric models of the orbit by fitting a generic template model to the MRI data of individual subjects. An automatic fitting process is developed, which combines parametric surface deformation with image feature selection. The accuracy of our

method is validated by comparison to manual segmentation. We also present 3D reconstruction of eyeball models from MRI using the template approach with subdivision surface fitting.

We then describe a new approach for determining the averaged longitudinal strains of cylindrical soft tissues. Our method does not rely on image features to establish tissue correspondences and uses the incompressibility property of soft tissues. We demonstrate its usefulness by estimating extraocular muscle (EOM) strains from reconstructed models. Simulated sensitivity analysis and validation on MRI of a rubber phantom show its accuracy. Integrating estimated EOM strains as deformation constraints, we register EOM models across eye positions in a physically consistent way.

Finally, we develop a 3D dynamic biomechanical model for simulating ocular motility. We model EOMs as "strands," which are modeling elements for musculotendon mechanics. Realistic muscle paths and cross sectional areas of the EOM strands are based on 3D geometric models reconstructed from human subject MRI. Nonlinear EOM mechanics are incorporated and pulley hypotheses are implemented. Simulation of fixations, smooth pursuits, and saccades are demonstrated. The model generates realistic gaze trajectories from neural control signals. We validate our simulator by comparing simulations to experimental data. Our model is the first one that simulates dynamics and includes anatomical and physiological properties.

Preface

Portions of this dissertation are based on work previously published or submitted for publication by the author [Wei and Pai, 2008; Wei et al., 2008, 2009; Wei and Pai, 2009; Wei et al., 2010].

Acknowledgements

My earnest acknowledgement goes to my advisor Professor Dinesh Pai. This dissertation would not have been possible without his supervision and support. Dinesh has been a wonderful mentor of me for many years, both in research and in life. He guided me every step throughout this journey and gave me very helpful advice whenever I needed his opinions. He always believes in me when I have doubts in myself; he continually encourages me to take on new challenges to accomplish more that I had thought I could. He taught me to be confident, motivated, persistent, and perseverant to achieve goals. He taught me how to communicate and how to present work effectively. I learnt much from him on how to be a serious researcher and many things about life. I greatly appreciate that he led and inspired me into these exciting research areas which I will benefit in my future career.

I would like to thank my thesis committee members, Professor Peter Meer and Professor Ahmed Elgammal, for their support, insightful comments, and generous recommendations. I also want to thank Dr. Joseph L. Demer and Dr. Joel M. Miller for their advice. They provided me invaluable insights and data, taught me knowledge of the eye, and sent me timely feedbacks. It has been a privilege and great experience collaborating with them.

I give my sincere gratitude to my labmates: Shinjiro Sueda, Timothy Edmunds, Sang Hoon Yeo, Paul Kry, Danny Kaufman, Subarna Sadhukhan, and the UBC SSL members, for their companionship through my graduate study.

The first two years at Rutgers were the most memorable: freesbie, Siggraph deadlines and trips, Knight demo, and many other lab activities. I am lucky to be a friend of them and be a member of the lab. They are the best labmates one can ever ask for. In particular, I want to acknowledge my long-time research partner and close friend, Shin, who contributed greatly to make this dissertation possible.

I give a special thanks to Xin He, Yingshu Li, Juan Li, and other friends at Rutgers and UBC for their friendship, encouragement, and help.

I am especially grateful for my parents, Jianping Wei and Yuqing Peng, who have brought me up to be the person I am. They have been with me every step of the way and give me unconditional love and support. They instill in me the confidence that I am capable of doing things I put my mind to. I also thank my dearest sister, Wansu Wei, for her love by all means.

The most fascinating thing that happened during my Ph.D. study was that I got married to Fei Li. He always reminded me the luxury of being a student and thus to cherish the opportunity. From his own experience, he showed me the importance of working hard to truly experience the journey other than simply anticipating the result. He believes in me, even more than myself; he knows more about me, even more than myself. His love, support, humor, and determination have made completing this dissertation easier and more enjoyable.

Dedication

I dedicate this dissertation to my parents, Jianping Wei and Yuqing Peng, and to my husband Fei Li.

Table of Contents

List of Tables

List of Figures

List of Algorithms

Chapter 1
Introduction

Vision is one of our most important senses. Rapid and accurate eye movements are crucial for coordinated direction of gaze. Many kinds of disorders that impair human vision are associated with pathological eye movements. Understanding how the eye moves is driven by the demand for better treatment for these diseases. For instance, *strabismus*, or binocular misalignment, is a common visual defect in which two eyes do not look at the same point at the same time when focusing. Approximately 4 percent of the U.S. population suffer from strabismus [AAPOS].

Each eye has six muscles, called the *extraocular muscles* (EOMs). Strabismus is typically caused by uncoordinated extraocular muscles. Strabismus can be treated surgically; this involves manipulating the unbalanced EOMs. Because of the difficulty of predicting the mechanical effects of operations, current diagnosis and treatment are mostly based on simple heuristics, intuition, and experience [Miller and Demer, 1999]. As a result, the success rates of strabismus surgeries are not satisfying. Many operational treatments are found ineffective in improving vision, and re-operations are generally required. To advance the knowledge of binocular misalignment and human eye movement in general, much effort has been devoted to reexamine the anatomy and biomechanics of the orbital plant. In particular, the orbital connective tissues have been studied using histology and MRI [Miller, 1989; Demer, 2004, 2007]. Researchers have

found that a 3D computational model of the orbit that realistically represents the anatomical and physiological findings is indispensable in understanding the mechanics and neural control of ocular motility [Haslwanter, 2002; Miller et al., 2003; Demer, 2007].

Computational modeling provides a powerful tool to analyze biological systems, complementary to experimental studies. It aims to build realistic models for individual components of the system to describe the underlying mechanism. Such a model normally employs physical principles and computational methods. Validation is performed through simulation and comparison to the empirical findings. Computational models are not isolated from experimental observations. Incorporating anatomical and physiological properties is critical for their realism and accuracy, and for their utility in scientific studies and clinical applications. In turn, modeling efforts and predictions can provide insights into the structures and aid in the design of better experiments.

Studying human eye movement has other significant implications. The oculomotor plant is an unique mechanical system. It is organized in a seemingly simple way – three pairs of extraocular muscles work as three agonist-and-antagonist pairs and control 3D rotation with three degrees of freedom. However, the oculomotor system exhibits complicated behaviors that are yet to be understood, such as the mechanism behind Listing's law: in head fixed eye movement, the unique ocular torsion in any gaze direction and regardless of the gaze trajectory [von Noorden and Campos, 2001]. How Listing's law is implemented on the globe with noncommutative rotation is under debate [Miller, 2007; Demer, 2007], with the possibility that the cause is mechanical, neural, or both. Surely, any progress on understanding the kinematics and neural control of the eye will aid in the study of other human movements and

in humanoid robots.

1.1 Thesis Statement

A realistic computational model of the human oculomotor plant can be constructed and simulated based on mechanical principles, physiological measurements, and imaging.

1.2 Contributions

In this dissertation, we present several studies on modeling and simulating human eye movement using medical imaging techniques and biomechanical simulators. We aim to lay the foundation of a biomechanical framework for simulating the oculomotor plant, which eventually will be used for clinical applications. Our main contributions and their associations are summarized in Figure 1.1, and are described in the following.

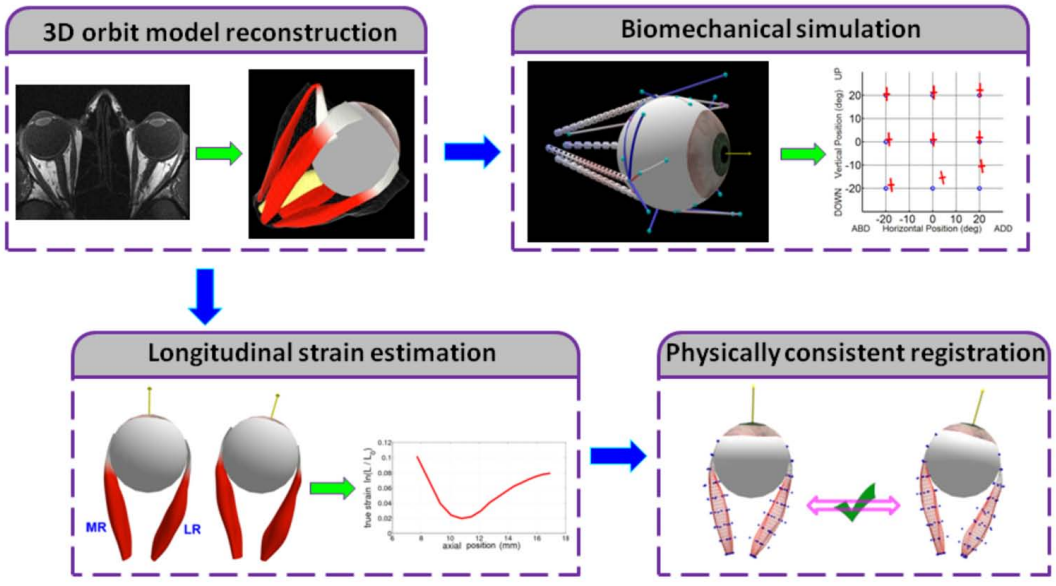

Figure 1.1: Main contributions of the dissertation and their connections.

- Efficient reconstruction of 3D orbit models

  We propose a semi-automatic computational framework to efficiently reconstruct individualized orbit models from Magnetic Resonance Imaging (MRI).

  Advances in medical imaging have greatly benefitted clinical diagnosis and scientific research. Computed Tomography (CT) and MRI have been employed in the diagnosis and evaluation of ocular motility disorders [Gonzales et al., 1986; Demer et al., 1994; Velez et al., 2004; Clark and Demer, 2006; Rutar and Demer, 2009] and anatomical studies [Miller, 1989; Tian et al., 2000; Clark et al., 2000; Kono et al., 2002a; Demer et al., 2003a,b]. MRI has the advantage of excellent soft tissue contrast and of non-invasiveness. Three dimensional imaging provides valuable information about the anatomical features of the intrinsic orbital structures, including the globe [Mutti et al., 2007; Hoerantner et al., 2007] and the extraocular muscles [Demer et al., 1994; Clark and Demer, 2002; Oh et al., 2002; Rutar and Demer, 2009]. MRI scans are becoming routine examinations for diagnosis and treatment planning. Manual image-based reconstruction of the orbital structures is too labor intensive to be practical; automated approaches on the computer will facilitate patient-specific data analysis.

  Our method requires minimal manual work. It combines template-based deformable models with adaptive edge selection. It does not depend on user intervention and is robust with respect to image noise, which makes the approach suitable to generate models for many subjects. The reconstructed geometric models are important for realistic biomechanical simulation of the oculomotor plant. We also demonstrate building detailed

geometric models of the eyeball from MRI automatically, as an application of the reconstruction method. The resulting eyeball meshes are potentially useful for biomechanical modeling and shape analysis in clinical applications.

- Estimation of longitudinal strains

  We present a simple yet effective technique for estimating one-dimensional longitudinal deformation of cylindrical soft tissues.

  Assessing how tissues deforms is important for understanding its mechanical properties and functions. For instance, quantifying the deformation of the orbital layer and global layer of an extraocular muscle at different eye positions can provide evidence for or against the hypothesis that the two layers contract differentially [Miller et al., 2006]. Imaging techniques and physical markers are often employed to study tissue properties. However, with traditional medical imaging modalities, such as CT and MRI, material properties related to movement are hard to resolve either due to the limitations of these techniques or the intrinsic challenges of the target tissues, such as homogeneous intensity. As a result, advanced imaging techniques, such as tagged MRI [Osman et al., 1999] and Magnetic Resonance Elastography [Muthupillai and Ehman, 1996], are required to quantify tissue deformation.

  Motivated by the limitations of existing imaging techniques, we propose a method that does not rely on image features to establish tissue correspondences. It is especially useful for cases where images are inadequate for providing interior tissue features. Our method uses the incompressibility property of soft tissues and is sufficiently general to be applicable

to many tissue types. We apply our approach to analyze extraocular muscle deformation using the reconstructed 3D EOM meshes. The results show inhomogeneity of EOM deformation as a function of eye position.

- Physically consistent model registration

  We describe an algorithm to apply deformation properties during model registration such that the resulting models are physically consistent.

  Typically, geometric models reconstructed independently from different deformed states of the structures only represent the shape variations, and do not show underlying deformation. We enforce deformation consistency constraints in the surface fitting process to regulate positions of the points on the mesh. The registered models are associated with each other by the deformation properties. Mechanically meaningful material correspondences of the models are provided directly. The method can be generalized to create realistic models for biomechanical simulation. Using the reconstructed meshes and estimated longitudinal muscle strains described above, we demonstrate registration of extraocular muscle models at various horizontal eye positions.

- Biomechanical simulation of eye movement

  We develop a new biomechanical simulation framework for studying ocular motility. It is the first biomechanical model that realistically implements extraocular muscle pulleys and simulates dynamics eye movements.

  Several computational models have been developed to improve our understanding of the mechanics and control of ocular motility. Models using simplified anatomical and mechanical properties of the orbit have

been proposed for studying the neural control of saccadic movements [Schnablok and Raphan, 1994; Raphan, 1998; Quaia and Optican, 1998]. In these models, simplifications are made such that analytical solutions can be found. However, these simplifications limit the models' accuracy and thus their usefulness in the study of ocular motility [Quaia and Optican, 2003]. These simplified models are insufficient for use in clinical predictions. On the other hand, biomechanical models that incorporate anatomically realistic muscle paths and empirical EOM innervation-length-tension relationships have been implemented [Robinson, 1975; Miller and Robinson, 1984; Miller et al., 1995; Haslwanter et al., 2005], mainly for planning strabismus surgical treatment through binocular alignment simulation. One drawback of the currently available biomechanical models is that none of them can simulate dynamic eye movements, such as saccades. Our biomechanical simulator addresses the limitations of previous models. By using a novel muscle-modeling primitive, our model of the orbital plant incorporates the nonlinear mechanical characteristics of existing biomechanical models while supporting dynamic simulation. We include realistic anatomy of the EOMs by using subject-specific muscle paths and cross sectional areas provided by the geometric models reconstructed from clinical MRI of patients. Possessing these desired features, our biomechanical model can be used to simulate both static and dynamic eye movements. One of our main contributions is that the model's generality and flexibility allow new anatomical and physiological findings, such as the recently proposed pulley hypotheses [Miller, 1989; Kono et al., 2002a; Demer, 2004], to be included. Such a model will benefit both laboratory studies and clinical surgical treatment.

1.3 Outline

The rest of this dissertation is organized as follows. We first present background on eye movements in Chapter 2. In Chapter 3, we describe our template-based reconstruction approach. We show reconstructed 3D models of the orbit as well as validations of model accuracy. We also introduce a subdivision fitting procedure for building detailed models of the eyeball from MRI. In Chapter 4, we present a longitudinal strain estimation method. To assess the effectiveness and accuracy of the approach, we apply it to real MR images of a rubber phantom and conduct sensitivity analysis using computer simulations. The practical application of the approach is further demonstrated by studying EOM deformation and registering EOM models in a physically consistent way. In Chapter 5, we describe two biomechanical models with different implementation of the rectus muscle pulleys. Simulations of fixations, saccades, strabismus, as well as model validation are presented. Finally, we conclude the dissertation with discussion and plan for future work in Chapter 6.

Chapter 2
Background

In this chapter, I introduce background knowledge on eye movement. It is a big topic and I provide a brief outline on the subject matters relevant to this dissertation. See [Leigh and Zee, 2006] or [von Noorden and Campos, 2001] for more information.

2.1 Anatomy and Physiology

The orbit is a complicated structure. The globe (eyeball) is held in position in the eye socket by ligaments, muscles, and fascial sheaths connected to the orbital wall. Three pairs of muscles insert on the globe and are coupled through complex connective tissues. These six muscles, named the extraocular muscles (EOMs), are innervated to generate force and rotate the globe to reach or track a visual target object and to stabilize the image of the object on the retina. Figure 2.1 shows a 3D model of a human orbit reconstructed from MRI [Wei et al., 2009].

2.1.1 EOM Anatomy and Physiology

The six EOMs include four rectus muscles and two oblique muscles. The four rectus muscles originate from the annulus of Zinn; they course anteriorly, pass through the Tenon's capsule, and insert on the sclera. The muscle lengths of the

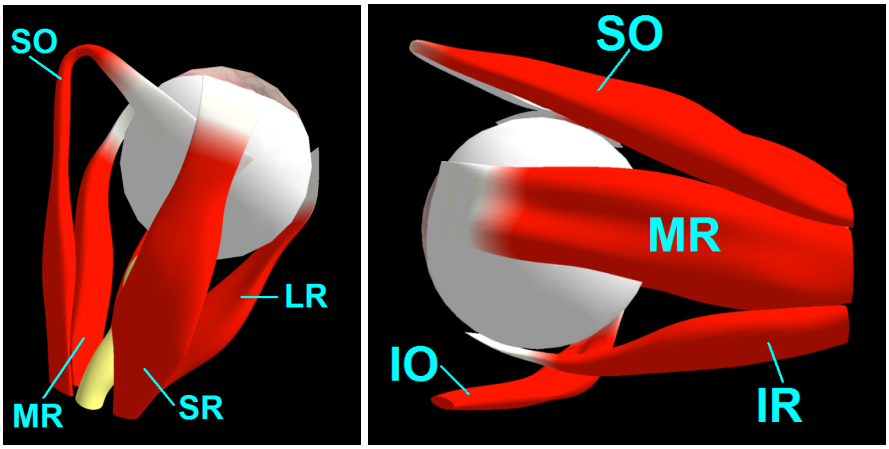

Figure 2.1: 3D model of a human right eye reconstructed from MRI viewed from above and from the medioinferior side.

rectus muscles are all about 37*mm* and the tendon lengths vary between 3*mm* and 7*mm* [von Noorden and Campos, 2001]. The origin of the superior oblique (SO) muscle is on the periorbita of the superonasal orbital wall [Demer, 2007]. The SO tendon passes through the trochlea, a cartilaginous pulley structure attached to the orbital wall, which reflects the SO path inferiorly by 54°. The SO has a long tendon about 30*mm* and its muscle is about 30*mm*. The inferior oblique (IO) muscle originates from the orbital wall anterioinferior to the globe center, courses superiorly, posteriorly, and laterally to its insertion on the sclera posterior to the globe equator. The length of the IO muscle is about 37*mm*; the IO tendon is less than 2*mm* long.

The EOMs are controlled by the cranial nerves. The abducens nerve (cranial nerve VI) innervates the lateral rectus (LR) muscle. The oculomotor nerve (cranial nerve III) innervates the superior rectus (SR), inferior rectus (IR), medial rectus (MR), and inferior oblique (IO) muscles. The superior oblique muscle is controlled by the trochlear nerve (cranial nerve IV).

Two horizontal rectus muscles, LR and MR EOMs, form the horizontal

agonist-antagonist pair. Contraction of the LR produces *abduction* (see Figure 2.2d) – movement in the temporal direction. Contraction of the MR rotates the eye towards the nose; such a movement is called an *adduction* (see Figure 2.2f). Each of the LR and the MR only has one action direction from the straight-ahead eye position.

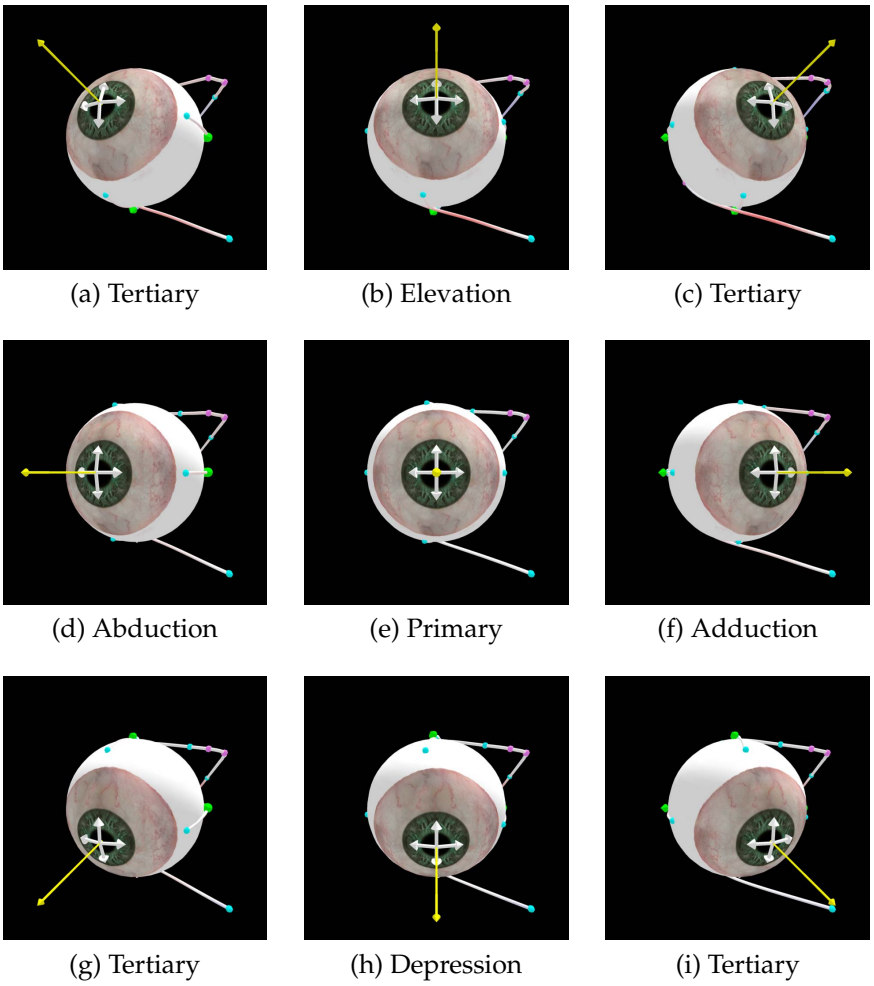

(a) Tertiary (b) Elevation (c) Tertiary

(d) Abduction (e) Primary (f) Adduction

(g) Tertiary (h) Depression (i) Tertiary

Figure 2.2: Primary gaze: (e). Secondary movements: (d) abduction; (f) adduction; (b) elevation (supraduction); (h) depression (infraduction). Tertiary movements: (a); (c); (f); (h).

Vertical eye movement is controlled by the two vertical rectus muscles and

the two oblique muscles. The vertical EOMs are the superior rectus and inferior rectus muscles. SR and IR share a muscle plane that forms an angle about 23° with the median (vertical) plane of the body. SR primarily contributes to *elevation (supraduction)* of the eye while IR mainly contributes to *depression (infraduction)*. See Figure 2.2b and Figure 2.2h for simulated elevation and depression. Contractions of SR and IR also affect eye rotation about the line of sight, called *cycloduction*. The secondary actions of SR and IR cause *incycloduction* (inward rotation) and *excycloduction* (outward rotation) respectively [von Noorden and Campos, 2001]. They also adduct the eye slightly.

The superior oblique and inferior oblique muscles form the third agonist-antagonist pair, which primarily influences cycloduction. Contractions of SO/IO lead to incycloduction/exclyduction. SO and IO also produce depression and elevation respectively as their secondary roles. They contribute to abduction as well.

Accurate eye movement requires cooperative control of the six EOMs. A single EOM never works alone to produce a desired movement. Empirical laws have been proposed to explain this coordination in simple cases with a pair of antagonistic muscles, but it not clear how well the laws generalize to more comprehensive models of the orbit. According to *Sherrington's law of reciprocal innervation*, an antagonist muscle is relaxed when an agonist muscle is innervated. Such interplay between opposing EOMs makes eye movement smooth and steady [von Noorden and Campos, 2001]. Furthermore, due to the anatomical arrangement of EOMs, any vertical gaze involves innervations of both the vertical and the oblique EOM pairs.

Since humans have binocular vision, EOM neural control of one eye is associated with the control of the other eye to produce synchronized movements

of both eyes, except for pathological conditions. *Hering's law of equal innervation* explains such associations – during eye movements, the corresponding muscles in two eyes receive the same amount of innervations.

Global Layer and Orbital Layer

EOMs are bilaminar and consist of two layers with different fiber types [Porter et al., 1995]. The orbital layer (OL) of an EOM is on the outer side, adjacent to the orbital wall. The inner global layer (GL) of a rectus muscle is adjacent to the globe. The GL of the oblique EOMs constitutes the central core [Demer, 2007].

The anterior GL becomes tendinous and inserts on the sclera while the OL terminates posterior to the EOM tendon. The rectus OL inserts on the connective tissue pulleys, important evidence based on which the active pulley hypothesis was developed [Demer et al., 2000].

Pulley Connective Tissues

Pulleys refer to the connective tissues that stabilize the rectus muscle paths even in extreme eye positions [Miller, 1989]. Rectus muscle pulleys are believed to play a significant role in the mechanics and neural control of eye movement [Miller, 2007]. One of the reasons that these mechanically important structures were ignored from orbit anatomy is because they are distributed structures that can only be characterized as condensations of smooth muscles, elastin, and collagen revealed in histological images [Demer et al., 1995; Kono et al., 2002b]. The functional positions of pulleys, identified by the sharp inflections of EOM paths were quantified from MRI studies [Clark et al., 2000; Kono et al., 2002a]. More details about pulleys will be given in Section 5.5.1.

2.1.2 Eye Movements

When the eyes are looking straight ahead, that position is named the *primary position* (see Figure 2.2e); a mathematically precise definition can be found in [Tweedw et al., 1990]. Pure horizontal or vertical eye rotations are called *secondary positions*. Gazes with both horizontal and vertical components are *tertiary gazes* (see Figure 2.2a for an example). There are five basic types of eye movements.

During **fixation**, the eyes maintain the gaze on a single target. However, eyes are never completely stationary. Microsaccades – are small and involuntary saccades – and ocular drifts are usually involved in fixational eye movements.

A **saccades** is the rapid eye movement that we make to quickly change visual attention from one target to another. A saccade brings the image of the target to the fovea, which has the highest concentration of photoreceptors on the retina and provides the best visual resolution. Saccades are the fastest movements of human body and can reach $1000^{\circ}/s$. Due to the high speed, vision is blurred during the execution of a saccade.

When an eye is following a slowly moving target, the motion is called a **smooth pursuit**. The eyes try to foveate the image of the target continually during pursuit. Pursuit is often accompanied by catch-up saccades and is driven by visual feedback.

The above eye movements are *conjugate* movements, during which two eyes rotate the same angle in the same direction. When the two eyes move in the opposite directions, a *disjunctive* movement, or **vergence** occurs. Inward

vergence is called *convergence* and outward vergence is called *divergence*. Tracking an object who's distance from the viewer varies involves vergence movement.

Vestibular-ocular movement is a reflex eye movement that does not depend on visual feedback. Its function is to stabilize the retinal image of a stationary target being fixated while the head is moving using inertial sensors for head movement called the vestibular organs. The eyes involuntarily move in the opposite direction as the head moves in order to compensate for the head movement.

2.2 Strabismus

Strabismus, or *squint*, is the misalignment of two eyes due to dysfunction of extraocular muscles and/or lack of coordination among them. The cause of strabismus is complicated. It could be innervational, mechanical, or a combination of both.

A visual axis refers to the vertical or horizontal axis of the eyeball that is on the equatorial plane. Characteristics of the visual lines (lines of sight) and visual axes are used to accurately describe orientation of the eyes [von Noorden and Campos, 2001]. In normal cases, visual lines are parallel in distance fixation and properly converged in near vision. Strabismic eyes are subject to deviation of the visual axes and visual lines. Based on deviation direction, strabismus can be classified into various kinds.

- **Horizontal deviation.** *Esotropia* refers to the convergence of the vertical visual axes and *exotropia* refers to the divergence of the visual axes. Two examples are illustrated in Figure 2.3:A and Figure 2.3:B.

- **Vertical deviation.** If the visual line of the left/right eye is higher than the right/left, the left/right eye is said to have *hypertropia* (see Figure 2.3:C). *Hypotropia* defines the situation when the visual line is lower in one eye than the other (see Figure 2.3:D).

- **Cyclodeviation.** Clockwise mis-rotation about the visual line causes *excyclotropia*; counter-clockwise rotation leads to *incyclotropia*. See Figure 2.3:E and Figure 2.3:F.

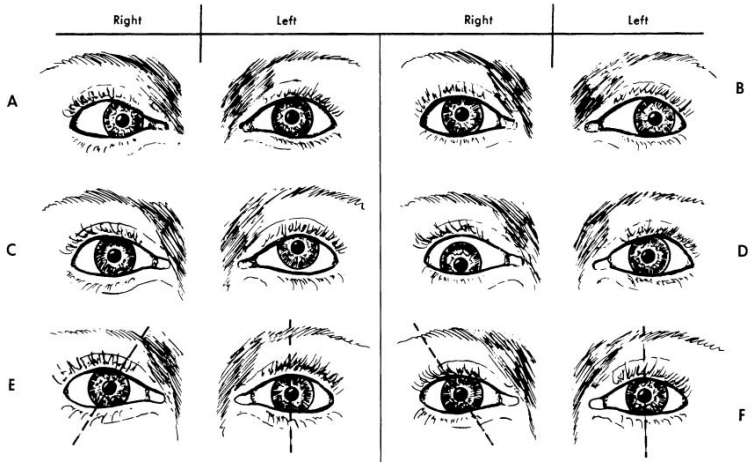

Figure 2.3: Classification of strabismus by direction of deviation (illustration from [von Noorden and Campos, 2001]). A: Right esotropia. B: Left exotropia. C: Left hypertropia. D: Right hypotropia. E: Right incyclotropia. F: Right excyclotropia.

Strabismus is also classified into *comitance* and *incomitance* by the deviation pattern. Incomitant strabismus exhibits varying deviation angles in different eye positions. Paralytic extraocular muscles typically cause incomitant strabismus; the deviation is more dramatic in the major acting direction of the underacting muscle. Deviation of comitant strabismus is constant in all eye positions. Comitant strabismus is primarily due to causes other than anatomical and mechanical pathologies, such as generic factors, innervational defects, uncorrected refractive errors, etc. [Lang, 2000]

Chapter 3
3D Reconstruction of the Orbit

3.1 Introduction

In this chapter, we present a template-based approach to building subject-specific models of the human orbit (the contents of the eye socket, including the extraocular muscles that move the eye) from magnetic resonance images. Our goal is to build subject-specific geometric representations of ocular structures efficiently and accurately, with minimal manual work.

Motivations

Modern imaging techniques, in particular MRI, make the evaluation of abnormalities of orbital structures of alert humans possible and thus have been used in clinical diagnosis. Quantitative morphometric analysis of EOMs using MRI can be used in the objective diagnosis of superior oblique (SO) muscle palsy [Demer et al., 1994; Demer and Miller, 1995]. Cross sectional areas can be measured from coronal images that reveal the size and contractile changes of SO. Patients with SO palsy normally have smaller SO size and show abnormal contractile changes. High resolution MRI in alert humans combined with computer simulation has shown that heterotopic pulleys, i.e., pulleys with abnormal positions, can account for incomitant strabismus [Clark et al., 1997, 1998].

Previous studies have employed MRI to quantify the size and shape of eyeballs [Atchison et al., 2005; Singh et al., 2006]. One of the interesting findings is that the axial length of an eyeball increases as the degree of myopia increases [Atchison et al., 2005]. Such observations and further investigations are useful for interpreting ocular imaging and better understanding myopia and refractive errors.

Current analysis is mainly done manually, which is time consuming and inconsistent due to the dependence on human operators. Reconstructing patient specific 3D models of the orbit from medical images on a computer will greatly aid in ocular disorder diagnosis, as many key characteristics can be inferred directly from these models.

Efficient and accurate orbital model reconstruction also has important applications in assisting the planning of surgical treatment with individual patients. Associated with biomechanical properties (innervations, contractile forces, elasticities, etc.), these models can be used to simulate patient-specific disorders. Using appropriate biomechanical simulators, such as the ones introduced in Chapter 5 and others developed previously [Miller et al., 1995; Haslwanter et al., 2005], ophthalmologists can apply surgical manipulations on the models to predict surgical outcomes and gain insights on effectiveness of operations.

Reconstruction of the orbit has been studied previously. Li et al. [2002] developed a system that generates 3D models by assisting the user with the time-consuming task of segmenting 2D contours of the orbital structures from MRI. Even with the tools provided, this frame-by-frame image-based reconstruction process is prohibitively expensive for anything other than a research study. In addition, due to the geometric representations they use, the reconstructed models lack sufficient resolution and do not have smooth shapes. Miller et al.

[2003] produced 3D reconstructions of orbital tissues using different types of images, including MR images and histological images. The strong structures in the orbit as well as other important connective tissues were reconstructed. However, their technique involves significant manual segmentation and feature identification, making it difficult to generate many subject-specific models. The surfaces for generating the finite element meshes in [Schutte et al., 2006] were also built from manually traced contours.

In summary, previous approaches of orbit reconstruction are based on time-consuming manual image segmentation. We develop a semi-automatic computational framework for building subject-specific models of the orbit from MRI efficiently. The template surfaces are adaptively fitted to the refined feature points selected by using 3D spatial information and 2D image intensity. Our surface fitting approach is a variant of the iterative closest point (ICP) algorithm. See [Rusinkiewicz and Levoy, 2001] for a review of ICP variants. We use an automatic point selection algorithm to define the closest points in each iteration. The "closeness" depends not only on Euclidean point-to-surface distances but also on regional textures.

Outlines

In Section 3.2, we first review related work in 3D model reconstruction. We present the details of the proposed approach in Section 3.3. In addition to showing reconstructed orbit models of different normal subjects in Section 3.4, we demonstrate the clinical application of the framework to studying pathological subjects with geometric abnormalities. We also evaluate the accuracy of the reconstruction by comparing our results with manual segmentation. Understanding the mechanisms of eye movement is difficult without a realistic,

biomechanically complete model. In Section 3.4.4, we discuss how to build individualized biomechanical models of the orbit from reconstructed three-dimensional meshes. The resultant models can be used in physically-based simulations to test various scientific hypotheses, predict surgical outcomes, and improve our understanding of the orbital motility. Finally, in Section 3.5, we present 3D reconstruction of detailed models of the eyeball from MRI using the template approach with an additional procedure – subdivision surface fitting.

3.2 Related Work

Methods for 3D reconstruction from volumetric data can be broadly categorized into two types: *primitive-based* and *model-based*.

Low-level primitive-based reconstruction does not assume any prior knowledge of the topology of the structure being reconstructed. It is a bottom-up approach and generates surfaces from the (normally dense) surface primitives. Shape recovery from 3D range data such as a point cloud (which is a set of unorganized vertices) [Hoppe et al., 1992] and range images [Reed and Allen, 1999] has been studied extensively. Methods based on radial basis functions (RBF) [Hoppe et al., 1992], mesh sweeping [Reed and Allen, 1999], Voronoi Diagram and Delaunay Triangulation [Edelsbrunner and Mucke, 1994; Amenta et al., 32], and level sets [Zhao et al., 2001] have been investigated. Reconstruction of tissues from medical image data normally involves segmenting boundaries in image slices and building surfaces from a stack of contours [Li et al., 2002]. Marching Cubes is a commonly used algorithm that extracts isosurfaces from volumetric data [Lorensen and Cline, 1987]. This approach is straightforward and practical for objects with complex topological structures.

However, the resultant meshes usually contain too many vertices and have topological consistency problems [Treece et al., 1999]. A general problem with primitive-based generative reconstruction is its inability to achieve consistent representation across many data sets unless parametrization or remeshing is performed post processing [Treece et al., 1999].

Another powerful tool is model-based reconstruction that uses deformable models. Our method falls into this category. The basic idea is to use known shapes as prior knowledge to bootstrap the solution. Instead of generating the model from low-level image primitives directly, a template is first created to encode the generic geometric and topological information of the object being reconstructed. The template is then deformed to generate the model fitted to the data. Model-based methods are more efficient for producing a series of models of similar shapes. They are robust to image noise, but implementation can be more complicated. Deformable models [Kass et al., 1987; Terzopoulos et al., 1987; Metaxas and Terzopoulos, 1993], which are based on physical elasticity theory, have been successfully applied in medical image segmentation, registration, and reconstruction [McInerney and Terzopoulos, 1996]. They initiate the development of top-down model-based approaches incorporating prior knowledge with local constraints in shape reconstruction [McInerney and Terzopoulos, 1996]. Statistical anatomical atlases, which model average shapes and the most significant variations of tissues named the principal modes, have been applied in image registration [Chen et al., 2000; Sadowsky et al., 2007]. By deforming initially constructed organ meshes to manually identifies tissue boundaries through some intermediate trivariate tensor volumes, Fernandez et al. [2004] described building anatomically-based finite element geometric models of the musculoskeletal systems. Our approach combines parametric

surface fitting studied in digital geometry processing [Liu et al., 2005] with an automatic edge point selection algorithm. These two steps alternate until a satisfactory model is achieved. We do not use the commonly employed image gradient to guide surface deformation but the selected edge points.

Segmenting multiple objects from image data is non-trivial. Two-dimensional segmentation approaches using multiple *active contours* have been proposed. These models deform to boundaries [Srinark and Kambhamettu, 2004] or are combined with local spatial information and global intensities [Huang et al., 2004; Xie et al., 2002]. Gilles et al. [2006] presented a framework that uses multi-resolution simplex meshes to segment 3D models through simulation. It is a complicated system designed for musculoskeletal systems, with structures in contact with each other and complex attachment constraints. All the structures are solved simultaneously in a global setting. In our proposed approach, we take advantage of the fact that extraocular muscle (EOM) bellies are not in close contact with each other. Thus, our method is efficient to treat EOMs individually, distinguish nearby structures by distances and intensities, and fit them iteratively to updated edge points.

3.3 Methods

Figure 3.1 shows an overview of our template-based reconstruction framework. We first build a template model of the orbit consisting of the orbital wall, the globe, the optic nerve, and the six extraocular muscles (EOMs). Our template-based reconstruction approach is motivated by the observation that, except in rare abnormalities and following certain unusual surgical procedures, the topological relationship of the extraocular structures is fixed. Therefore, if we can build a template model defining the average anatomical and structural

properties of the orbit, we can fit this carefully constructed template to MR images of a new subject by deforming it to model individual variations. Using the template to define prior knowledge of the orbital anatomy is efficient and robust for building individualized models. We develop an iterative computational procedure for generating subject-specific models using the template. As shown in Figure 3.1, our method involves deformable surface fitting to a dense point cloud and adaptive feature selection.

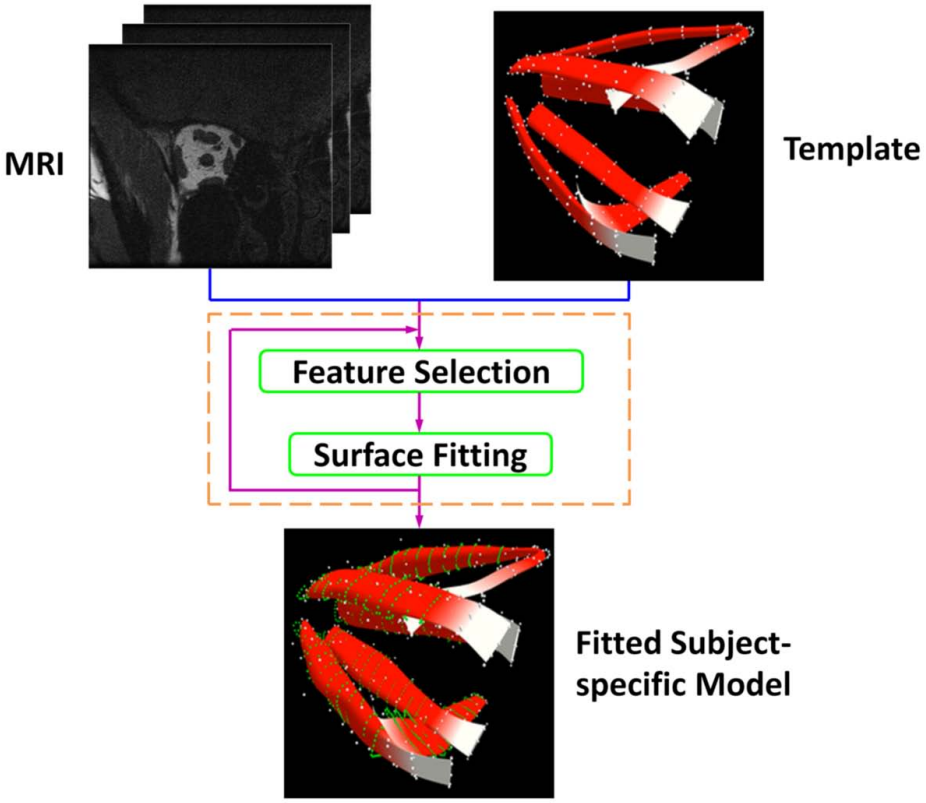

Figure 3.1: Overview of the template-based reconstruction approach.

Build Template Model of the Orbit

We use a uniform bicubic B-spline surface as the geometric representation for modeling the orbital structures, considering its smoothness and continuity, efficiency in modeling and computation, and suitability for simulation. B-spline

surfaces are parametric tensor product surfaces and their basis functions are the products of two univariate functions with interval domains. A uniform bicubic B-spline surface is defined as

$$D(u, v, P) = \sum_{i=0}^{3} \sum_{j=0}^{3} P_{i,j} B_i(i) B_j(v), \tag{3.1}$$

where $P_{i,j}$ is a set of sixteen control points called the *control mesh* for the surface, and B_i is the i^{th} cubic B-spline basis. The four basis functions are

$$\begin{aligned} B_0(u) &= \frac{1}{6}\left(-u^3 + 3u^2 - 3u + 1\right), \\ B_1(u) &= \frac{1}{6}\left(3u^3 - 6u^2 + 4\right), \\ B_2(u) &= \frac{1}{6}\left(-3u^3 + 3u^2 + 3u + 1\right), \\ B_3(u) &= \frac{1}{6}u^3. \end{aligned} \tag{3.2}$$

$D(u, v, P)$ is a weighted sum of the control points with the basis functions as the weights. B-spline surfaces provide inherent smoothness and C^2 continuity. They are also computationally efficient since we only need to compute the positions of the control points, and the surface patches can be evaluated via Equation 3.1. For more details about B-spline surface computation, see [Cohen et al., 2001].

The template of the orbit is constructed based on standard textbooks [von Noorden and Campos, 2001; Moore and Dalley, 1999] and the Orbit^{TM} model in [Miller et al., 1995]. 3D modeling software, Autodesk Maya, is used to build the template shown in Figure 3.1. Except for the superior oblique (SO) muscle, each EOM is represented by a cylindrical B-spline surface with seventy-two control points arranged around nine rings. The SO muscle passes through the trochlea and bends at an acute angle about 54°. More control points are needed to model SO's irregular shape especially near the trochlea. In total, ninety-six control points are used for the SO muscle.

Fit Template to Subject Image Data

To build subject-specific models, the template is fitted to MR image by deforming the template meshes to fit the edge points of the extraocular structures. Considering the anisotropic 3D image resolution (slice resolution 2.0mm vs. image resolution 0.3125mm), we decided not to use the commonly employed image gradient to guide mesh deformation. Instead, we develop an automatic edge point selection algorithm and incorporate it in the iterative fitting process. Given the mesh configuration solved from the previous iteration, edge points that most likely belong to one structure are chosen based on their Euclidean distances to the mesh and regional image intensities. Doing so, we avoid time-consuming manual segmentation of the EOM contours.

The proposed reconstruction algorithm is outlined in Algorithm 1 and described in details as follows.

- **S**tep 1-2 in Algorithm 1

  Given a new subject, a global registration is performed at the beginning. The registration scales, rotates, and translates the template to align roughly with the image data. Currently this step is done manually. Then the Canny edge detector is applied to each image to compute all the feature candidates. The Canny algorithm consists of multiple operations to optimally detect edges in an image [Canny, 1986]. We use the Matlab implementation of Canny edge detector and set the two parameters "THRESH" and "SIGMA" to 0.125 and 0.8 through our experiments. The edges are transformed into the 3D patient space using the magnetic resonance (MR) sequence parameters in the image headers. Some of these

Algorithm 1 Template-based EOM reconstruction algorithm

```
1: Register template meshes initially
2: Acquire all possible edge candidates and transform them to 3D
3: for each EOM X_i do
4:    for iteration t do
5:       Compute point-to-surface distances
6:       Discard distant points
7:       for MR image d do
8:          Pick three good edge points
9:          while there is any unchecked edge point c_k do
10:            if adding c_k results in a convex texture similar to the prior then
11:               Accept c_k
12:            else
13:               Discard c_k
14:            end if
15:         end while
16:         Remove interior edge points
17:      end for
18:      Compute new positions of the control points (Equation 3.7)
19:      Update control points (Equation 3.9)
20:   end for
21: end for
```

edge points are on the contours of the structures that we are not interested in or from noisy edge features caused by the imaging process. Our strategy is to pick the most likely features automatically using some fair metric and deform the mesh to fit to these data points in the least squares sense at each iteration. Both false positives and false negatives in edge selection may occur during earlier iterations. Nevertheless, as the alternation of the two steps goes on, the mesh deforms closer to the actual position and feature selection becomes easier and more accurate.

- **S**tep 5-6 in Algorithm 1

  EOM meshes are reconstructed separately, and their edge points are selected independently. Two criteria are considered for point selection:

3D point-to-surface distance and *regional image intensity statistics*. First, we compute the distances of all the points to each EOM B-spline surface, X_i. Only those points with distances smaller than some threshold (2.5mm in our experiment) are passed to the next stage. The 3D distances are used to prune the unlikely points quickly.

- **T**exture analysis in Step 7-17 in Algorithm 1

  These chosen points are further filtered to remove the ones belonging to other nearby structures, such as another EOM or the orbital bone. Here we check edge points in every image using the local image texture information. The EOM image texture prior is learned from the union of several EOM regions in one MR image. The idea is that a true EOM region in the same image data set has similar texture to the learned prior. Our objective is to choose those points that form a convex region having such texture characteristics.

  We adopt the texture representation and analysis presented in [Huang et al., 2004]. In region merging segmentation algorithms, the mean and variance of an intensity distribution are commonly used as the metric to measure the similarity of two regions. Such metric may not be sufficient for MR images since the pixel intensities of one type of tissue may not be homogeneous but vary within some range. To account for this deficiency, we use the Kullback-Leibler (K-L) divergence as the similarity measurement. The K-L distance (or K-L divergence) between two probability distributions f and g is defined as

$$M_{KL}(f|g) = \sum_i f(i) \log \frac{f(i)}{g(i)}. \tag{3.3}$$

  The K-L distance is an asymmetric metric. $f(x)$ denotes the intensity

density from new data, and $g(x)$ is from the learned texture prior. Non-parametric kernel functions are used to robustly model the intensity distribution of the pixels in each region:

$$f(x) = \frac{1}{M} \sum_{j=1}^{M} h_j(x), \tag{3.4}$$

where h_j is a Gaussian kernel function for pixels $p_j (j = 1, 2, \ldots, M)$,

$$h_j(x) = \frac{1}{\sqrt{2\pi}\sigma} \exp\left(\frac{-(x - p_j)^2}{2\sigma^2}\right). \tag{3.5}$$

For small regions where the number of samples is relatively small, using the kernel functions instead of the pixel values is especially useful. The example in Figure 3.2 and Figure 3.3 illustrates the regional intensity analysis based on K-L distances. The non-EOM Region 2 shows similar intensity statistics to the EOM regions 1, 3, and 4 – the mean intensities of Region 1-4 are 48.7, 46.6, 44.0, and 44.8 respectively and the standard deviations are 8.8, 12.2, 9.6, and 10.4 respectively. Therefore, relying on regional intensity means and standard deviations makes it difficult to distinguish Region 2 from others.

Based on the computed intensity densities in Figure 3.3, the K-L distances of Region 2, Region 3, and Region 4 to Region 1 are 0.91, 0.42, and 0.36 respectively. The K-L distances show a clear differentiation of the non-EOM region (Region2) from the true EOM regions. We conclude that K-L distance is an effective metric in classifying EOMs in MRI.

- **S**tep 7-17 in Algorithm 1

  All the points on the same image assigned to one EOM passed from the 3D point-to-surface distance filter are considered for further selection (steps 7-17 in Algorithm 1). We first generate a hundred of triplets of

(a) A coronal image

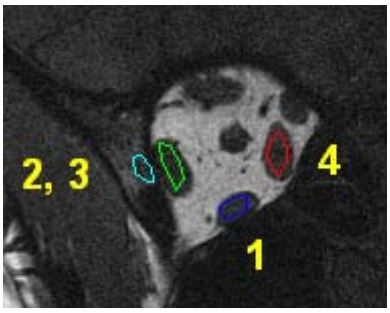

(b) Four regions with similar intensity

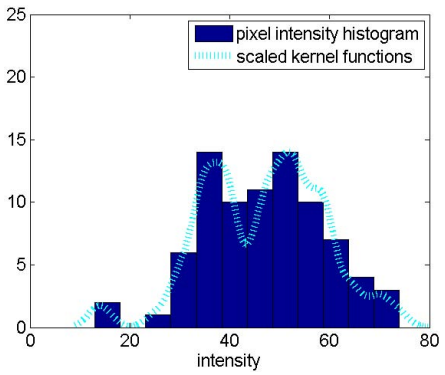

(c) Intensity histogram of Region 2

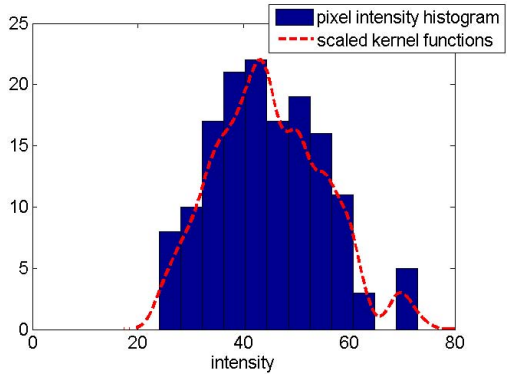

(d) Intensity histogram of Region 4

Figure 3.2: An example showing the texture analysis. (a) A coronal MR image posterior to the globe equator. (b) Four regions with seemingly similar intensity are identified. Region 1 (blue), Region 3 (green), and Region 4 (red) are inside EOMs; Region2 (cyan) is outside the orbital wall but has similar intensity texture to the EOMs. (c) and (d) compare the pixel intensity histograms and intensity densities using kernel functions of Region 2 and Region 4. It is difficult to distinguish Region 2 and 4 by using the intensity mean (Region 2 - 46.6; Region4 - 44.8) and standard deviation (Region 2 - 12.2; Region 4 - 10.4) as the metric.

points by randomly picking three points from all the candidates for each triplet. We then compute the similarity of each triangular area formed by one triplet to the learned texture using K-L distance as the metric. The smaller the computed K-L distance from one triplet is, the more similar the triangular area's intensity texture is to the prior texture. The triplet with the smallest K-L distance is chosen as the initial points to bootstrap

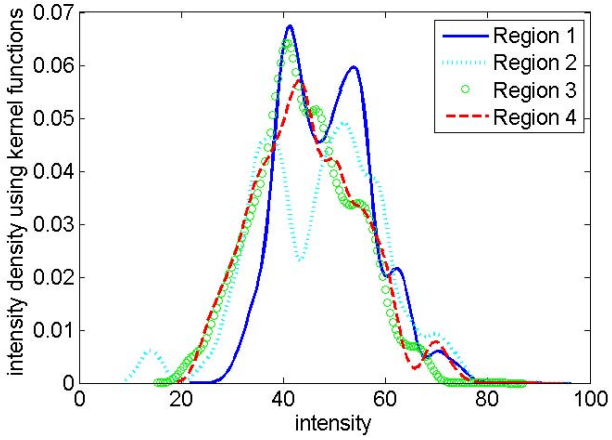

Figure 3.3: Intensity distributions of the four regions in Figure 3.2b.

the selection of more points.

Next, all other candidate points are processed sequentially. When considering a feature point c_k, we calculate the convex hull of the already chosen points and c_k. If the new convex region is sufficiently similar to the texture prior (i.e., K-L distance smaller than a threshold), c_k is accepted. Otherwise, c_k is discarded. Notice that mis-acceptance may happen if c_k is not on the convex hull but located in the interior. In this case, c_k is an interior point but not an edge point, therefore it should not be chosen. However, including c_k does not change the existing convex hull and the original algorithm will still pick it. To detect these interior points, after all the feature points are processed, we apply one more filter by computing the distance from each point to the convex hull formed by all accepted features. If a point is too far from the convex hull (distance larger than 0.2 times the minor axis length of the convex hull), it is discarded. All the points that pass this step are used for surface fitting.

- **S**tep 18 in Algorithm 1

  The contour points provide the discrete details of the EOM surface, and

the parametric template represents the prior knowledge of smooth and continuous shape of the EOM. The objective is to compute the positions of the control points of the template mesh such that the template closely approximates the structure. What needs to be solved is a parametric surface fitting problem, which is normally formulated as a total least squares problem [Pottmann and Leopoldseder, 2003]. The error to minimize is the sum of all point-to-surface squared distances:

$$\min_{P} \sum_{k=1}^{N} ||X(u_k, v_k, P) - c_k||_2^2, \tag{3.6}$$

where $X(u_k, v_k, P)$ is a function of the control points $P_{i,j}$ to be solved. A quadratic term that encourages smooth surfaces [Hormann, 2000] and serves as a regularization term to stabilize the numerics can be added to the objective function. Written in matrix form, the complete objective function is

$$\min_{P} ||AP - c||_2^2 + \alpha F_{smoothness}. \tag{3.7}$$

The elements in the k^{th} row in matrix A are the spline coefficients parameterizing the closest point on the spline surface to a data point c_k. $F_{smoothness}$ is the smoothness constraint based on the surface curvature. α is set to 0.05 in our experiments. We use the simplified thin plate function [Hormann, 2000], one of the commonly adopted approximate energy functions,

$$F_{smoothness} = \int_u \int_v \left(X_{uu}^2 + X_{uv}^2 + X_{vv}^2 \right) dudv. \tag{3.8}$$

Equation 3.7 is solved using the Singular Value Decomposition (SVD).

- **S**tep 19 in Algorithm 1

  At each iteration t, we only update the positions of the control points by

a fraction of the solution $P_{i,j}^t$ solved from Equation 3.7,

$$P_{i,j}^t \leftarrow P_{i,j}^{t-1} + \frac{1}{\omega}\left(P_{i,j}^t - P_{i,j}^{t-1}\right), \tag{3.9}$$

$\omega \geq 1$ is to reduce the influence of the mis-selected edge points in this round and enforces gradual updates. ω is set larger in the first few iterations due to the uncertainty of the selected points. After a few iterations, as the surface deforms closer to the improved feature points, ω is decreased in order to accelerate the fitting process.

Figure 3.4 shows an example of surface fitting. The original template and its deformed configuration are plotted side by side.

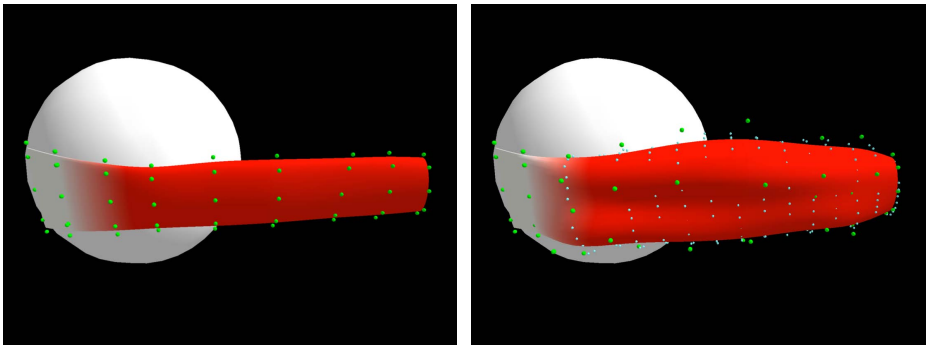

(a) Template mesh (b) Fitted mesh

Figure 3.4: (a) Template B-spline surface of the medial rectus muscle (MR). Green spheres are the control points. (b) MR mesh is deformed to match the selected feature points shown as cyan spheres.

3.4 Results

3.4.1 Reconstruction of Orbital Models

MRI data was acquired at the University of California, Los Angeles. Each subject underwent high-resolution, T_1-weighted MRI scans using a 1.5 T General Electric Signa (Milwaukee, WI) scanner. Multiple quasi-coronal and sagittal

MR images 2.0mm in thickness were obtained using a 256×256 matrix over an 8-cm^2 field of view, giving pixel resolutions of $0.312mm$. Details of the image acquisition protocol can be found in [Clark et al., 2000]. MRI was anonymized and sent to us by Dr. Joseph Demer at UCLA.[1]

Figure 3.5 shows the reconstructed models from two representative subjects from different views (RMS fitting error of $0.370mm$).

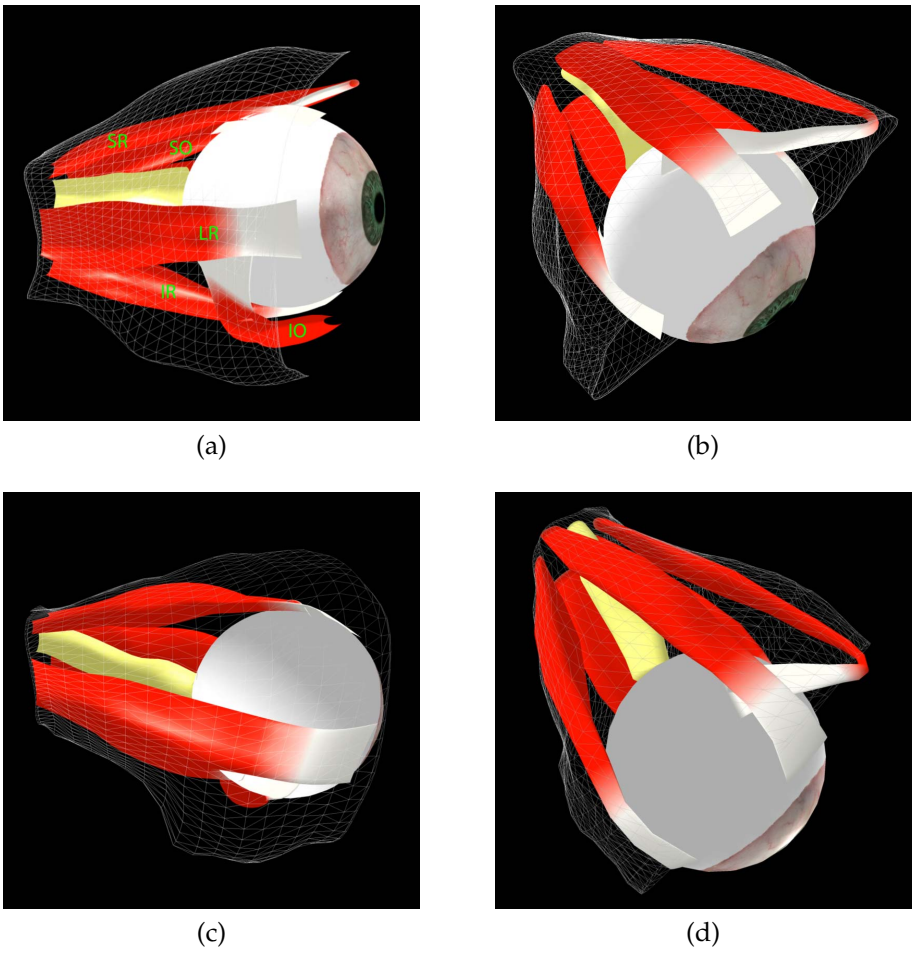

(a) (b)

(c) (d)

Figure 3.5: Reconstructed geometric models of the orbit of two subjects:(a) (b) subject 1; (c) (d) subject 2.

The shape variation of the orbital structures is observed (for example, see

[1] IRB approvals on sharing anonymous data has been obtained at both universities.

the difference of the lateral rectus and superior rectus muscles). The optic nerves are reconstructed in the same way as the EOMs. The orbital wall is represented by a B-spline surface fitted to the edges obtained using the Canny edge detection algorithm followed by fitting active contours with distance forces [Cohen and Cohen, 1993]. The eyeball is approximated as spherical and its center coordinates and radius are fitted using least squares to the boundaries of the globe manually segmented from images. It is difficult to automatically detect the globe boundaries in T_1-weighted MRI, due to the poor contrast between the sclera and EOM tendon. We will describe automatic eyeball reconstruction from T_2-weighted MRI in Section 3.5. Since EOM tendons are hard to segment from images, we use the template geometry directly and gradually blend it to the detectable muscle edge points. In some data sets, EOM contours are segmented manually on one or two images near the equator, where the Canny edge detector fails to find edges between EOMs and the eyeball.

3.4.2 Validation of Reconstruction Accuracy

In order to assess the accuracy of the proposed reconstruction approach, we compare the reconstructed models with manual segmentation obtained from tracing the EOM contours. Since our method produces three-dimensional models of the EOM, we can conveniently obtain the true cross sectional areas at the original imaging planes for comparison. Computer graphics rendering techniques are employed. By properly setting the two clipping planes of the virtual camera, the near plane and the far plane, we display the 3D mesh locally with very thin thickness at desired locations along the medial axis of the mesh. Applied simple image processing operators, cross sectional areas can then be computed from the rendered images.

We choose the Dice coefficient (DC), commonly used in validating image segmentation, to measure the overlap between two areas A and B,

$$DC(A,B) = \frac{2|A \bigcap B|}{|A| + |B|}. \tag{3.10}$$

Figure 3.6 shows the validation results of the horizontal rectus muscles in three subjects at two eye positions, distance and convergence viewing. Each number is the average overlap over a series of images, from which the 3D model is reconstructed. We observe that all muscles have high Dice coefficients over 0.83. This result indicates good agreement of the reconstruction and the manual segmentation. The accuracy of the proposed method is proved.

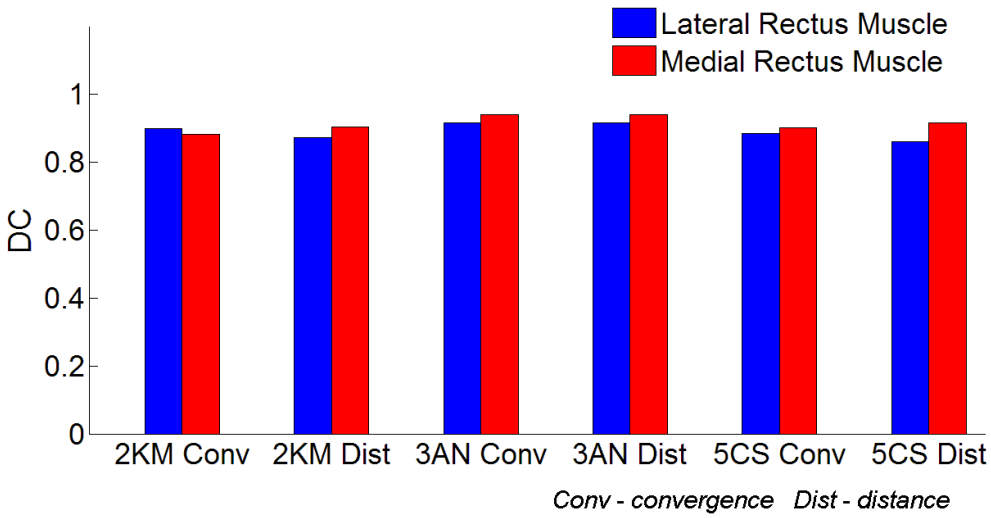

Figure 3.6: Dice coefficients (DC) of reconstructed model to manual segmentation. Analysis is performed on the two horizontal rectus muscles of three subjects during binocular fixation of a target at distance and convergence respectively.

Furthermore, we evaluate the reconstruction accuracy visually in Figure 3.7 by displaying the reconstructed LR and MR muscle models together with MR images in the same coordinate system and checking the intersections. The intersection curves of the model with the MR images match the actual EOM boundaries reasonably well; the usefulness of the proposed framework is proved.

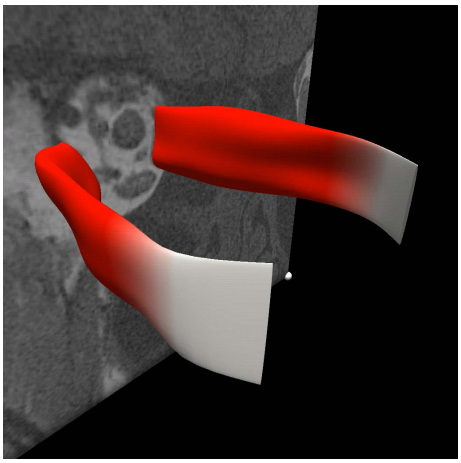

(a)

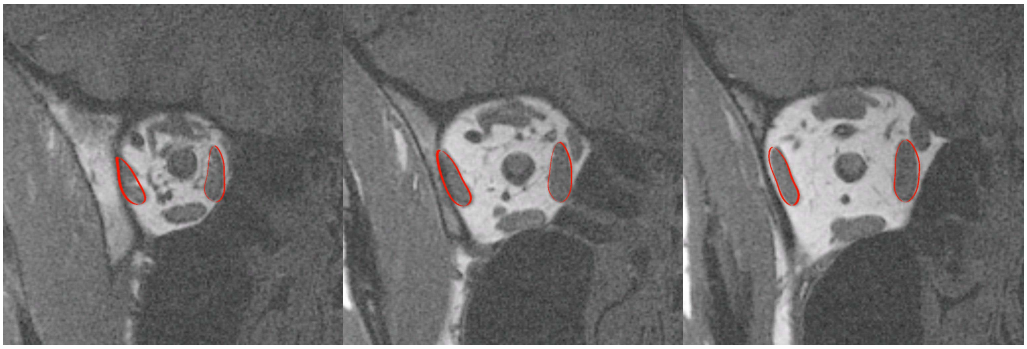

(b) (c) (d)

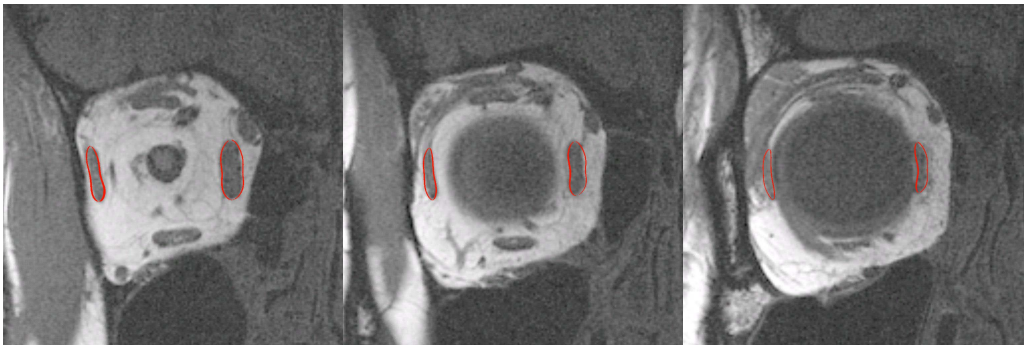

(e) (f) (g)

Figure 3.7: Visual evaluation of reconstruction accuracy. (a) Reconstructed horizontal rectus muscle models are displayed in three-dimensional patient coordinates. Magnetic resonance images are rendered as textures in the same coordinates. (b)-(g) Intersection contours of the 3D models with contiguous 2-*mm*-thick coronal magnetic resonance images from posterior to anterior imaging planes.

3.4.3 Reconstruction of Inferior Sagging Abnormality

Subject-specific models reconstructed from patients with abnormalities can be used for clinical diagnosis and surgical treatment planning. In the following, we use the horizontal rectus muscle inferior sagging (pulley heterotopy) as an example to demonstrate the application of our method.

Previous studies have investigated the inferior displacement of the horizontal rectus muscles due to aging [Clark and Demer, 2006] or degeneration of lateral rectus-superior rectus (LR-SR) band [Rutar and Demer, 2009]. This abnormality may lead to esotropia and hypotropia; its extreme case is associated with the "heavy eye syndrome" [Demer, 2007]. In these studies, centroids of cross sectional areas are analyzed in quasi-coronal MR images.

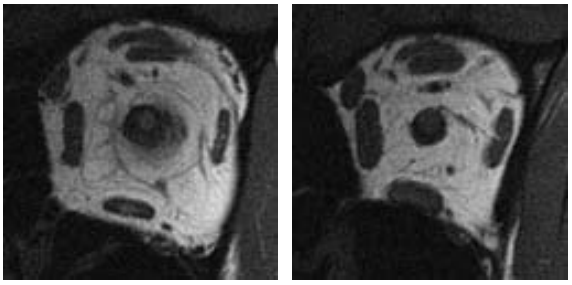

(a) A normal subject

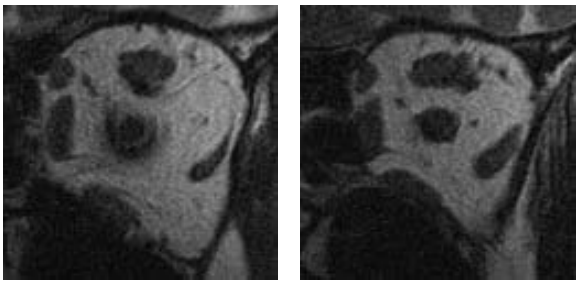

(b) A subject with sagged LR muscle

Figure 3.8: Magnetic resonance images in quasi-coronal planes (on the left) at and just posterior to the globe-optic nerve conjunction in central gaze and (on the right) $4 - mm$ posterior to the globe-optic nerve conjunction. Anonymous MRI was provided by Dr. Joseph Demer.

Figure 3.8 shows MR images of a normal subject and another subject with

inferior sagging of the LR muscle. MR images at two quasi-coronal planes are displayed as representatives. We observe that in addition to the inferior displacement of the LR centroids, the sagged LR muscle exhibits abnormally thinned superior compartment as well as clockwise rotation around its longitudinal axis. These abnormal characteristics may not be revealed by quantifying the centroids only.

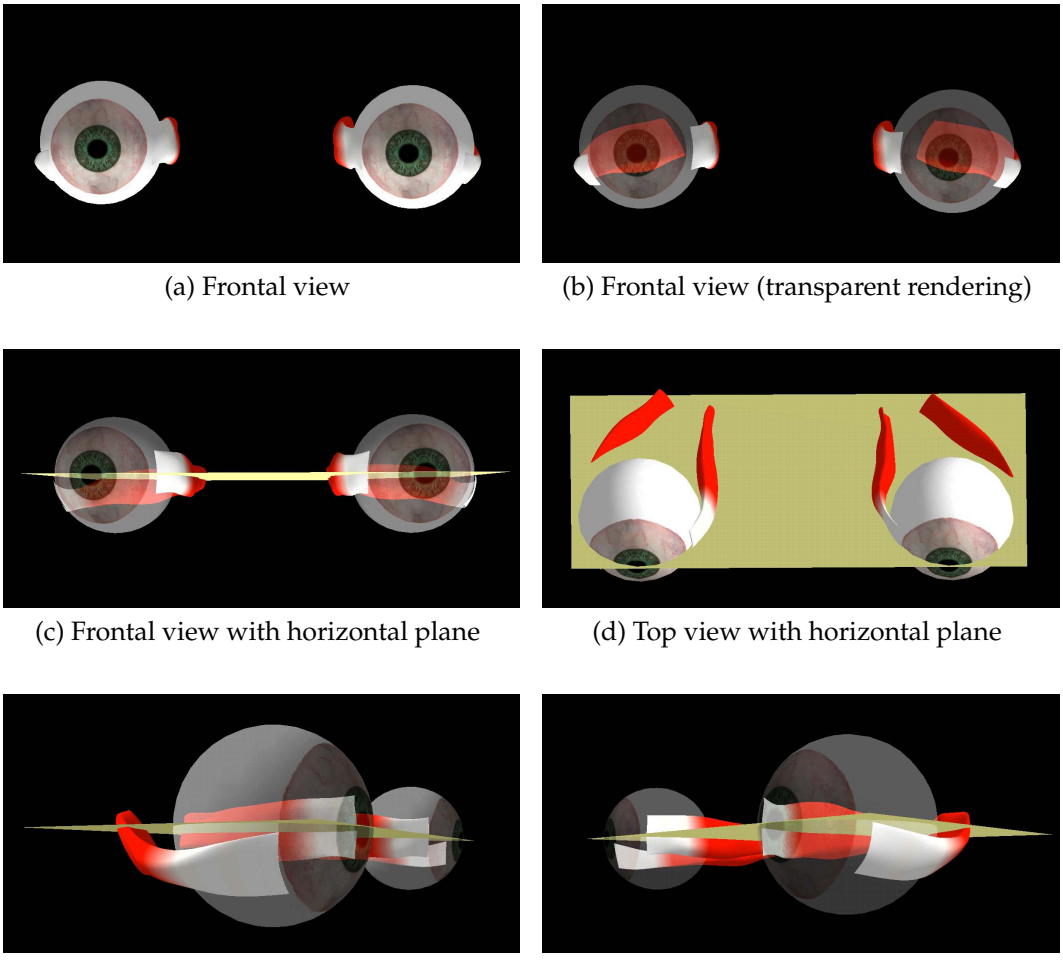

(a) Frontal view (b) Frontal view (transparent rendering)

(c) Frontal view with horizontal plane (d) Top view with horizontal plane

(e) Sagittal view from the right eye (f) Sagittal view from the left eye

Figure 3.9: Reconstruction of a subject with inferiorly sagged LR muscle. Models are rendered in different configurations for better visualization.

We apply our approach described above and reconstruct the 3D models of the LR and MR muscles to visualize this pathological case. The template mesh

of the LR is first manually translated to model the displaced LR path. Then the automated surface fitting procedure is executed. The reconstructed models in Figure 5.30 clearly show the LR geometric abnormalities in both the left eye and the right eye. Sagging starts from the middle parts of both LR muscles.

Quantitative analysis such as the EOM paths shown in Figure 3.10 can also be performed automatically. The maximum inferior displacement is about 5*mm* for both LR muscles.

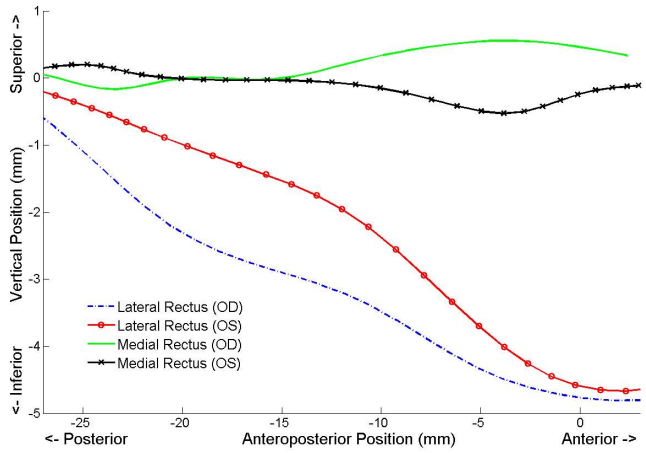

Figure 3.10: Vertical positions of the horizontal rectus muscle of both the left eye (OS) and the right eye (OD) along their paths in the central gaze in the oculocentric coordinate system. Zero position on the horizontal axis (EOM path in oculocentric coordinates) is the globe center.

3.4.4 Building Biomechanical Orbit Model for Simulation

We use the reconstructed geometric models to build biomechanical models for simulation. Finite element models (FEMs) [Schutte et al., 2006] and "strand" models [Sueda et al., 2008] are two biomechanical models that are well suited for studying the biomechanics and neural control of eye movements. Most existing models use simplified geometries and lumped assumptions about the

active force-innervation relationship [Tweed and Vilis, 1987; Schnablok and Raphan, 1994; Quaia and Optican, 1998]. The *Orbit*^{TM} gaze mechanics simulation [Miller et al., 1995] does not have subject-specific 3D shapes or dynamics. In contrast, FEM and strand models can be anatomically realistic and capable of simulating dynamics.

Our modeling framework described in Figure 3.11 eases the development of biomechanical simulators.

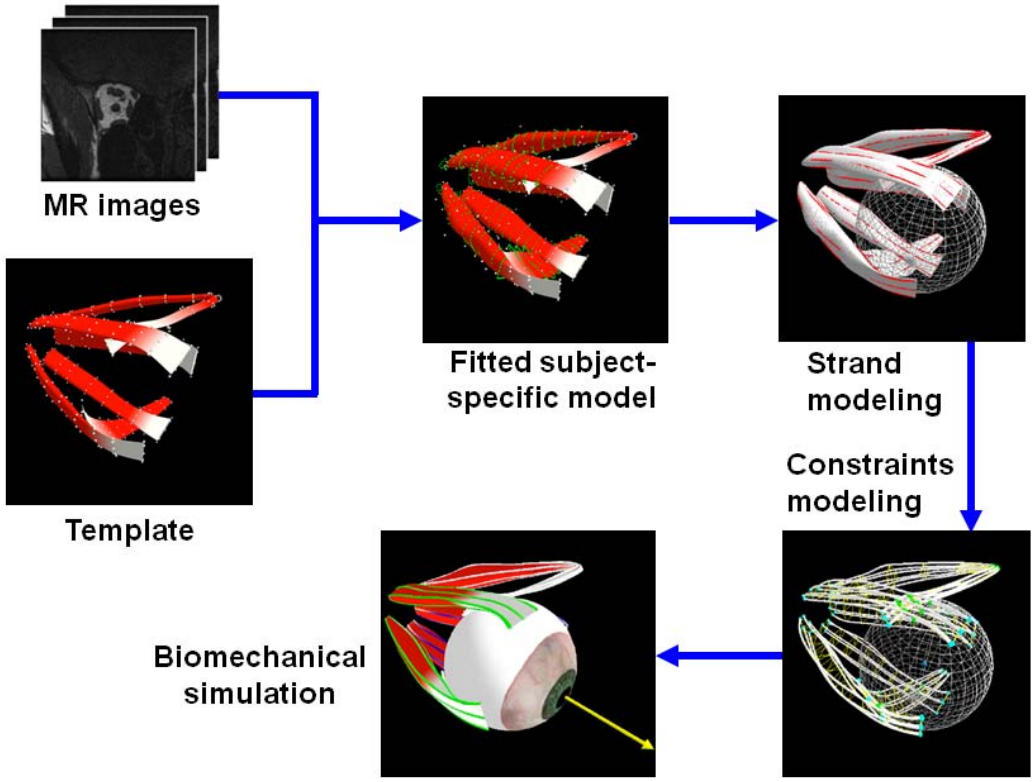

Figure 3.11: Procedure flow to build individualized biomechanical models. Given the reconstructed 3D models, strands are generated automatically to represent realistic EOM anatomy. Mechanical constraints are then specified to define the biomechanical properties of the orbital plant and couplings of the orbital structures. The resulting model is simulated to study eye movement.

Our modeling procedure avoids tedious manual contour segmentation and can generate models of many subjects efficiently. We use the strand modeling primitive as an example. For FEMs, once we have the reconstructed B-spline

surfaces, generating finite element tetrahedral meshes is straightforward. For instance, the commercial software as discussed in [Schutte et al., 2006] or the mesh mapping approach in [Blemker and Delp, 2005] can be applied.

To illustrate the usefulness of subject-specific reconstruction, we describe our approach of automatically fitting strands to subject specific EOMs. The strand-based biomechanical simulation of eye movements will be presented in Chapter 5. Each strand is based on a uniform cubic B-spline curve with associated mass. A point S on a cubic spline is evaluated at its spline parameter t as

$$S(t, P) = \sum_{i=1}^{3} P_i B_i(t), \tag{3.11}$$

where P_i is a set of four adjacent control points and B_i is the i^{th} cubic B-spline basis given in Equation 3.1. By representing each EOM as one or more strands, we incorporate subject-specific muscle path, associate realistic 3D muscle geometry, model tissue interaction, and simulate dynamic eye movements. Using multiple strands interacting with each other by applying volume preservation constraint, larger muscles can be realistically modeled and simulated. We have developed two methods based on different desired configurations to generate multiple strands given a reconstructed mesh. One is to generate strands on the surface, and the other is to model strands inside the muscle. These modeling approaches are not restricted to extraocular muscles; they can be applied to skeletal muscles as well. In the following, we introduce these two methods.

Method One: Model Strands on the Surface

We consider the problem of modeling each EOM as a few strands on the mesh. Specifically, our goal is to position the strands along the direction of the longitudinal axis of the EOM as well as to minimize the distances from the strands

to the mesh. It is also desirable to have the strands distributed uniformly on the surface to achieve a regular representation.

Our approach is straightforward and efficient for generating subject-specific strand models. Initially, the strands are defined directly on a template that has uniformly distributed control points. When the template is deformed to fit the subject image data, the strands on the template are deformed accordingly with the new positions of the control points. The resulting strands are nearly uniformly distributed on the surface due to their initialization and smooth deformation of the control points.

Recall that our template is a cylindrical surface with control-points arranged around a sequence of rings (see Figure 3.12a).

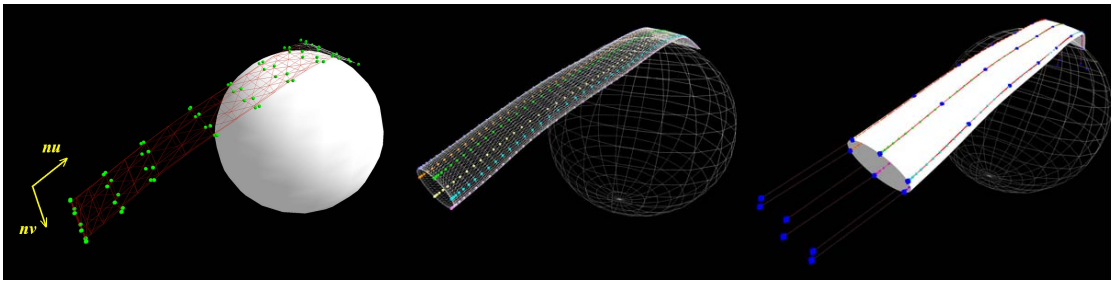

(a) B-spline surface of SR muscle (b) Generated mesh points (c) Fitted strands

Figure 3.12: Model a muscle by six strands ($ns = 6$). (a) The superior rectus (SR) muscle is represented by a cubic B-spline surface ($nrings = 9$; $ncps = 8$). The green spheres are the control points of the surface. (b) The surface is sampled at higher resolution. Six sets of points are extracted, each of which has the same transverse v coordinates. Points in the same set are visualized by the same color. (c) Six B-spline curves are fitted to selected surface points that are on the B-Spline surface. The blue spheres are the curve control points.

We let the number of control point rings on the template be *nrings* and the number of control points per ring be *ncps*. In order to create a strand on the surface, we first need to generate sample points on the surface in the longitudinal direction. A strand can then be fitted to these sample points that are

computed at a high resolution, as shown in Figure 3.12b. Sample point generation is easy because the template is a regular cylindrical surface with control-points arranged around a sequence of rings (see Figure 3.12a). Let the number of strands per EOM specified by the user be ns. For the i^{th} strand, we fix the longitudinal parameter $u = i/ns$ whereas we vary the transverse parameter v to generate a sequence of sample points, X_i, in the longitudinal direction (see Figure 3.12b).

A B-spline curve is fitted to the points in each point set D_i such that the deviation from all points to the curve is minimized. Like the surface fitting problem, this curve fitting can be solved using least-squares. The following objective function is minimized for each spline curve:

$$\min_{P} \sum_{j=1}^{nrings} \parallel S^i(t,P) - X_j^i \parallel_2^2, \tag{3.12}$$

where X_j^i is the j^{th} point in X_i and $S^i(t,P)$ is the closest point on the spline curve S^i to X_j^i.

Figure 3.12c shows the resulting curves fitted to the B-spline surface of the SR muscle in Figure 3.12a. The volumetric deformation of an EOM modeled by strands can be visualized by rendering the bicubic B-spline patches. Each patch is influenced by 4×4 (16) control points from four neighboring strands coupled by volume preservation constraints.

We show the complete strand-based model of subject 1 (in Figure 3.5a) in Figure 3.13. Each EOM is modeled by six strands. Every strand of the rectus muscles and the inferior oblique muscle has 8 control points. The superior oblique muscle has 18 control points to represent its more complex geometry. The strands approximate the reconstructed surfaces closely to a root mean square error (spline to surface) of $0.1mm$.

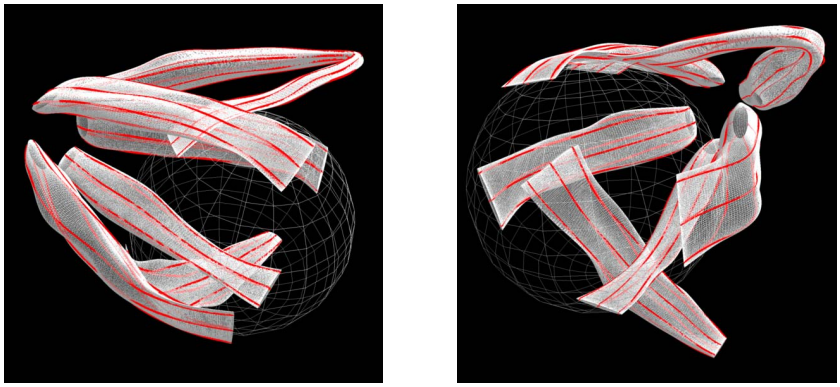

Figure 3.13: A biomechanical model of the orbit using strands fitted to the reconstructed model in Figure 3.5a.

Finally, in Figure 3.14, we show two simulation examples of the strand-based biomechanical orbit model in Figure 3.13 by specifying EOM activations through a Graphical User Interface (GUI). Shortening muscles are visualized in green and lengthening EOMs are in blue. Realistic EOM volumetric deformation is observed.

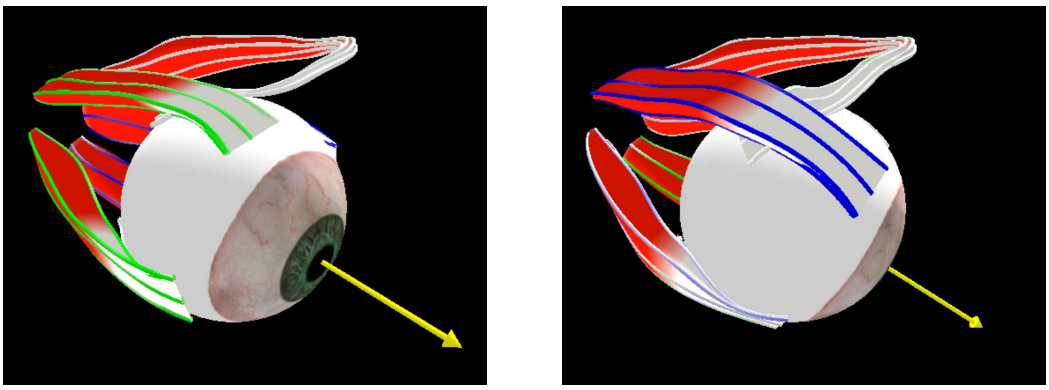

(a) (b)

Figure 3.14: Forward biomechanical simulation of the biomechanical model with manually specified EOM activations. (a) Superior rectus and medial rectus muscles are activated. (b) Inferior rectus muscle is activated. Shortening EOMs are visualized in green and lengthening EOMs are in blue.

Method Two: Model Strands inside the Volume

In this section, we present a solution to the problem of generating multiple strands inside a quasi-cylindrical musculotendinous structure. Given a 3D mesh, our goal is to embed N strands inside the mesh uniformly, along the same direction as the main axis of the mesh (which is the muscle contraction direction). Different from the previous modeling requirement of being on the mesh, we want the strands to spread out inside the mesh as much as possible. Another requirement is to maximize the distance between any two neighboring strands to achieve uniformness. If we think of each strand as a cylinder of some radius, we want to solve the locations of the strands as well as the radius of the cylinder such that the union of these disjoint cylinders covers as much space as possible inside the mesh.

Many problems of this type are NP-hard problems [Baur and Fekete, 1998]. Therefore, we explore practical approximation methods. We propose an approach consisting of two steps. First, we solve a point location problem in 2D. Then, we employ spatial consistency and construct the strands in 3D from those 2D locations.

- **Proposed Approach to 2D Locations**

  Using the graphics rendering technique mentioned in Section 3.4.2, we get local cross sectional contours of the mesh by rendering camera clipping planes. Given these 2D contours, our objective is to solve the desired locations of N data points inside each contour. We develop an algorithm for closed convex contours as it is sufficient for muscles in general.

  We name a convex contour as C. The discrete contour points on C are $Q_k := (x_k, y_k), k = 1, 2, \ldots, m$ in clock-wise order. The inside 2D strand

points to solve are $p_i := (x_i, y_i), i = 1, 2, \ldots, n$. In addition to the position variables, we have a radius variable r for all strands. We define that each strand point has a circular cover area centered at the point itself with radius r. The problem is to solve for the largest feasible r such that three criteria are satisfied simultaneously. First, p_i is inside the convex contour C. Second, every strand point p_i is at least with distance r away from all the contour points. Third, these circles do not overlap. Mathematically, it can be formulated as an optimization problem,

$$\begin{aligned} & \max(r) \\ s.t. \quad & p_i \text{ is inside } C, \\ & D^2(p_i, p_j) \geq (2r)^2, \\ & D^2(p_i, Q_k) \geq r^2, \end{aligned} \tag{3.13}$$

where $i, j = 1, 2, \ldots, n, i \neq j, k = 1, 2, \ldots, m$.
$D(p_i, p_j) = \sqrt{(p_{i_x} - p_{j_x})^2 + (p_{i_y} - p_{j_y})^2}$ is the 2D Euclidean distance function of two points, p_i and p_j.

There are many algorithms to determine if a query point is inside a polygon. Since we assume the contour is convex, we add linear constraints using the contour center to enforce that the points stay inside the contour. We compute the center of mass $c := (c_x, c_y)$ of all the boundary points $Q_k := (x_k, y_k), k = 1, 2, \ldots, m$. If one point p_i is inside the convex hull C, p_i and c should be on the same side of any line passing through two adjacent boundary points. Given a line $A^k x + B^k y + F^k = 0$ passing through Q_k and Q_{k+1}, the constraint on a strand point p_i is formulated as,

$$(A^k \cdot c_x + B^k \cdot c_y + F^k)(A^k \cdot p_{i_x} + B^k \cdot p_{i_y} + F^k) > 0 \tag{3.14}$$

Equation 3.13 is a quadratic constrained linear programming (QCLP) problem and is solved by the *sequential quadratic programming* (SQP) routine in MATLAB. We notice that only the radius variable r appears in the objective function. The other position variables are expressed in the constraints. From our experiment, the objective converges to a local optimal only when the initial positions are close to a good solution.

- **Sequential Automatic Solver** After we compute the strand locations p_i with good initialization specified by the user in the first frame, we can use p_i to set a good initialization for the next contour by warping (deforming) the first contour. Such initialization helps convergence of the optimization problem of the second frame without asking for user input, and can be applied in a sequential order to all other frames.

  The algorithm consists of the following steps.

  1. Given two sequential contours C_i and C_{i+1} with ordered contour points Q^{C_i} and $Q^{C_{i+1}}$, we establish the one-to-one correspondence between the two sets of points. We simply look for the closest points because of the relatively simple shapes of muscle. An example is shown in Figure 3.15b. For revolute geometry, contour shapes have to be aligned first.

     Given the correspondences, we first solve the deformation from the first contour C_i to the second contour C_{i+1}. Then the solved strand location p^{C_i} of C_i can be deformed correspondingly, and p^{C_i} is used to bootstrap C_{i+1}. Here we take advantage of the spatial consistency of sequential contours.

  2. Next, we set up a 2D *free form deformation* (FFD) grid for C_{i+1} (see

Figure 3.15b). Every intersection on the grid is a control point. Then we solve the deformation of the control points and move the contour points accordingly from Q^{C_i} to Q^{i+1} (see Figure 3.15c). This step involves inverse free form deformation (IFFD) and can be formulated as a linear system. We solve it by the preconditioned conjugate gradient method.

3. Given the new control point locations, we compute the new locations of the strand points in the previous slice. The updated positions serve as the initialization for the solver for C_{i+1}. See Figure 3.15c.

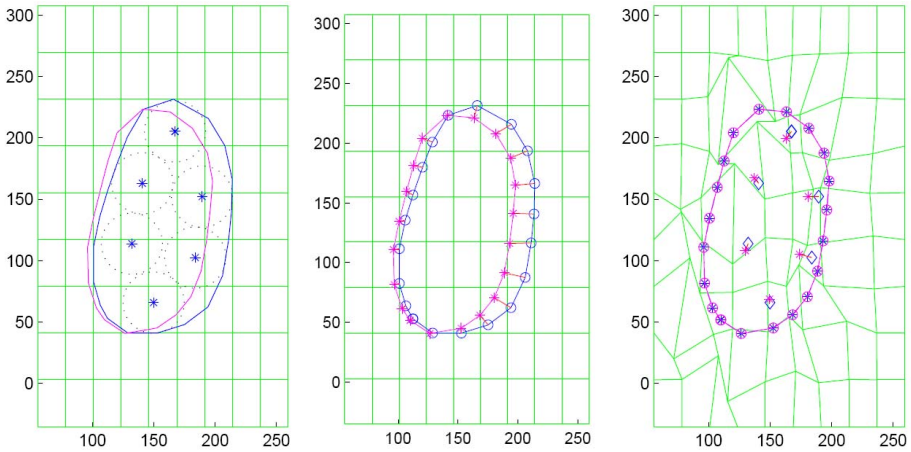

Figure 3.15: (a) Contour C_k is in blue and its solved strand points P^{C_k} are shown as the blue stars. The next contour C_{k+1} is in magenta. (b) Correspondences between Q^{C_k} and $Q^{C_{k+1}}$. (c) FFD grid deformation is computed such that Q^{C_k} are transferred to match $Q^{C_{k+1}}$. P^{C_k} are also deformed accordingly, which are used to initialize the solution of C_{k+1}.

- **3D Strand Modeling**

  Using the algorithms described above, we solve for the 2D strand points for every contour in sequence. We then fit cubic B-spline curves to the

2D positions and complete 3D strand construction. Figure 3.16 shows the fitted six strands of the LR muscle.

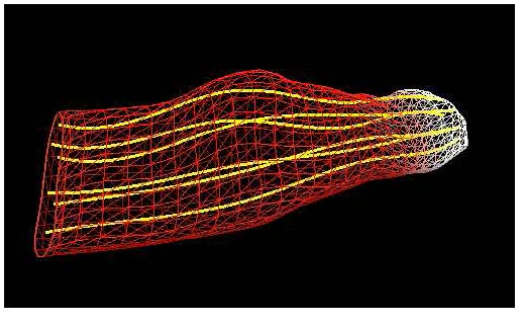

Figure 3.16: Six strands are fitted uniformly to the lateral rectus muscle mesh.

Recently, Levin et al. [2008] proposed a more general approach on generating multiple strands distributed throughout the 3D geometry of a skeletal muscle, on and inside the mesh. The method is based on a collection of energy minimizing active curves and it incorporates underlying muscle fiber directions from diffusion tensor imaging data.

3.5 Reconstruction of Eyeballs

Previous studies have employed MRI to quantify the size and shape of an eyeball. Curvatures of the retinal surfaces are analyzed [Atchison et al., 2005; Mutti et al., 2007] and 3D eyeball models are built [Singh et al., 2006]. A positive correlation between the axial length of the eyeball and the degree of myopia has been found. There are many other clinically important topics of the eyeball geometry that have not been investigated, such as the statistical variations of the eye shape of a large population and the possible gaze-dependent eye shape changes of normal subjects. Detailed and accurate eye models reconstructed from images are needed for such studies.

We extend our template-based reconstruction approach and develop a procedure to reconstruct detailed 3D models of the eyeballs from T_2-weighted MRI provide by Dr. Joseph Demer at UCLA. Compared to T_1-weighted MRI, T_2-weighted MRI provides excellent contrast between the eyeball and its surrounding tissues and hence enables automated boundary detection.

Our method is described in Algorithm 2. The image segmentation involves simple thresholding and hole-filling operators. A registration process is required to correct the head movement during two scans of the same subject. We use a variant of the iterative closest point (ICP) algorithm to find the best alignment. None of the two sets of boundary points B_c and B_s completely sample the whole shape because some of the images near the poles of the eyeball are too blurry to show accurate boundaries. In addition, B_c and B_s are from two nearly orthogonal imaging directions. As a result, the closest correspondence found in the other set may not be a truly close point. Instead of applying the ICP optimization on all data points from two image sets, we set a minimum distance threshold and only consider those points whose corresponding points are sufficiently close to avoid false correspondences.

Algorithm 2 Template-based Reconstruction of Eyeballs

1: Segment globe boundaries B_c from coronal MR images.
2: Segment globe boundaries B_s from sagittal MR images.
3: Register edges points B_c to B_s using ICP variant; $B_c \rightarrow B_c'$.
4: Fit a B-spline surface $S_{BSpline}$ to $B_c' \cap B_s$ which are sparse in space.
5: Fit a subdivision surface S_{subdiv} to densely sampled vertices P from $S_{BSpline}$ (see Algorithm 3).

The fitted B-spline surface closely models the geometry of the eyeball. However, since we use a B-spline surface with opening endings, artifacts occur at

two ends. It is also a bit hard to maintain mesh uniformness which is important for shape analysis. Here, we employ the Loop subdivision surface [Loop, 1987] based on an approximating subdivision scheme. Algorithm 3 describes Step 5 in Algorithm 2, fitting subdivision surface S_{subdiv} to vertices P, in more details. In our experiment, 10 iterations are in general sufficient to achieve a good fit.

Algorithm 3 Subdivision Surface Fitting

```
for Each iteration do
    for Each vertex v_i of S_subdiv do
        Find v_i's three "closest" vertices in P: p_1, p_2, and p_3
        Compute v_i's projection v̄_i on the plane formed by p_1, p_2, and p_3
        v_i ← v̄_i
    end for
    Perform mesh smoothing on S_subdiv
end for
```

Figure 3.17 shows the reconstructed eyeballs from anonymous subjects, which are identified by their two-letter IDs. MRI data is provided by Dr. Joseph Demer. Asymmetry of the two eyes of each subject as well as the nonspherical shape characteristic is observed. Eyeballs of some subjects (for example Subject RB) are more oblate than other eyeballs.

3.6 Conclusions

We have developed a computational framework for building subject-specific models of the orbit from MRI, using adaptive feature selection and parametric surface fitting. It is a template-based approach and uses the anatomy of the orbit as the prior knowledge to bootstrap 3D reconstruction of different subjects.

Our framework eases quantitative analysis of orbital anatomy and morphology. It is useful for both laboratory studies and clinical applications. The

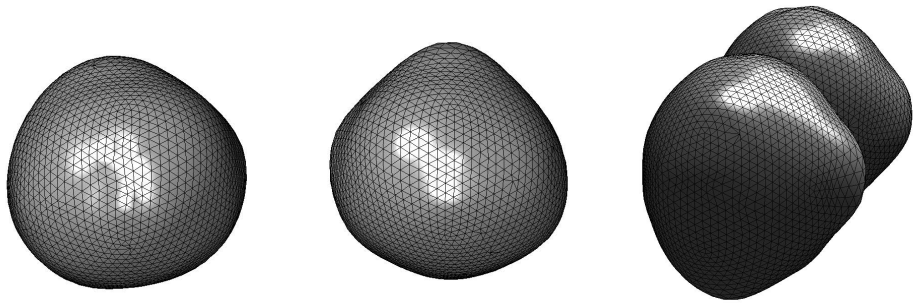

(a) Subject BB (top view) (b) Subject BB (side view)

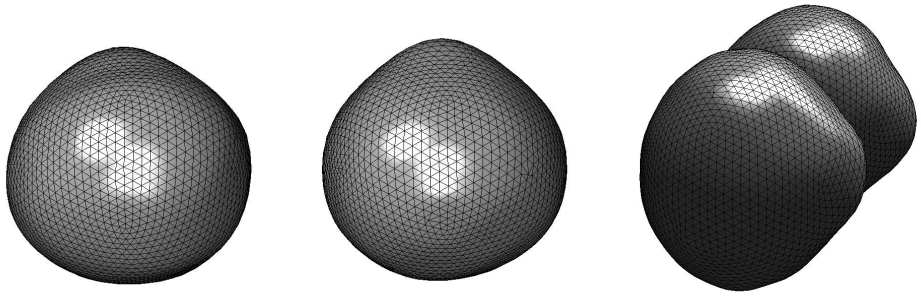

(c) Subject CS (top view) (d) Subject CS (side view)

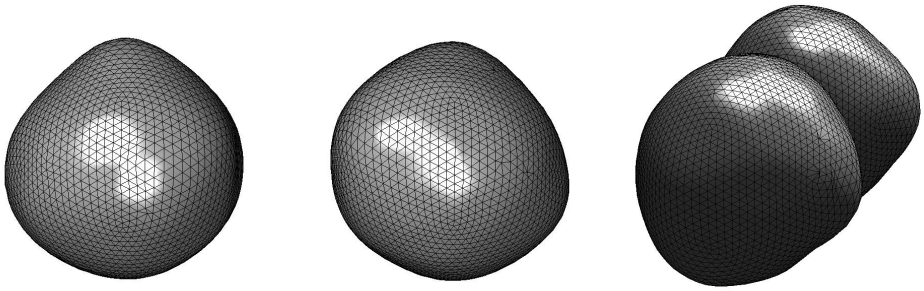

(e) Subject GA (top view) (f) Subject GA (side view)

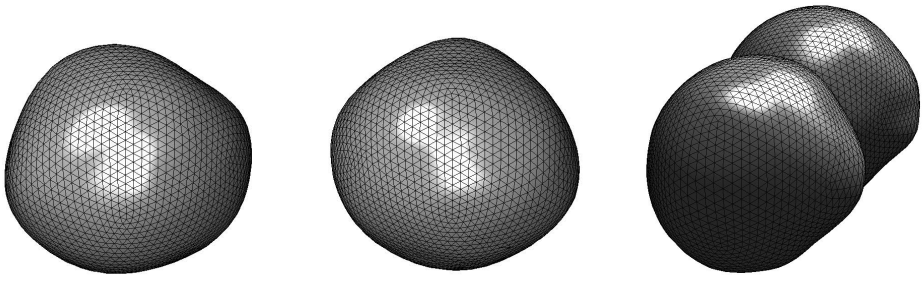

(g) Subject GP (top view) (h) Subject GP (side view)

Figure 3.17: Reconstructed eyeballs from T_2-weighted MRI.

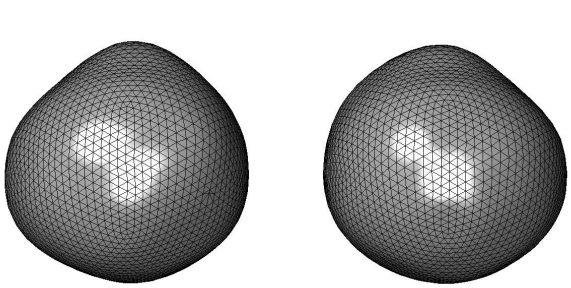

(i) Subject HU (top view)

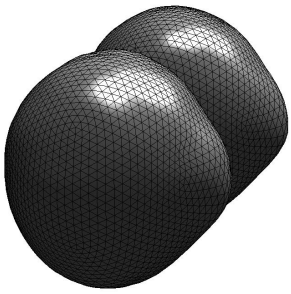

(j) Subject HU (side view)

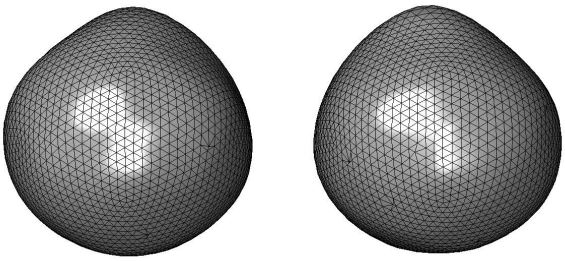

(k) Subject KP (top view)

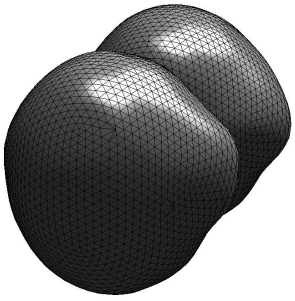

(l) Subject KP (side view)

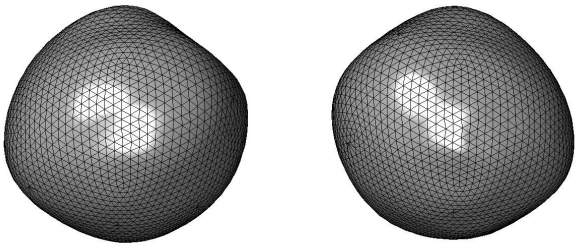

(m) Subject LG (top view)

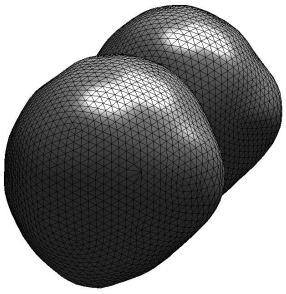

(n) Subject LG (side view)

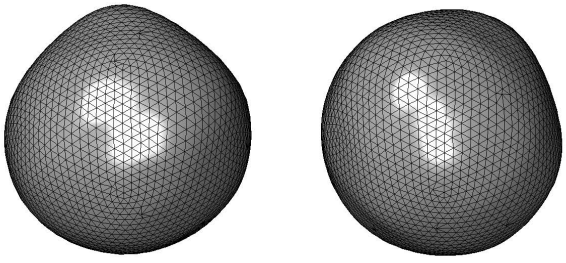

(o) Subject LW (top view)

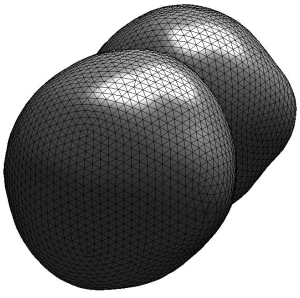

(p) Subject LW (side view)

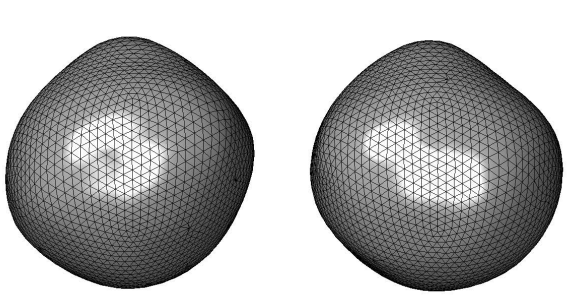

(q) Subject MU (top view)

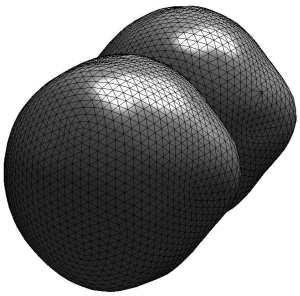

(r) Subject MU (side view)

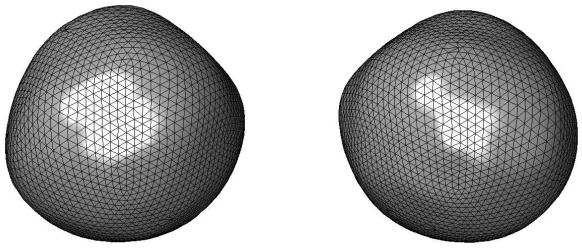

(s) Subject PL (top view)

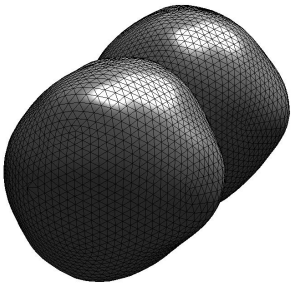

(t) Subject PL (side view)

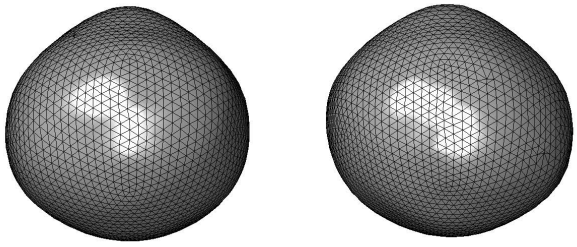

(u) Subject RB (top view)

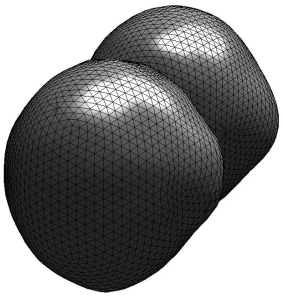

(v) Subject RB (side view)

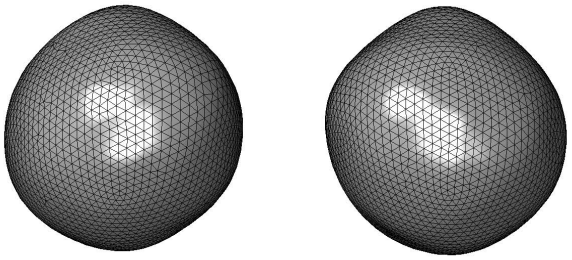

(w) Subject WC (top view)

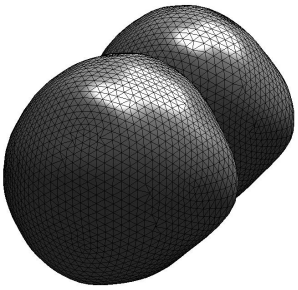

(x) Subject WC (side view)

method can be used to simultaneously reconstruct geometries, EOM deformation, and path inflection in different eye positions. Biomechanical simulation will benefit from these models by incorporating estimated EOM strains (to be introduce in Section 4.4) and inferred pulley locations [Clark et al., 2000; Kono et al., 2002a].

Chapter 4
Longitudinal Strain Estimation in Cylindrical Tissues from MRI

4.1 Introduction

Estimating deformation properties of soft tissues is a fundamental problem in biomechanics. It is useful for understanding tissue mechanical properties and functions. For instance, the strain field showing the deformation pattern of the material is commonly used to determine tissue mechanical properties, such as elasticity. Realistic biomechanical modeling and simulation also require knowledge of material properties, as well as reconstruction of geometric models with minimal distortion. However, accurate and efficient material property estimation *in vivo* is challenging.

Our study is motivated by the observation that sometimes conventional imaging techniques are insufficient to infer muscle and tendon mechanical properties, due to limited image resolution, homogeneous intensity, etc. For example, although high resolution MRI has already become a routine diagnosis tool for strabismus patients, it is still impossible to estimate extraocular muscle (EOM) deformation property as a function of gaze directly from these images because of the lack of distinguishable features inside EOMs. We propose an approach to determining EOM longitudinal deformation from reconstructed 3D geometric models. It does not rely on image features to establish

tissue correspondences; therefore, it does not suffer from the image inadequacy problem.

4.1.1 Related Work

Different imaging modalities have been widely employed to estimate material properties by tracking tissue deformation. We list a few representatives here. Ultrasound is used for measuring strains [Lubinski et al., 1996; Witte et al., 2006], because of its noninvasive feature and real time capability. In particular, ultrasound elastography has been developed to measure the elastic properties of tissues, leading to important applications including lesion detection in breasts and prostates. MRI [Gilchrist et al., 2004] and fluoroscopic imaging [DeFrate et al., 2006] have also been used for strain estimation. Most of these approaches compute the material displacement through finding *tissue correspondences* in two images. Tissue correspondence refers to the mapping of the tissue in one state to the "corresponding" tissue in another. However, it is not always possible to establish correspondences due to poor image resolution, homogeneous intensity across the material, smooth shape deformation, etc.

One approach to solve the correspondence problem is the MRI tagging technique which introduces tags in the imaging process to capture the underlying tissue movement. Tagged MR images have been applied in estimating myocardial strains [Osman et al., 1999; Reichek, 1999; Qian et al., 2007], hamstring strains [Fiorentino et al., 2007], and extraocular muscle deformation [Piccirelli et al., 2007]. Magnetic Resonance Elastography (MRE) combines MRI with low-frequency sound waves. It is able to measure the viscoelastic properties of tissues [Muthupillai and Ehman, 1996; Dresner et al., 2001; Bensamoun et al.,

2007]. Cine phase-contrast MRI has also been proven to be effective (RMS error of $1mm$) for tracking skeletal muscle motion [Asakawa et al., 2003; Zhong et al., 2008]. Applications using these techniques are limited by their availability and time efficiency. They are mostly restricted to two-dimensional strains, assuming that the off-plane tissue movement is negligible. Three-dimensional cardiac strains are estimated from 4D Cine-MRI by modeling the preferential stiffness of the myocardium tissue along fiber directions as a transversely linear elastic model [Papademetris et al., 2000], and from tagged MRI by tracking motions with meshless deformable models [Wang et al., 2008].

Another way is to introduce extra tissue markers that are easier to track. Dye lines of elastin stain are applied on the gastrocnemius tendon-muscle unit for measuring longitudinal strain [Trestik and Lieber, 1993]. Markers are attached to the surfaces of the tendon and muscle [van Donkelaar et al., 1999; Wren et al., 2001; DeFrate et al., 2006] or implanted in the extraocular muscles [Miller et al., 2006]. The surface markers are limited to the study of cadaver tissues or superficial live tissues. The bead implant is complicated and apparently cannot be applied on human subjects.

4.1.2 Outline

We propose a new algorithm for measuring the longitudinal strain of an object when the images are inadequate for providing enough information of the object interior. Usually, the boundaries are relatively easy to extract through automated or manual segmentation because of the contrast between different tissues. Our goal is to compute the one-dimensional strain field along the major deformation axis, given only the boundaries of the tissue of generalized cylindrical shape. A *generalized cylinder* (GC) is defined as a cylindrical object

resulting from sweeping a possibly varying cross section along a trajectory, which is an arbitrary space curve [O'Donnell et al., 1994]. Note that the cylinder does not have to be axis-symmetric since the cross sections can be arbitrary too. The flexibility of a GC makes it a realistic geometric representation of muscles and tendons.

Instead of the transverse strain, we focus on the longitudinal strain – one of the most important parameters in measuring material properties of ligaments and tendons [Trestik and Lieber, 1993; Wren et al., 2001; DeFrate et al., 2006]. The key point of our method depends on the fact that most soft tissues are incompressible to a very good approximation [Lubinski et al., 1996; van Donkelaar et al., 1999; Epstein et al., 2006]. In other words, the volume of the tissue material is nearly constant in different deformed states as well as in the steady state. By using only this physical property, we compute longitudinal strains by finding segment-to-segment correspondences instead of discrete point-to-point correspondences.

In Section 4.2, we introduce our methodology by using a 2D synthetic example for the simplicity of conveying the idea. It is straightforward to extend the method to three-dimensions. To validate the effectiveness of the approach, we apply it to real MR images of a rubber phantom modeling a muscle (see Section 4.3.1). Predicted longitudinal displacements are compared with the ground truth (gold standard) given by markers in the phantom. Further evaluation is performed by sensitivity analysis of computer simulated data in Section 4.3.2. Finally, in Section 4.3.3 we present a practical application of our approach to estimating longitudinal strains of EOMs from human subject MRI. Estimated deformation can be used as physical constraints to register EOM models in different eye positions (see Section 4.4). We conclude by discussing

the limitations of the proposed method and future work in Section 4.5.

4.2 Methods

To ease illustration, we describe our algorithm using a simulated 2D muscle-like elastic object. The method applies directly to any generalized cylinder. We demonstrate the method using the segmented data of MRI from a rubber phantom presented in Section 4.3.1.

Figure 4.1a shows a 2D object in the steady state, the boundary of which is outlined in red. Figure 4.1b represents the object after deformation, which is being elongated to the positive x direction. (The objects could also be in two deformed states.) The total area is constant. Given only the boundaries, we show how our algorithm computes the strain field along x-axis. In general, the boundary does not have to be as smooth as this example (see Section 4.3.2 for applications on noisy data).

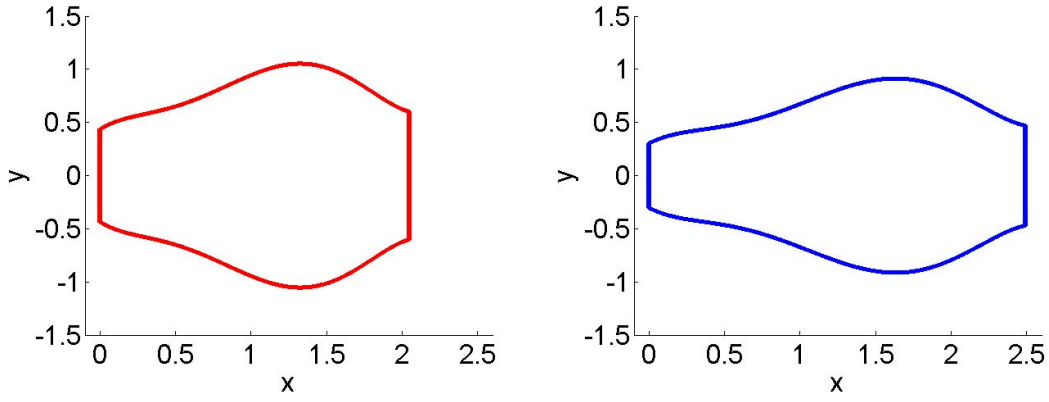

(a) Before deformation (b) After deformation

Figure 4.1: A 2D example showing an object (a) before deformation and (b) after deformation.

The whole area (volume if in 3D) is first discretized into M equal area segments along the x-axis as follows. The cumulative area function f_c over x

(shown as a blue curve in Figure 4.2) is first computed. A finite difference approximation is used to calculate the area,

$$V_{total} = \sum_{i=1}^{N-1} (x_{i+1} - x_i)(l_{i+1} + l_i)/2, \tag{4.1}$$

where l_i is the length (area in 3D) of the vertical section at $x = x_i$ and N is the number of samples. Then the total area along the vertical volume-axis is uniformly divided (shown as the cyan line segments in Figure 4.2). These divisions intersect f_c at M locations, which are then projected onto the x axis. The magenta lines in Figure 4.2 show the projections, and they define the equal area segments. The accuracy of the uniform partition depends on the number of segments.

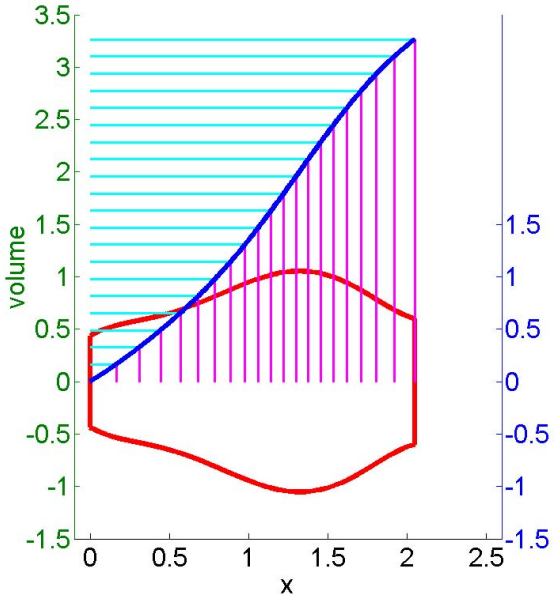

Figure 4.2: The cumulative volume function and the resulting segments of same area from projection.

In Figure 4.3a, the example is uniformly partitioned into 4 segments in both states. We use fewer segments here for clearer demonstration. All segments have approximately the same area, $\Delta V_{before} = \Delta V_{after} = V_{total}/4$. Therefore,

each segment before deformation can be associated with one afterwards, following the sequential order along the x-axis. Instead of tracking image-based point-to-point correspondences, 1D shape-based segment-to-segment correspondences, shown as the purple dashed arrows in Figure 4.3b, are established using incompressibility.

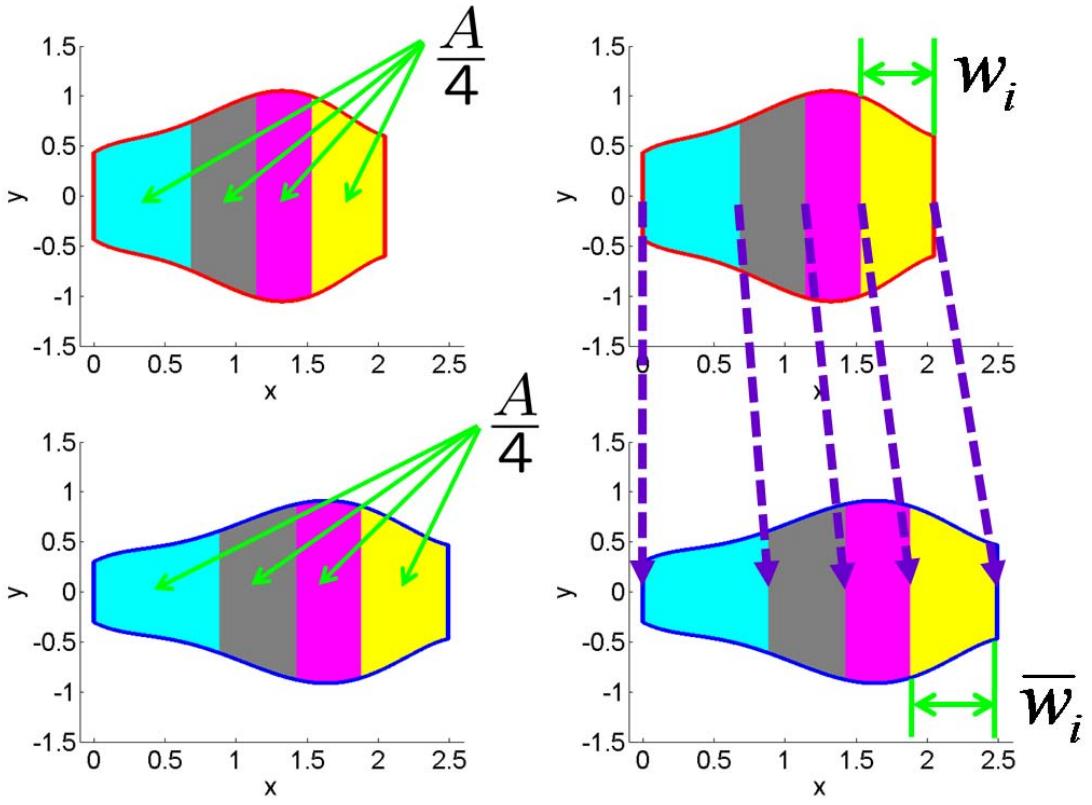

(a) Area division (b) Segment correspondences

Figure 4.3: (a) Each object is divided into 4 segments of equal area. (b) Purple arrows indicate segment correspondences.

The longitudinal strain of each segment is computed as

$$s^i = \ln \frac{\overline{w^i}}{w^i}, \tag{4.2}$$

where w^i and $\overline{w^i}$ are the weighted average widths of the i^{th} segment before and after deformation (see Figure 4.3b). Figure 4.4 shows the estimated strain of

the above example in 20 segments. The green curve is the spline interpolation of the raw strain field computed at the centers of the 20 segments (shown as yellow squares). As expected, nonuniform strain is observed for this example.

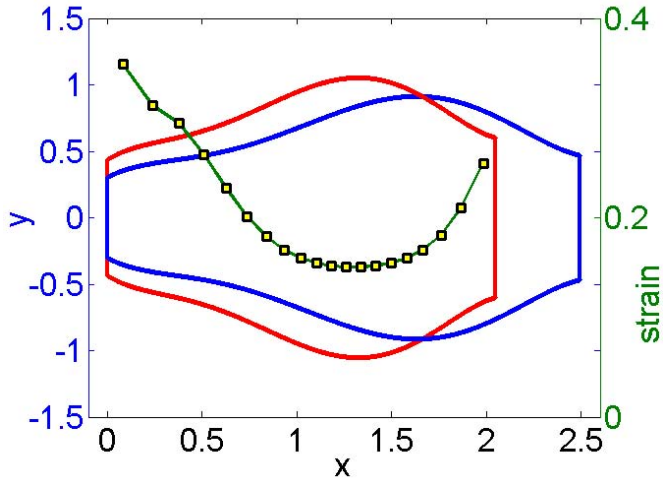

Figure 4.4: Estimated longitudinal strains shown as the yellow squares are computed for 20 segments. A continuous strain field is obtained by interpolating the discrete strain estimates, shown as the green curve.

4.3 Results

To validate the effectiveness of our approach, we apply it to real MR images of a 3D tissue phantom, as described in Section 4.3.1. Predicted longitudinal deformation is compared with the ground truth given by the markers inside the phantom. Further evaluation is performed by sensitivity analysis of computer simulated data in Section 4.3.2. We assess the accuracy of the method in noisy conditions. Finally, we present the estimated longitudinal strains of extraocular muscles from clinical human subject MRI to demonstrate the usefulness of our approach (see Section 4.3.3).

4.3.1 3D Phantom Validation

In order to test the applicability of this approach in real applications, evaluation is first performed on real MR images of a rubber phantom mimicking generalized cylindrical soft tissues. MRI is used since it is widely used for *in vivo* imaging the musculoskeletal system and the ocular system of human subjects.

Experiment Design

The tissue phantoms were made from silicone rubber (Smooth-On, Easton, PA) embedded with glass beads (BioSpec, Bartlesville, OK). MR images of the phantoms at different stretched states were acquired with $0.5mm$ voxel resolution from a Philips 3.0 Tesla MRI scanner. We compare the phantom deformation estimated by our algorithm to the ground truth obtained by tracking the displacements of the glass bead markers.

Figure 4.5a shows two rubber phantoms glued to two fiber glass boards in a MR compatible box, viewed from the top. The box stabilizes the phantoms in different stretching states. At the rest state, each phantom is about $83.5mm(L) \times 25mm(W) \times 18mm(H)$. The two phantoms were made from rubbers of different hardness. The upper phantom was made of silicone rubber Ecoflex^{TM} with hardness 00-30A and the lower one was from Dragon Skin^{TM} with hardness 10A [1]. About 40 solid glass beads ($\sim 1mm$ in diameter) were scattered inside the phantom. The beads appear dark in the MR images due to their MRI invisibility, while Silicone rubbers appear bright. Such nice contrast enables easy tracking of the bead locations and gives us ground truth of the

[1] Hardness is measured by Shore durometer. Echoflex 00-30A has Shore 00 scale and durometer 30. Dragon Skin 10A has Shore A scale and durometer 10

phantom deformation.

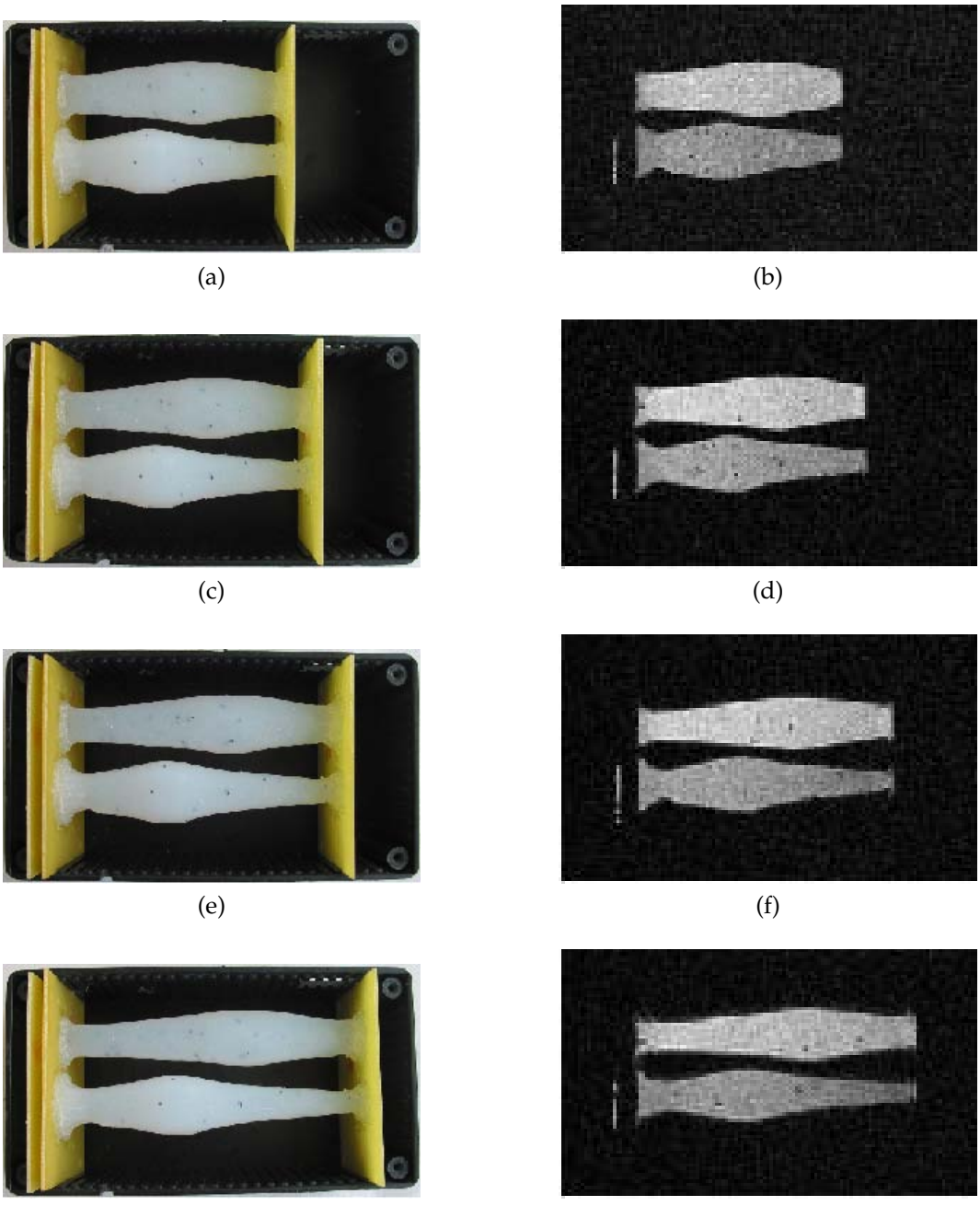

(a) (b) (c) (d) (e) (f) (g) (h)

Figure 4.5: Photos and the corresponding MR images of the phantoms which were (a)(b) at the reference state; (c)(d) elongated by 1.11; (e)(f) elongated by 1.22; (g)(h) elongated by 1.33. The dimensions of the box are $135mm(L) \times 75mm(W) \times 70mm(H)$. The total lengths of the phantoms in the four states are $83.5mm$, $92.7mm$, $101.6mm$, and $111.2mm$ respectively.

Experiment Results

T_1-weighted gradient echo 3D MR images were acquired from a Philips Achieva 3.0 Tesla MRI scanner in the MRI Research Centre in the University of British Columbia. The scan matrix is 400×200 and the voxel size of the isotropic 3D image data is $0.5mm$. 60 coronal images were scanned in each elongation state of the phantom. Figure 4.5 shows pictures of the phantoms at different elongation states as well as the corresponding MR images. The amount of each elongation was determined by the spacing of the vertical slots that supports the phantom in the box. Each glass marker shows up in at least one voxel. In the following, we mainly discuss the results from the Ecoflex^{TM} phantom. From our data analysis, Dragon Skin^{TM} performs similarly to Ecoflex^{TM}.

Axial images are reconstructed from 3D image data. The slice thickness is the same as the spatial resolution, which is $0.5mm$. Threshold segmentation is applied to the axial images. The cross sectional areas are estimated from the segmented areas and shown in Figure 4.6. We apply our method to the part between the first and the last recognizable markers along the longitudinal axis of the phantom and we call it the *valid phantom volume*.

We first check the validity of the incompressible assumption on our phantom. Figure 4.7 plots the accumulated *valid volume* of the phantom along the longitudinal axis at each state. The total volumes are summarized in Table 4.1. The most stretched state (elongation by 1.33) has the maximal volume loss (about 1.22%) compared to the reference state. The volume loss might be caused by the blurry boundaries in MR images of the elongated phantom (see Figure 4.5h). This volume loss leads to less accurate image segmentation. The blur is caused by the change of resonance due to vibration of the phantom under the mechanical noise created by the scanner. The more stretched the

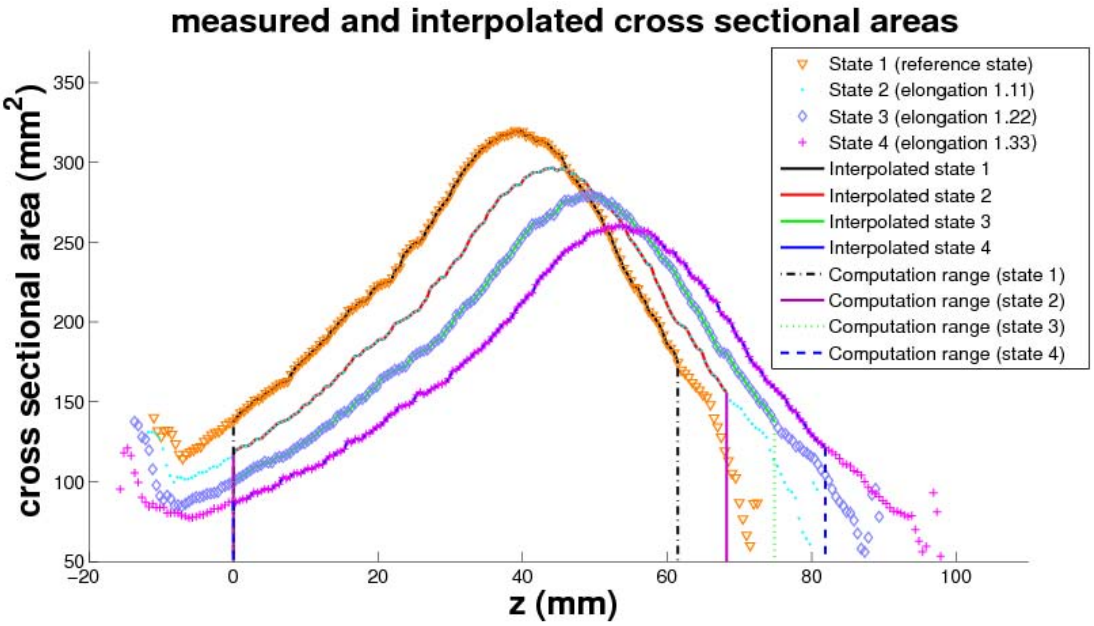

Figure 4.6: Measured and (spline) interpolated cross sectional areas of the phantom at different elongation states. Data from four states are aligned along the longitudinal axis z by the first recognizable marker in the phantom.

phantom is, the more vibration the phantom might experience. However, volume loss of about one percent is still small and negligible. We conclude that the volume preservation assumption holds for the rubber phantom.

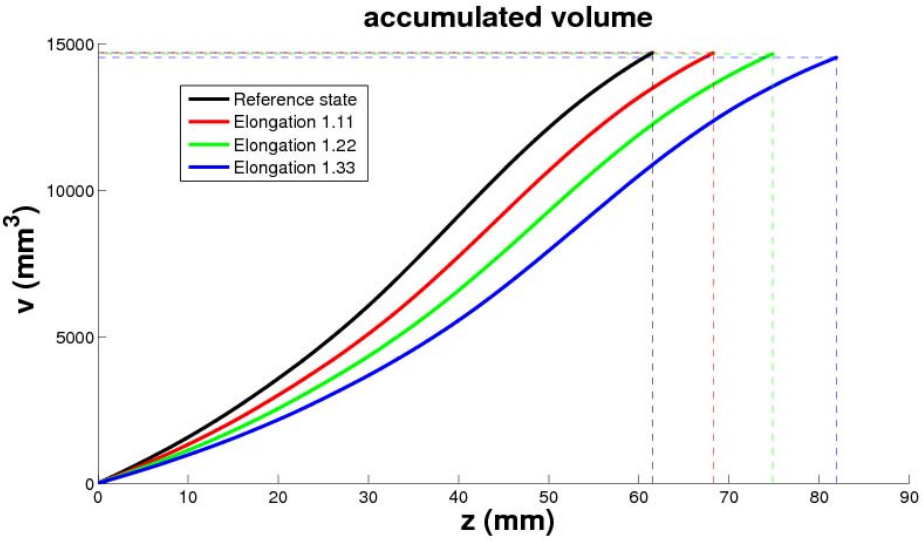

Figure 4.7: Accumulated (*valid volume*) of the phantom at different states.

State	Elongation	Volume (mm^3)	Volume loss (%)
1	0	14695	0
2	1.11	14692	0.02
3	1.22	14638	0.39
4	1.33	14516	1.22

Table 4.1: Total valid volumes of all states.

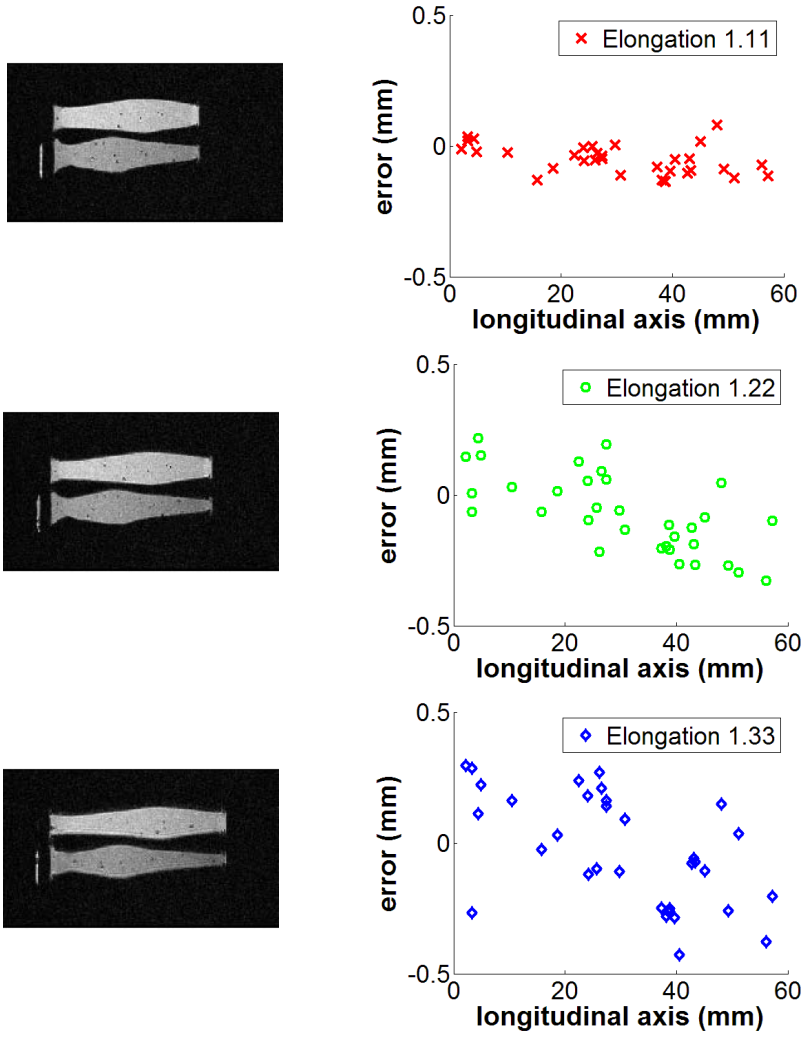

Figure 4.8: Axial displacement error e at three elongations.

Glass beads embedded in the phantoms are identified and their centers of mass are used as their 3D locations. Our approach is validated by computing the error, defined as the difference between the bead location predicted by the

method described above and the actual bead location. Figure 4.8 plots the errors of all the markers in three elongation states. Note that the errors are all bounded by the MRI resolution $0.5mm$. The result proves the accuracy of the method.

We also compare the estimated longitudinal strains with the phantom to the actual strains interpolated from the tracked bead displacements. We use those beads that are at least $2mm$ apart in the rest state such that errors introduced by imaging resolution $0.5mm$ and marker size ($\sim 1mm$ in diameter) can be diminished. Figure 4.9 shows the strain comparison in three elongated configurations. Our estimated strains well approximate the true strains.

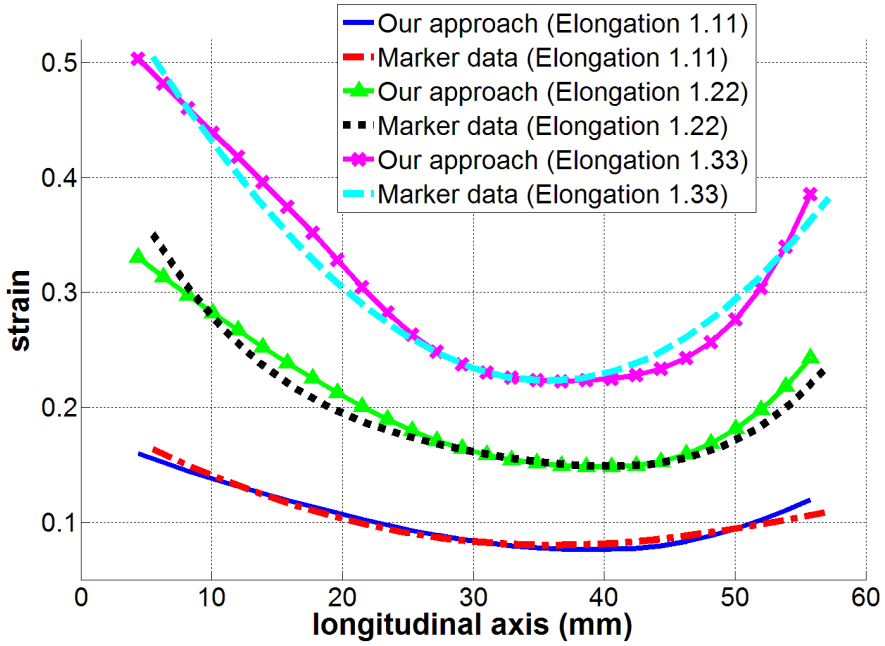

Figure 4.9: Comparison of strains estimated from our approach and true strains interpolated from actual bead displacements.

4.3.2 Simulated Sensitivity Analysis

In the sensitivity analysis using simulated data, the input is perturbed by either adding errors to the boundary measurement or violating the basic assumptions. The method described in Section 4.2 is applied on the perturbed input, and errors are analyzed with respect to the noise level.

Shearing

In this experiment, we assume that the tissue shears to some extent (see Figure 4.10 for an example). A simple 2D shearing model is considered. Mathematically, each point (x, y) in the object moves to (x', y'), where $x' = x + y \tan \alpha, y' = y$. α is the shear angle.

Obviously, volume is preserved. Both the true x-strain and y-strain are zero. If we apply our method, we will not get exactly zero strain along the x-axis because of the geometric distortion perpendicular to the x-axis. Figure 4.10 shows the estimated strains. The maximum strain error is about 0.0085.

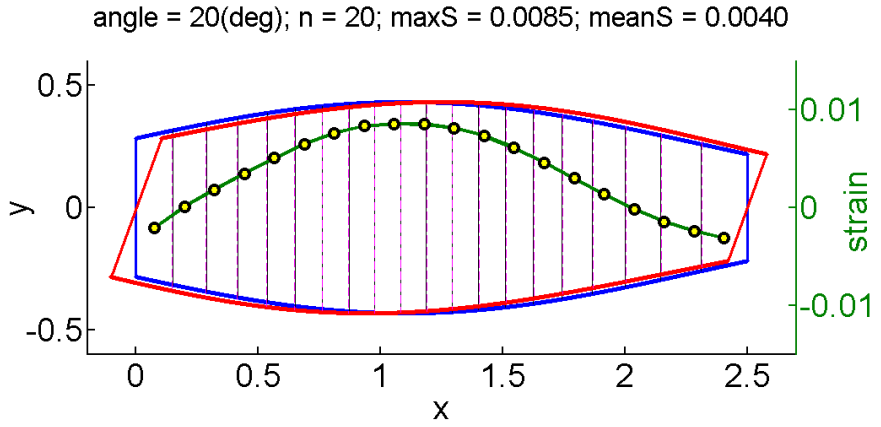

Figure 4.10: Example showing estimated strains with shearing along the x axis. Original tissue in blue is sheared by 20 degrees and becomes the object in red. Estimated strains are shown as the green curve. The vertical scale of strain is magnified to make the small variation in strain visible.

Strain fields at different shearing angles are computed. Intuitively, the strain error increases as the shearing angle increases. The magnitude of the strain error is studied, which is just the absolute value of the estimated strain because $|s^i - s_0^i| = |s^i - 0| = |s^i|$, where s^i is the strain of the i^{th} segment and s_0^i is the true longitudinal strain under shearing. Figure 4.11 shows the error statistics $max(|s^i|)$ and $average(|s^i|)$ at 26 different shearing angles. The maximum error is only about 0.015, even with shearing of 26 degrees. We conclude that the error due to tissue shearing along the longitudinal axis is small and the method is robust to 1D shearing.

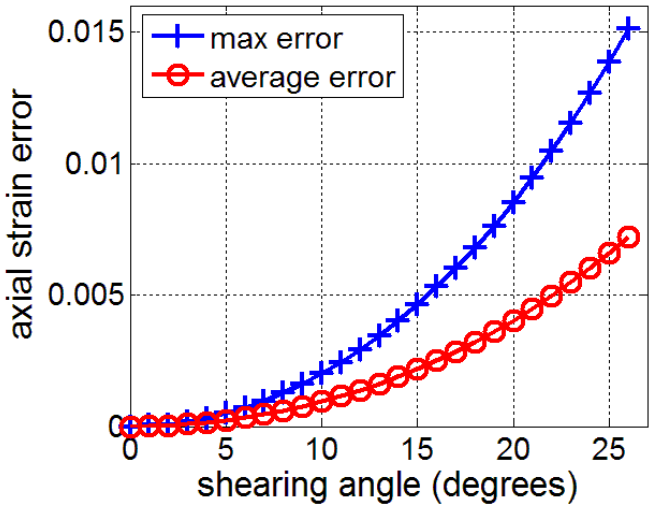

Figure 4.11: The statistics of strain errors given different shearing angles.

High frequency Gaussian noise

Next, we consider the cases where boundary measurement is imperfect. Here the boundary is assumed to be corrupted by additive Gaussian noise. An example is shown in Figure 4.12. Independent boundary noise is applied on the before-deformation tissue in magenta and the after-deformation tissue in cyan. We observe that the estimated strains with noisy input deviates from the true

strains by small amounts, varying along the x axis.

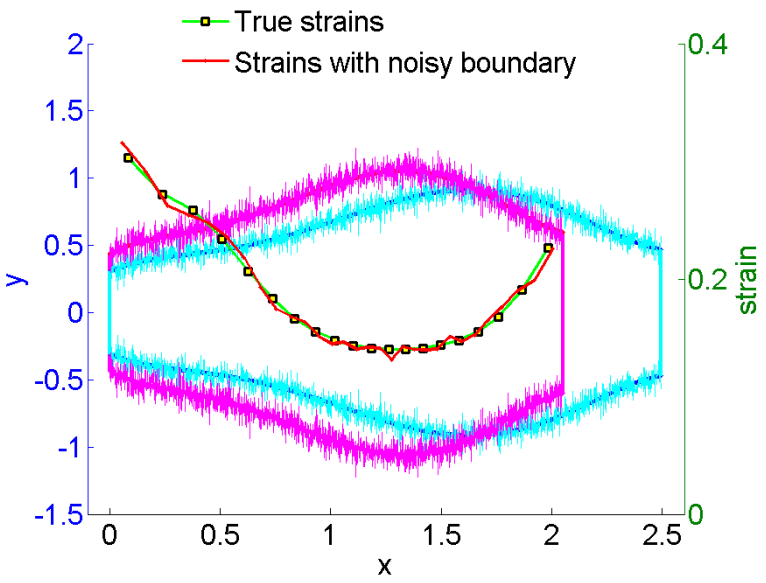

Figure 4.12: An example showing strain errors due to additive Gaussian noise ($\sigma^2 = 0.032$) on the boundaries.

Strain errors at thirteen noise levels, specified by the variance of the Gaussian noise, are studied. For each level, the following process is repeated for 100 times and the average is taken as the error measurement. Random Gaussian noise is generated and added to the original boundary. Then the strain fields, s_0 from the original data and s from the noisy data, are estimated respectively. The maximum and average of the strain error magnitude, $max(|s^i - s_0^i|)$ and $average(|s^i - s_0^i|)$, are recorded. Figure 4.13 shows the statistics of the strain error. The error increases almost linearly with the noise variance. Even with the largest perturbation, the maximum error is still below 0.01. It is possible that the high frequency Gaussian boundary noise is canceled to some extent in the cumulative segment partition and thus the influence due to noise is diminished. We conclude that this kind of high frequency noise does not affect the overall performance much.

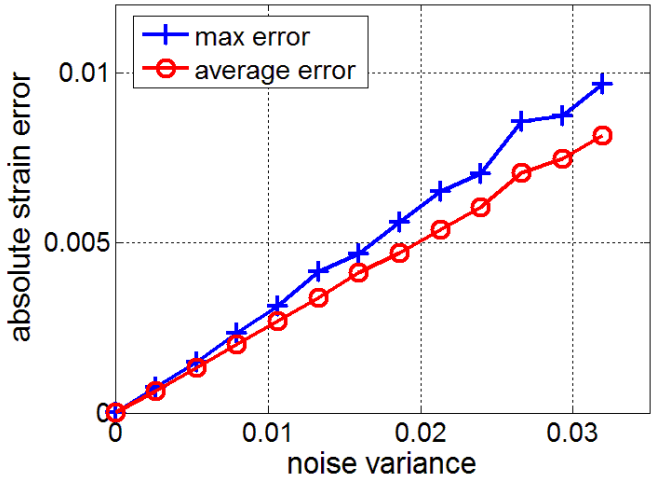

Figure 4.13: The maximum and average strain errors given different Gaussian noise variance.

Low frequency sinusoidal noise

Here we consider sinusoidal noise added to the boundary,

$$d(x) = A\cos(2\pi f x). \tag{4.3}$$

We analyze the relationship between the strain error and the magnitude and frequency of sinusoidal noise. The experimental procedure is same as the one described in the previous section on Gaussian noise. In our simulation, we observe that the strain error increases linearly with the noise magnitude (see Figure 4.14a). Figure 4.14b shows the maximum and average strain errors due to noise with different frequencies with fixed magnitude $d(x) = 0.055\cos(2\pi f x)$. We do not see analytical relationship between the error and the noise frequency. The maximum error reaches its peak where the noise frequency is about 4. One possible explanation is that as the frequency increases, the additive noise might be canceled in the cumulative volume calculation, like in the case with Gaussian noise. The number of segments is another important factor that influences the error curve.

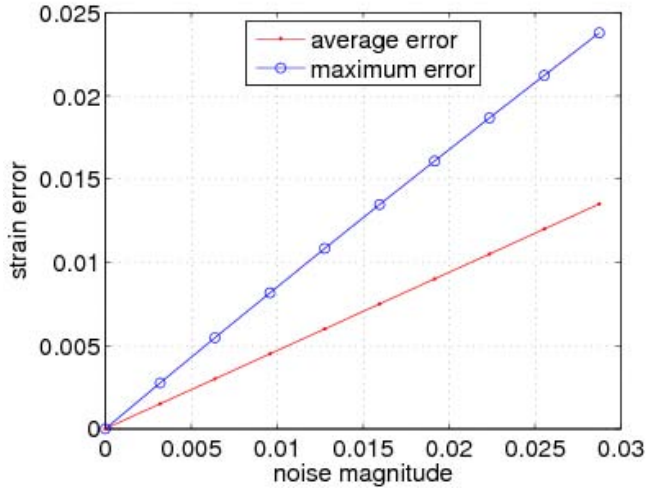

(a) Strain error with varying noise magnitude

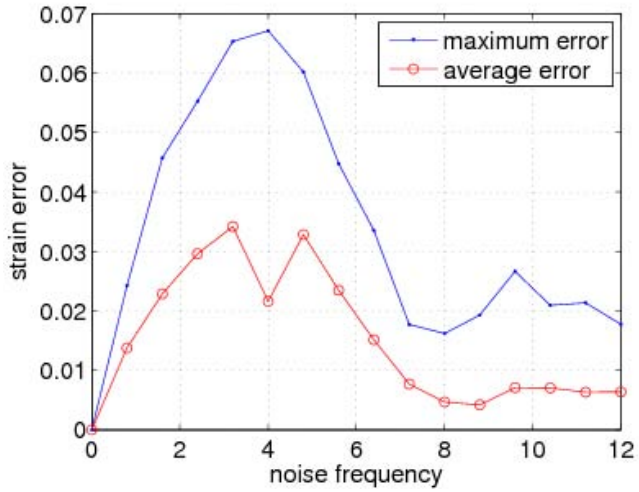

(b) Strain error with varying noise frequency

Figure 4.14: The maximum and average absolute strain errors given different sinusoidal noise (a) magnitudes and fig:sinusoidalErrors:b frequencies.

4.3.3 Longitudinal Strains of Extraocular Muscles from MRI

We now demonstrate the application of our method to extraocular muscles mechanics. Understanding how EOMs deform *in vivo* as a function of gaze is important in studying the physiological and mechanical properties of the oculomotor plant. However, measuring EOM deformation is challenging. Miller et al. [Miller et al., 2006] implanted gold beads in the orbits of monkeys and

tracked these markers using CT imaging. Clearly, this technique cannot be used on human subjects. Motion-encoded MRI has recently been used to assess EOM motion [Piccirelli et al., 2007]. However, limited by the imaging resolution and imaging dimensions, local deformation along the EOM axis has not been available [Piccirelli et al., 2007]. Neither paper reports local EOM strains quantitatively.

As pointed out by Piccirelli et al. [2007], EOM deformation cannot be directly acquired from conventional MRI. Our method solves this problem by computing longitudinal strains from models reconstructed from MRI instead of from the images themselves. We see our approach as complementary to the above techniques because of its simplicity and usefulness on widely available conventional MRI data from human subjects.

Models of the two horizontal muscles (LR and MR) in the right eye of a human subject in three eye positions are reconstructed from MRI [2]. The template-based reconstruction method described in Chapter 3 is used. The 3D models in adduction, primary, and abduction gazes as well as three magnetic resonance images acquired at about the same spatial location are shown in Figure 4.15. LR and MR muscle boundaries are outlined in red in the MRI.

EOM deformation can be seen from the 3D shape variations and from the segmented boundaries in MR images. Compared with the primary gaze, the LR cross sectional area in abduction gaze becomes larger due to its contraction while the MR cross section is smaller because of passive elongation. Similar systematic EOM deformation pattern is also observed in the adduction gaze.

The medial axis of an EOM is estimated from the reconstructed mesh and represented by a cubic B-spline curve. It is used as the longitudinal axis. Note

[2] Anonymous MRI data was provided by Dr. Joseph Demer.

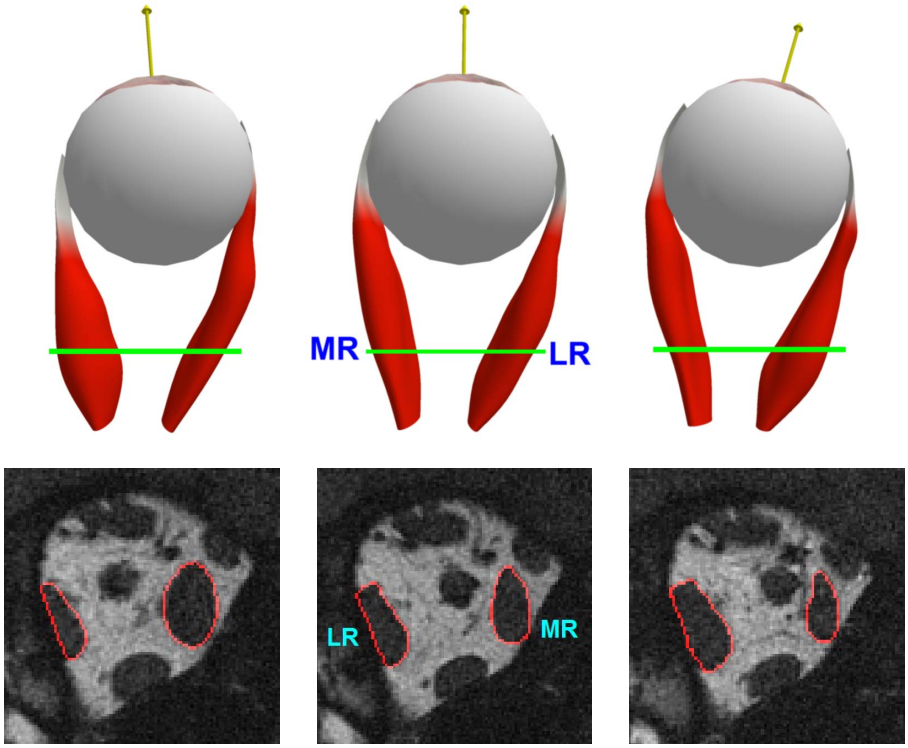

(a) Adduction (b) Primary (c) Abduction

Figure 4.15: Reconstructed geometric models of LR muscle and MR muscle, and corresponding magnetic resonance images at the imaging planes indicated by the green lines in (a) adduction gaze, (b) primary gaze, and (c) abduction gaze.

that our method is sufficiently general to apply on curved tissues. The whole volume is discretized along the medial axis into cross sections, perpendicular to the axis. The cumulative volume is the discrete integral of the cross sectional areas along the axis. Longitudinal strains are then estimated from the computed axial displacements of the segments.

In Figure 4.16, we show the estimated longitudinal strains of LR and MR when the eye moves from the primary straight ahead position to adduction and abduction respectively. We compute the strains of the middle EOM bellies, which are less affected by tissue distortion near the EOM origin and insertion. Positive strain is in the EOM elongation direction and negative strain is in the

shortening direction.

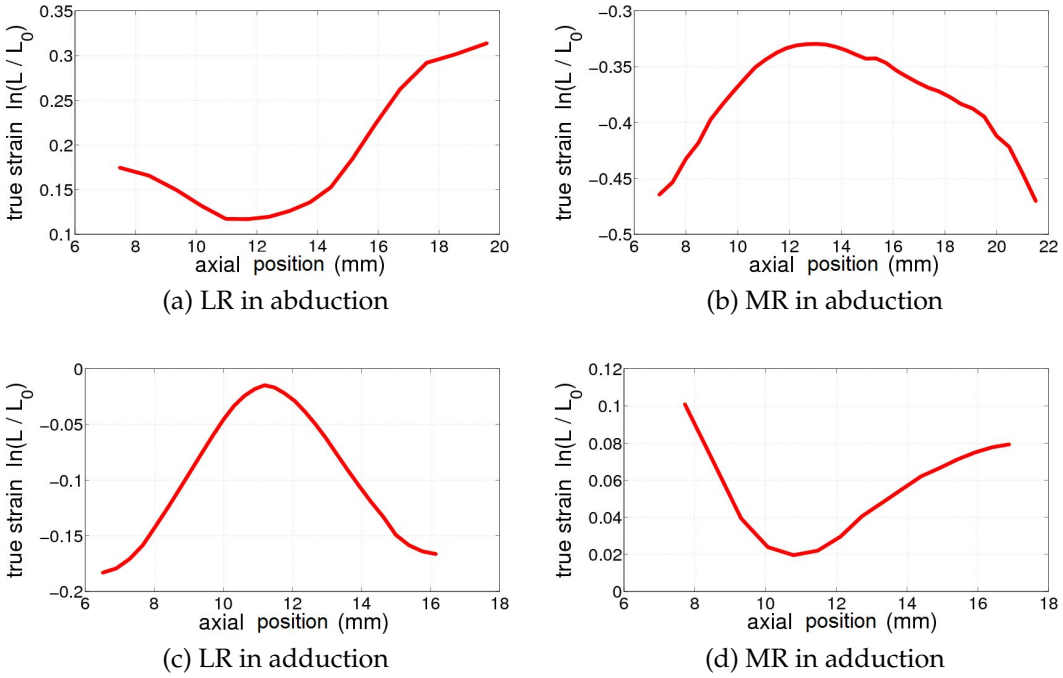

(a) LR in abduction

(b) MR in abduction

(c) LR in adduction

(d) MR in adduction

Figure 4.16: Longitudinal strains of LR and MR estimated from the reconstructed models in Figure 4.15. (a) and (b) show the strains in abduction. (c) and (d) show strains in adduction.

Nonuniform shortening of skeletal muscles with parallel-fibered architectures has been studied [Pappas et al., 2002; Blemker and Delp, 2005]. Although EOMs are different from other skeletal muscles in many aspects, they do share some common properties, such as the constant muscle volume and nonlinear force-length relationship. It is useful to see whether EOM also deforms heterogeneously. Our results in Figure 4.16 show that EOM deformation is also nonuniform in both active shortening (LR in abduction and MR in adduction) and passive elongation (LR in adduction and MR in abduction). The nonuniform deformation is consistent with our proposition and could lead to other studies on EOM functions.

4.4 Application

In this section, we illustrate an important application of the strain estimation method to building realistic biomechanical models. We show that the estimated longitudinal strains presented in Section 4.3.3 can be used in physically consistent registration of the reconstructed EOM meshes. Constrained by the estimated EOM deformation, the resulting models can be both more anatomically accurate and physically meaningful. The models are discretized in material coordinates in each state and consistent with the real tissue deformation. Material correspondences are provided directly, which ease biomechanical simulation and model parameter estimation. Our method is not restricted to modeling EOMs but can be generalized to other incompressible generalized cylindrical objects in various deformed configurations.

The rest of this section is organized as follows. In Section 4.4.1, we introduce the motivation behind this study and related work. The registration approach formulated as a constrained optimization problem is presented in Section 4.4.2. Results on the rubber phantom and extraocular muscles are described in Section 4.4.4.

4.4.1 Introduction

High resolution MRI provides valuable characteristics of the orbital structures *in vivo* and has led to important discoveries of the biomechanics of the oculomotor plant [Miller, 1989; Clark et al., 2000; Piccirelli et al., 2007]. Different configurations of the orbit in various eye positions can be captured in volumetric data. Figure 4.17 shows the reconstructed models of two horizontal EOMs in three gazes. Deformation due to EOM contraction and elongation is

observed. We suggest that these different deformed states of the orbit not only present the shapes of the orbital tissues, but also encode mechanical characteristics of the EOMs. In Section 4.3.3, we have shown that EOM mechanical properties, such as strain fields, can be estimated by correlating the static tissue configurations across eye positions. In the rest of this section, we demonstrate that the material properties inferred from models can be applied back onto the models to improve their realism and make them more useful in biomechanical simulation.

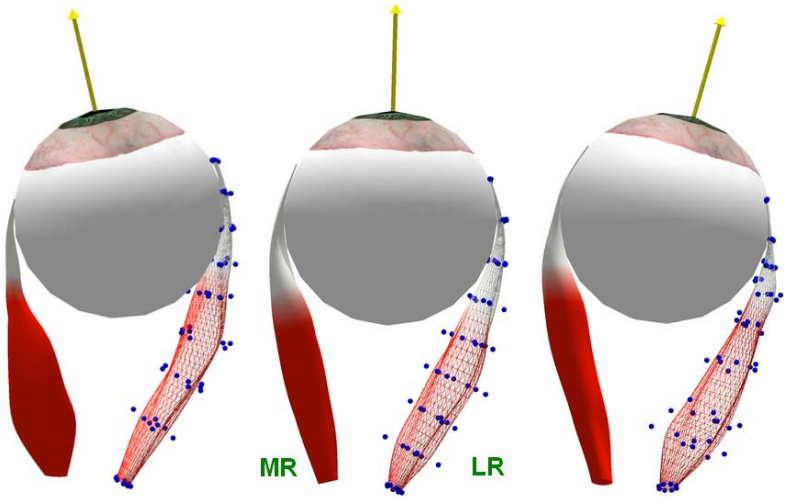

(a) (b) (c)

Figure 4.17: Reconstructed surfaces of two horizontal EOMs, medial rectus (MR) and lateral rectus (LR), in the (a) adduction, (b) primary, and (c) abduction gazes. (b) and (c) are the same as the ones in Figure 4.15 but rendered differently.

There are numerous discrete representations of the shape of an object on a computer, if no additional constraints are imposed. For instance, both a polygonal mesh and a parametric surface can model and visualize the same object at sufficiently good accuracy. Note that in Figure 4.17b and Figure 4.17c the surfaces of the lateral rectus (LR) muscle have no correspondences to each other; the control points are arbitrarily distributed as long as the overall shape

closely approximates LR. In other words, these reconstructed surfaces are independent of each other. We show that these models can be correlated to be more useful. If we apply material constraints, such as the deformation property introduced in Section 4.2, we can register LR surface in adduction gaze to the LR surface in primary gaze in a physically consistent way. The resultant surface shown in Figure 4.17a realistically shows how LR deforms from the primary gaze to the adduction gaze. All control points move consistently towards the medial direction, which is the elongation direction. Such a model is more meaningful than the unregistered LR surface in Figure 4.17c.

These physically realistic models are discretized in material coordinates and provide immediate correspondences. Building such consistent models can ease discretization for biomechanical simulations using FEM [Schutte et al., 2006; Blemker and Delp, 2005] or strands [Sueda et al., 2008]. Furthermore, although MR images in only a few key eye positions are acquired, given the correspondences, we can generate realistic intermediate configurations to animate continuous EOM deformation by using interpolation techniques.

Establishing the mapping between two models has been studied in digital geometry processing; it has wide applications from texture transfer to shape analysis [Sheffer et al., 2006]. Various techniques for registration [Allen et al., 2003] and parameterization [Praun et al., 2001; Sheffer et al., 2006] have been developed. However, these approaches cannot be directly applied for our purpose because they use geometric features that do not necessarily correspond to physical materials. A flexible framework that incorporates nonuniform stiffness in mesh deformation is presented in [Popa et al., 2006]. Positions of the vertices on triangular meshes are optimized to follow the transformations of

anchor triangles specified by the user while the material constraints are satisfied. It is developed for easy control of mesh manipulation to generate new poses instead of reparameterizing existing meshes. Taking advantage of the specific applications to generalized cylinders and efficient parametric surface representation, we derive a simple constrained parametric surface fitting formulation instead.

4.4.2 Methods

Figure 4.18 gives an overview of our approach. It consists of three parts. We first reconstruct geometric models of the target tissue from imaging data acquired in different deformed configurations. Then we estimate tissue deformation using the approach introduced in Section 4.2. Finally, the estimated tissue motion is applied to reparameterize the reconstructed model to improve its physical realism. If multiple configurations are available, a consistent discretization in the material coordinates is achieved across different deformation states.

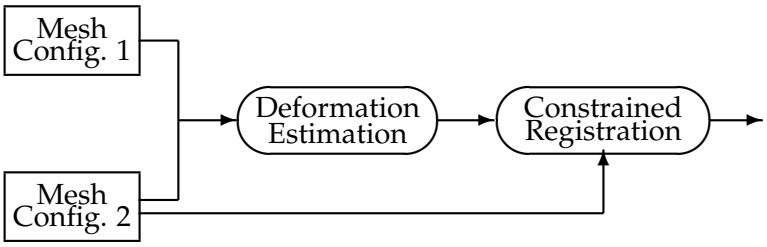

Figure 4.18: Overview of our physically constrained registration approach

4.4.3 Physically Consistent Registration

The reconstructed models from different gazes have no correspondence between them, as shown in Figure 4.17. The fitting process only optimizes the

closeness of the mesh to the boundary for one set of images. We realize that the estimated strains relate the deformation configurations to each other and can be used to improve the physical realism of the reconstruction.

Given the estimated axial strain, we reparameterize the reconstructed surface in the second configuration by constraining the nodes on the mesh to move consistently with the strain field. We use the estimated displacement field instead of strains because we need the information about where the nodes are supposed to move. The strain/displacement fields are estimated at the discrete partitions. They are interpolated by splines which give a good approximation to the continuous fields in the one-dimensional axial material coordinates. In other words, we have a mapping from the axial coordinate to the estimated displacement field. For every control point and vertex on one surface, we first project it onto the medial axis to calculate its axial coordinate. Then we get its axial displacement from its current position to the other configuration based on the mapping.

The axial displacement does not constrain movement in the transverse direction. Therefore, we formulate the displacement constraint as being on a plane perpendicular to the axis. q is a surface point and m_q is q's projection on the medial axis. m'_q is m_q's predicted point on the axis following the estimated displacement field. The destination plane of q passes through m'_q and is perpendicular to the medial axis. Let $\overrightarrow{n}(m'_q) = [A, B, C]$ be the axis tangent at m'_q. The predicted plane function of q is calculated as $Ax + By + Cz - \overrightarrow{n}(m'_q) \cdot m'_q = 0$.

Our reconstructed models are represented as tensor product bicubic B-spline surfaces that are linear parametric surfaces. A surface point is a linear function

of the control points. Therefore, instead of constraining surface points, we impose constraints on the control points. The original surface fitting problem in Equation 3.7 is augmented as a constrained optimization problem,

$$\begin{aligned} \min_{P} \quad & \|AP - c\|_2^2 + \alpha F_{smoothness} \\ s.t. \quad & A^i P_x^i + B^i P_y^i + C^i P_z^i + D^i = 0, i = 1, ..., N \\ & P_{xmin} \leq P_x^i \leq P_{xmax}, \\ P^i \in \mathbb{R}^3 : \quad & P_{ymin} \leq P_y^i \leq P_{ymax}, \\ & P_{zmin} \leq P_z^i \leq P_{zmax}. \end{aligned} \tag{4.4}$$

The objective function is same as that of Equation 3.7, except that s is a list of sample points from the mesh in the second configuration. The first set of equality constraints states that a control point $P^i(P_x^i, P_y^i, P_z^i)$ should be on the plane $A^i x + B^i y + C^i z + D^i = 0$. The other constraints enforce lower and upper bounds on the variables so that they are solved within the feasible range near the reconstructed surface. We use the QL package [Schittkowski, 2005], which implements the primal-dual method of Goldfarb and Idnani, to solve this convex quadratic programming problem. The solution is the reparameterized surface of the second configuration, representing realistic axial deformation.

Our formulation of the reparameterization problem is a simpler version of the variational surface modeling approach [Welch and Witkin, 1992]. Variational modeling extremizes some fairness functions that are integrals of the surface, subject to geometric constraints. We model conforming to a surface as minimizing the stretch and bending from the rest shape. In our method, we treat the reparameterization as a constrained fitting problem and minimize the distance deviation from the surface, defined as the distance sum from some

sampled points on the surface.

4.4.4 Results

We first describe our validation experiment on registering the surfaces reconstructed from MR images of the rubber phantom presented in Section 4.3.1. Then we present results on the parameterization of orbit models.

Rubber Phantom Models

We reconstructed the surfaces of the rubber phantom from MR images at different elongation configurations. We use this example as a validation of our approach. We choose the models from the rest state and the most elongated state (1.33). Details of the phantom and imaging protocols are presented in Section 4.3.1. Although the originally reconstructed surfaces have the same control point arrangement (a grid of 8 by 8 control points), they have no correspondences to each other (see Figure 4.19a and Figure 4.19c).

We first specify the axial displacement constraints on the control points of the second state. The blue rectangles in Figure 4.19b show the target planes of the control points. The predicted displacements in Figure 4.20 are used to compute the axial positions of the planes. To simplify validation, the control points are initially arranged in rings orthogonal to the axis such that control points on the same ring are enforced to have the same axial coordinates. Therefore, there are fewer planes than the actual number of control points in Figure 4.19b, since some of them share the same plane.

We then apply the physically consistent registration approach and reparameterize the second model shown in Figure 4.19c. We have two observations by comparing the resulting model in Figure 4.19d with the original model in

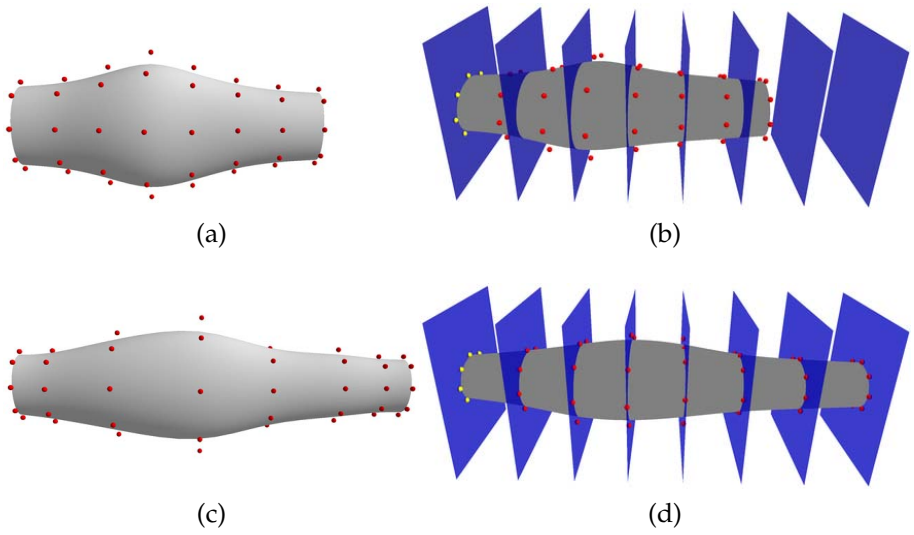

Figure 4.19: (a)(c) Reconstructed surfaces of the phantom in two states. (b) Displacement constraints of the control points. (d) Registered surface that fits to the shape while satisfying the displacement constraints.

Figure 4.19c. First, the new model closely represents the shape of the second configuration; this means that the reparameterization does not sacrifice modeling accuracy. Second, the control points correctly move to the assigned planes, obtained based on the estimated deformation. We conclude that the registered model in Figure 4.19d has direct material correspondence to the model in Figure 4.19a, accurately maintaining the geometric shape.

In Figure 4.20, we show that both the actual displacements of the control points solved by Equation 4.4 and the resultant surface points follow the constraints nicely.

Figure 4.21 presents the reparameterized surface in different colors to show the computed correspondences. Every point is assigned a color based on its initial axial coordinate. Each color segment represents a part of the object with uniform volume. Realistic nonuniform deformation is observed from the change of segment width. For example, the top green segment is stretched

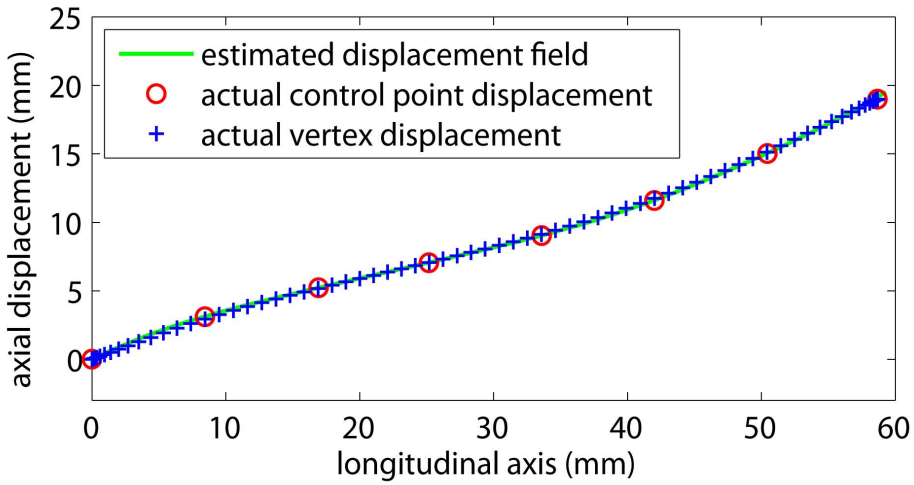

Figure 4.20: Estimated displacement field used as input, actual displacements of the control points, and the surface points after reparameterization.

more than the yellow green segment in the middle.

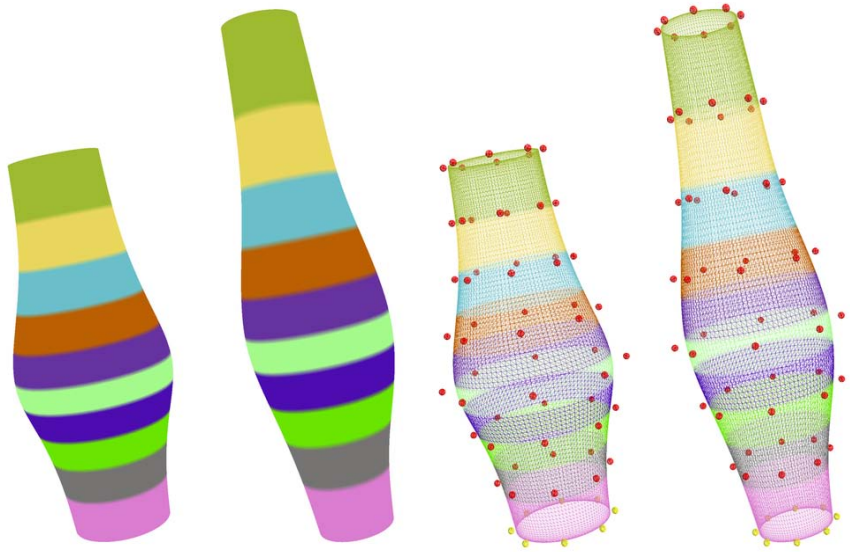

Figure 4.21: (a)(c) Surface in one configuration. (b)(d) Reparameterized surface in another configuration. Models are visualized in two different ways for better comparison.

Orbit Models

Figure 4.22 compares the originally reconstructed EOM surfaces to the physically registered surfaces in three eye positions. Control points are also displayed for ease of comparison. The registered models show realistic EOM deformation. The surface points move consistently with EOM contraction or elongation, satisfying the displacement constraint. Nonuniform stiffness is observed visually. On the contrary, in the unregistered model in Figure 4.22a, the tendon points inside the green dashed box show unrealistic negative stiffness. Moreover, the control points in the magenta oval move anteriorly closer to the globe, which is opposite to the actual EOM contraction direction.

Similarly, the difference in realism and consistency is shown in a different rendering scheme in Figure 4.23. We map chessboard textures to the surfaces to demonstrate the correspondences across eye positions.

In conclusion, the registered EOM models provide physically consistent correspondences of surface points and are more meaningful in visualizing deformation. They are ready to be used in biomechanical simulations to study EOM functions and to estimate parameters such as elasticity and forces, combined with the mechanical properties of other orbital structures.

4.5 Conclusions

We presented a simple and effective method for estimating longitudinal strains in musculotendons and other generalized cylinders, in cases where local correspondences are hard to find directly from images. The underlying idea is to find segment-to-segment correspondences utilizing the incompressibility of soft tissues. This approach is very practical since the geometries of soft tissues

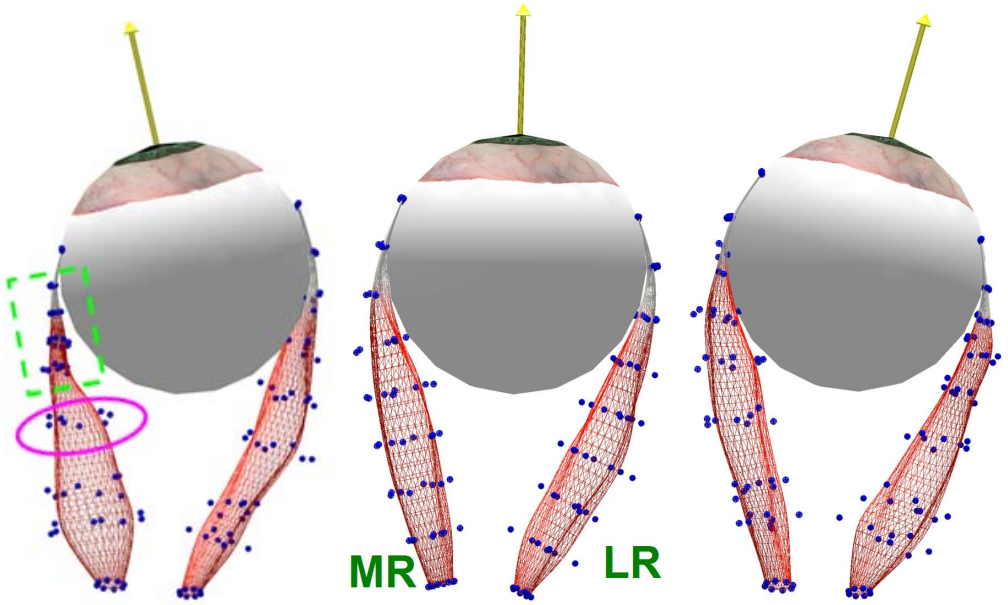

(a) Adduction (unregistered) (b) Primary (c) Abduction (unregistered)

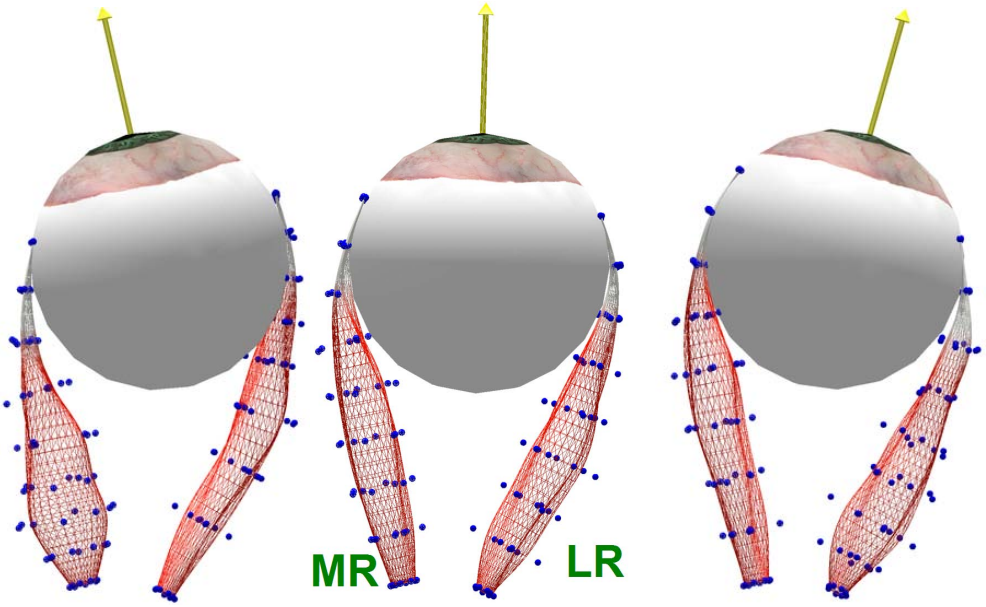

(d) Adduction (registered) (e) Primary (f) Abduction (registered)

Figure 4.22: (a)(b)(c) Original horizontal recti muscle models in adduction, primary, and abduction gazes. (d)(e)(f) Physically consistent models after registration.

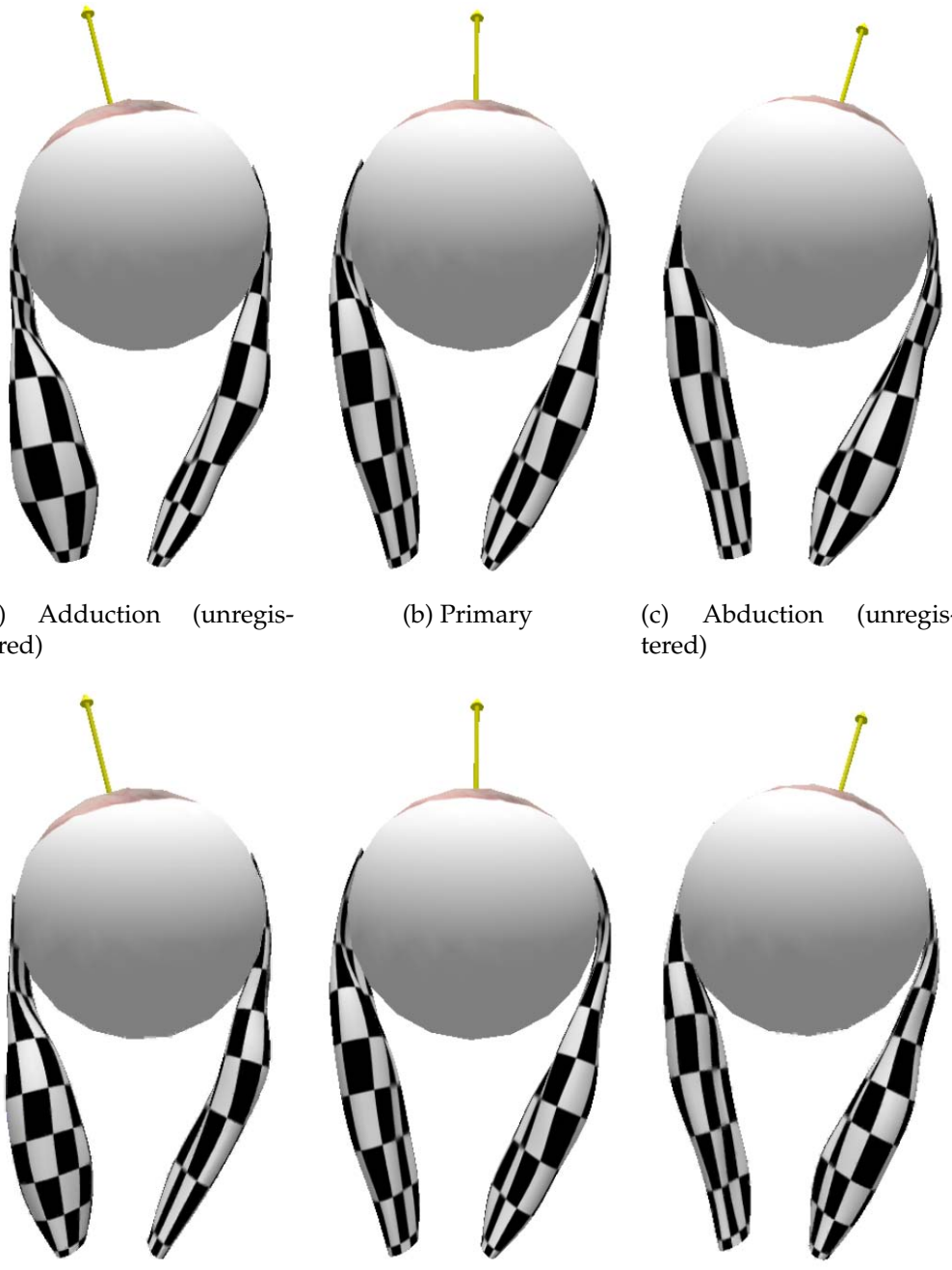

(a) Adduction (unregistered) (b) Primary (c) Abduction (unregistered)

(d) Adduction (registered) (e) Primary (f) Abduction (registered)

Figure 4.23: (a)(b)(c) Original horizontal recti muscle models in adduction, primary, and abduction gazes. (d)(e)(f) Physically consistent models after registration.

can be obtained conveniently either from medical images or recently developed laser reflectance system for measuring cross sections [Pokhai et al., 2008].

We demonstrate the usefulness of this method by estimating extraocular muscle strains using models reconstructed from MRI of human subject. Nonuniform strains are observed in both shortened and elongated EOMs. Simulated sensitivity analysis shows that with moderate noise, the algorithm produces small errors. Validation on MR images of a rubber phantom further proves the accuracy of our approach.

We also present an approach to realistically model extraocular muscles in different deformation states by using the estimated axial strains and applying physically constrained registration. We achieve a consistent parameterization across different configurations. The discretization is in material coordinates, and thus makes the resulting models suitable for biomechanical simulations.

The proposed method is limited to one-dimensional longitudinal strains and lumped in the transverse directions. It is designed for tendons, ligaments, and fusiform muscles such as the biceps brachii and extraocular muscles. In these muscles, fibers are arranged nearly parallel to each other. Our method cannot accurately predict strains from muscles with more complex architectures.

Chapter 5
3D Biomechanical Simulator of Oculomotor Plant

5.1 Introduction

In order to fully understand the biomechanics and neural control of the oculomotor plant, it is necessary to develop a computational model that describes the underlying mechanism, interprets empirical observations, and verifies scientific hypotheses [Haslwanter, 2002; Miller et al., 2003]. Such a model is required to accurately represent the anatomical and neurophysiological findings of the eye. It also should be capable of realistically simulating different kinds of eye movements under both normal and pathological situations.

Our study is motivated by the need of a realistic and accurate model with all desired properties. Previously developed models have limitations in different aspects, which restrict their applications to many important issues. For instance, the recently discovered pulley connective tissues are believed to have kinematic functions that are important to the oculomotor plant. MRI and histological studies have looked at the anatomical and physiological properties of these pulley tissues [Miller, 1989; Clark et al., 2000; Kono et al., 2002b,a; Demer, 2004] and suggested their possible functions in simplifying the ocular motor control [Kono et al., 2002a; Demer, 2004, 2007]. Clinical evidence also shows that pulley pathology is associated with certain strabismus patterns, which calls for attentions to the functions of pulleys. However, there has not

been a model that realistically implements the pulley mechanics.

We develop a new biomechanical simulation framework that addresses the limitations of previous models. Our orbital simulator incorporates realistic nonlinear anatomical and mechanical properties of the ocular plant. Individualized parameters, such as the extraocular muscle geometries and pulley pathologies, can be easily included. The simulator supports simulation of various kinds of eye movements, including fixations, smooth pursuits, and saccades. The model is sufficiently flexible such that the pulley hypotheses can be implemented and examined.

5.1.1 Related Work

Computation has played an important role in improving our understanding of the mechanics and control of eye movements. Robinson [1975] performed the first quantitative study of the extraocular muscle cooperation and prediction of strabismus surgery, using digital computers. From his modeling work, Robinson realized that the conventionally believed shortest path hypothesis on EOM paths would have produced large side-slips that were unrealistic. He then proposed a "permitted side-slip" model, which constrains EOM side-slip. Later, using magnetic resonance imaging and computerized 3D reconstruction, Miller [1989] found that the rectus muscle bellies are quite stable in the orbit even with large ocular rotations. Based on this observation, Miller first proposed that muscle sheaths at, and posterior to, the equator of the globe — which he named "pulleys" — couple rectus muscles to the orbital wall and constrain the transverse shift of muscle path. This is the foundation of the modern notion of extraocular muscle pulley theory, and has inspired the reexamination of orbit anatomy and revolutionized study of ocular motility.

Robinson's model [Robinson, 1975] is the groundwork of several other 3D models of the oculomotor plant that have been developed in the past two decades. These models have played an important role in providing insight and scientific bases for better understanding oculomotor biomechanics, control of eye movements, and strabismus. Existing models can be categorized in the following two types, based on their anatomical and physiological realism.

Simplified models. Models using simplified anatomical and EOM mechanical properties of the orbit have been developed [Schnablok and Raphan, 1994; Raphan, 1998; Quaia and Optican, 1998]. These models assume that three pairs of EOMs act on three planes that are orthogonal to each other. They also do not take into account the anatomical variations of different EOMs, such as muscle lengths and cross sectional areas. Another critical assumption to simplify the analytical solution is that the EOM force is simply proportional to the muscle innervation, whereas the actual EOM mechanics is quite complex. Such models have the advantage of supporting dynamic simulations and have been used to study neural control of saccades and pulley hypothesis [Raphan, 1998; Quaia and Optican, 1998]. These simplifications, however, may limit the models' accuracy and plausibility, as has been illustrated by Quaia and Optican [2003]. An improved model with anatomically accurate EOM geometries and advanced EOM dynamics is also proposed [Quaia and Optican, 2003] and compared with previous simplified models. However, the EOM constitutive model is still an approximation of the actual properties.

Biomechanical models. The first computerized biomechanical model due to Robinson solves for equilibrium of net force on the orbit [Robinson, 1975]. It incorporates anatomically realistic muscle paths and empirical EOM innervation-length-tension relationships to study normal binocular alignment, strabismus

and its surgical corrections. Two models were developed independently that improved Robinson's model, Miller and Robinson's SQUINT model [Miller and Robinson, 1984] and Simonsz's model [Simonsz and Spekreijse, 1996]. The SQUINT model was further extended to a widely used software tool, called the *Orbit*^{TM} gaze mechanics simulation, to provide a graphical user interface and implement passive pulleys [Miller et al., 1995]. Porrill et al. [2000] implement some functions of *Orbit*^{TM} in MATLAB for theoretical study on the separability of EOM control. SEE++ is a Windows-based modern software package developed from *Orbit*^{TM} [Haslwanter et al., 2005] that aims to provide highly interactive computer simulation environment for strabismus surgeries. Lately, Quaia et al. [2008] present simulation of superior oblique palsy using a model refined from their previous work [Quaia and Optican, 2003]. All of the above models are restricted to static fixations only and could not simulate dynamic eye movements which is supported by the simplified models. They all follow the computational procedures of Robinson's original model. EOM innervations are solved for three agonist-antagonist pairs and Sherrington's reciprocal innervation law is applied.

5.1.2 Outline

We develop two biomechanical models of the ocular plant with different implementation of pulley connective tissues. The remainder of the chapter is organized as follows. In Section 5.2, we introduce background knowledge including the ocular biomechanics and the strand simulator. The first model (called the *idealized pulley model*) that represents pulleys as prismatic joints is descrbied in Section 5.4. Simulated fixation and saccadic movements are presented in Section 5.4.1. In Section 5.5, we describe another strand-based model

(called the *physiological pulley model*), which represents pulleys as elastic suspensions. System validations on the pulley locations as well as representative strabismus alignment simulation are shown in Section 5.5.4.

5.2 Background

5.2.1 Ocular Biomechanics

In this section, we introduce the key mechanical properties of the components in the oculomotor plant including the eyeball (globe), passive tissues of the eyeball, extraocular muscles, pulley connective tissues, and motoneural innervations. A comprehensive review can be found in [Robinson, 1981].

The eyeball is a nonrigid spheroidal structure, filled with vitreous that contains 98% of water. The moment of inertia of the eyeball is small and negligible in the highly damped plant. The passive connective tissues of the eyeball apply a restoring force that brings the eyeball back to the central position when the net force from EOMs is zero. The static mechanical properties of these restraining tissues have been studied by passively rotating the eyeball and recording forces at various positions [Robinson et al., 1969; Collins, 1971]. Force-length relationships are reported [Robinson et al., 1969; Collins, 1971]. The quick release experiment was conducted to analyze the dynamic mechanical properties of the passive orbital tissues [Robinson, 1964; Collins, 1971]. Experimental data on monkey eyeball mechanics is published recently [Sklavosa et al., 2005; Quaia et al., 2009a]. Based on the empirical data, constitutive models of the restraining tissues were proposed and they consist of one or more viscoelastic elements [Robinson et al., 1969; Collins, 1971; Clark and Stark, 1974; Robinson, 1981; Sklavosa et al., 2005; Quaia et al., 2009a].

The three-element Hill muscle model [Hill, 1938] has been widely applied in describing the force generation mechanism of skeletal muscles. The Hill-type muscle constitutive model has been adopted to describe the extraocular muscle mechanics [Robinson, 1964; Cook and Stark, 1967; Clark and Stark, 1974; Collins et al., 1975; Robinson, 1981]. It consists of an active contractile element (CE), a series elastic element (SE), and a parallel elastic element (PE). See Figure 5.1 for a representative model.

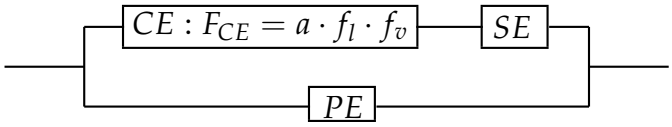

Figure 5.1: Three-element Hill-type muscle constitutive model. CE: contractile element; PE: parallel elastic element; SE: series elastic element.

CE describes the active muscle force. It depends on the muscle activation dynamics (a), the active force-length relationship f_l, and the active force-velocity relationship f_v. PE models the passive muscle force, which is characterized by the passive force-length curve. The active force-length and passive force-length relationships have been measured from human subjects and cats [Robinson et al., 1969; Robinson, 1975; Collins et al., 1975]. More recent work on the nonlinear viscoelastic stress-strain behaviors of extraocular muscles includes experiments on bovine EOMs [Yoo et al., 2009] and monkey EOMs [Quaia et al., 2009a,b]. Models of f_v have been proposed based on Hill's force-velocity curve of skeletal muscles, experimental data on rat EOMs, and maximum saccadic velocity of human eye [Clark and Stark, 1974; Robinson, 1981]. SE represents the passive muscle force from elastic elements in series with the contractile element. Tendons and connective tissues within muscles contribute to SE. EOM tendons are extremely stiff, therefore the EOM SE element

is mainly in the muscle sarcomeres. Unfortunately the series elastic element of EOMs has not been well quantified [Robinson, 1981].

5.2.2 Strand Simulator

One key issue in developing a realistic oculomotor plant model is the simulation of extraocular muscle mechanics. We model EOMs, consisting of parallel fibers, as a collection of musculoskeletal "strands" – novel computational modeling primitives for musculoskeletal simulations [Pai et al., 2005; Sueda et al., 2008]. EOM orbital and global layers as well as pulley connective tissues can be conveniently incorporated.

The first strand model, called the *Cosserat strand*, is a fiber-like, volumetric, incompressible structure [Pai, Sueda, and Wei, 2005]. It curves in 3D and makes contact with its neighbors. The Cosserat strand is based on Cosserat theory of elastic rods. Figure 5.2 shows a Cosserat strand. Each strand has a collection of *nodes*, which are fames embedded in the material. The *segment* between any two nodes defines the viscoelastic coupling of the nodes; it also models the local musculotendon geometry. Free Form Deformation (FFD) is used for smooth local deformation of segments with approximate volume preservation. The Cosserat strand offers both the efficiency of line-based muscle models and the realism of physically based deformable solids.

The more recently developed *Spline strand* is based on a spline with inertia [Sueda et al., 2008]. We use this new strand model for all the simulations presented in this chapter. Each strand represents a part of the musculotendon aligned with the fibers. Depending on the level of detail needed, a strand can be as fine as a single fascicle or as coarse as an entire muscle. The geometry

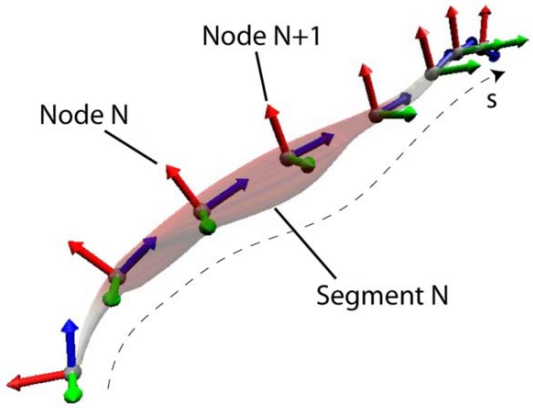

Figure 5.2: A Cosserat strand.

of a strand is described by a cubic B-spline curve that models realistic one-dimensional muscle path. The generalized coordinates, positions and velocities, of the strand control points define the strand dynamics. A strand may only need a few control points to model the musculotendon geometry and compute the underlying continuous mechanical states. This parametric representation makes the strand simulator efficient. Figure 5.3 shows a Spline strand that follows the medial axis of an extraocular muscle.

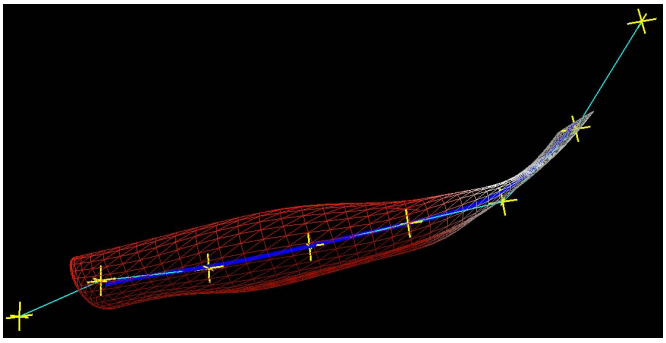

Figure 5.3: A Spline strand (in blue). It has eight control points, shown as the yellow crosses.

Empirical muscle constitutive models, such as the force-length and force-velocity relationships introduced in Section 5.2.1, can be specified on a strand

and included in the strand dynamics computation. Various kinds of mechanical constraints are supported to model complex interactions of the structures, such as mechanical couplings and surface contacts. See [Sueda et al., 2008] for more details of the Spline strand.

5.3 Strand-based Biomechanical Orbit Model

In this section, we describe a novel three-dimensional biomechanical simulation framework of the oculomotor plant for studying the mechanics and neural control of ocular motility and assisting strabismus surgical treatment. We use the *Spline strand* [Sueda et al., 2008] to model extraocular muscle mechanics. Our proposed model has the following desirable properties:

- Strand-based EOMs are associated with realistic subject-specific muscle anatomy, such as paths and cross sections. Individualized EOM anatomy is important for customized surgical planning.
- Physiologically accurate EOM constitutive models are incorporated.
- Latest discoveries of the oculomotor plant, such as the pulley hypothesis, can be easily implemented.
- Contact between EOM tendon and the globe is physically modeled, not only for visualization but also for realistic simulation.
- More importantly, our biomechanical model can simulate dynamic eye movements. Dynamic simulation has not been supported by previous biomechanical models.

We develop two strand-based biomechanical models. The difference lies mainly in the implementations of the pulley connective tissues. Figure 5.4 compares these two models.

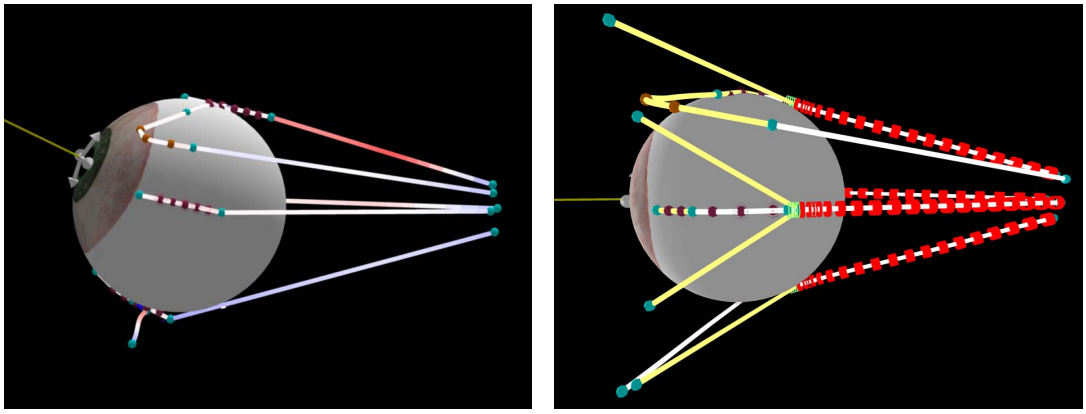

(a) Idealized pulley model (b) Physiologically realistic pulley model

Figure 5.4: Strand-based biomechanical models of the orbit. (a) First model with idealized pulleys implemented as prismatic joints. (b) Second model with physiologically realistic pulleys implemented as passive suspensions.

In the first model shown in Figure 5.4a, pulleys of the rectus muscles are represented as prismatic joints. These joints allow one-dimensional sliding motion along the joint axis and zero movement in the transverse direction. We call it the *idealized pulley model*, because it abstracts the mechanical functions of the rectus muscle pulleys and neglects the small transverse displacements of pulleys. Due to its simplicity, fewer undetermined parameters are introduced into the model, which makes it suitable for studying the dynamics and neural control of ocular motility.

The second model in Figure 5.4b uses passive elastic springs to model pulleys in a complicated mechanical arrangement. Mechanical linkages of the rectus muscles to the orbital wall and the intermuscular couplings are explicitly represented. Compared with the first model, the second one is a more realistic implementation of the connective tissues architectures in the orbit, revealed

by MRI and histological studies [Kono et al., 2002b; Miller et al., 2003; Demer, 2004]. The second model correctly incorporates the active pulley hypothesis [Demer et al., 2000; Demer, 2004] and allows transverse shifts of rectus muscle pulleys. Small amounts of pulley shifts are observed from MRI of human subjects under normal physiological conditions [Clark et al., 2000]. We name this model the *physiological pulley model*. It can be used to understand the active pulley hypothesis and facilitate surgical treatment of strabismus caused by pulley pathologies.

In the remaining context of this section, we introduce the common modeling strategies and model properties shared by these two models. In Section 5.4 and Section 5.5, we describe their specific characteristics and simulation results.

5.3.1 Model Description

In our biomechanical model, each extraocular muscle is modeled as one or more strands. Other ocular structures are defined as mechanical constraints. In the following, we use the first model with idealized pulleys shown in Figure 5.5 to describe the common model components.

a. The globe is approximated as a spherical rigid body (radius = $12.43mm$) with a ball-and-socket joint allowing rotation around its center of mass in three dimensions. The globe is actually nonrigid. However, because the moment of inertia of the globe is small, modeling the globe as a rigid body only introduces trivial errors. The translational movement of the globe is assumed negligible. The elasticity of the passive suspensory tissues of the globe is $0.5g/deg$ [Robinson, 1981]. Six extraocular muscles exert torques on the globe through attachment constraints.

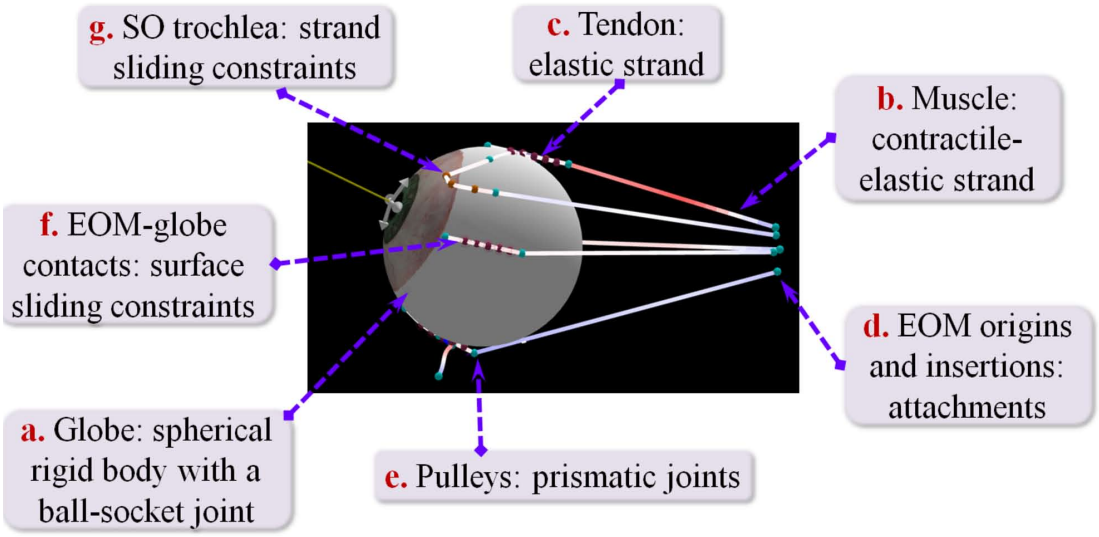

Figure 5.5: Biomechanical model of the orbit using strands and mechanical constraints.

b. Each of the four rectus muscles has two contractile-elastic strands modeling the global and orbital layers [Kono et al., 2002b]. The constitutive model of the EOM strands will be discussed in Section 5.3.1. The superior oblique (SO) muscle and the inferior oblique (IO) muscle are each associated with one contractile-elastic strand. Subject-specific EOM anatomy, such as EOM path and size defined by cross sectional areas, can be incorporated for individualized surgical treatment prediction. The cross sectional area is a variable along the strand, which allows simulation of realistic EOM deformation locally.

c. Each EOM, except for the IO muscle, has a non-contractile, nearly inelastic strand modeling the tendon. The tendon strand of the SO muscle is quite long ($30mm$). The IO muscle has a very short tendon ($1-2mm$) that is assumed negligible.

d. EOM origins and insertions are implemented as attachment constraints,

which couple their positions to the attachment sites.

e. By using strands to model EOMs and applying additional constraints, we can incorporate the pulley models (see [Miller, 2007] for a review) that have been proposed.

f. Contact between the extraocular tendons and the globe is handled to prevent penetration. A parametric B-spline surface is used to represent the geometry of the globe for computing contact locations on the fly. Surface sliding constraints are specified on the EOM tendon strands such that tendons always slide on the globe without penetrating. Our model is the first that deals with EOM-globe contact interaction.

g. The superior oblique trochlea is modeled as a sliding constraint to enforce SO tendon to pass through the trochlea of superior oblique that is fixed in the orbit.

EOM Strands

We have two types of strand elements in the model, *contractile-elastic strands* and *non-contractile elastic strands*. A contractile-elastic strand models muscle fibers; its total force is the sum of the active force and the passive force $F_m = F_{CE} + F_{PE}$. The series elastic (SE) element in the three-element Hill model illustrated in Figure 5.1 is not included in our EOM constitutive model. As Robinson [1981] has pointed out, the force mechanism of the EOM series element has not been quantified well due to the lack of physiological data. As a result, it is difficult to derive a reasonable model for the SE element. None of the existing biomechanical models has incorporated the SE component because of its indeterminacy, and we follow this common choice.

As introduced in Section 5.2.1, the active force of the contractile element (CE) is a function of the muscle activation a, active force-length (FL) relationship f_l, and active force-velocity (FV) relationship f_v: $F_{CE} = a \cdot f_l \cdot f_v$. a is assumed to be a variable between 0 and 1. $a = 1$ means the muscle is fully innervated. Both f_l and f_v have complex nonlinear characteristics, so is the passive force F_{PE}.

We adopt the the active force-length curve of a fully innervated EOM and the passive force-length curve in the Orbit^{TM} 1.8 simulator [Miller et al., 1995], which best approximate published empirical data. Figure 5.6a shows the FL curves of a lateral rectus muscle, from which the physiological data was acquired [Robinson, 1975]. In our simulation, the muscle strengths of other EOMs are scaled automatically by the ratios of their maximum cross sectional areas to the LR maximum cross section. We slightly adjust the parameters of the force-velocity model in [Robinson, 1981] and use it in simulating saccadic eye movements. Figure 5.6b shows the FV curve.

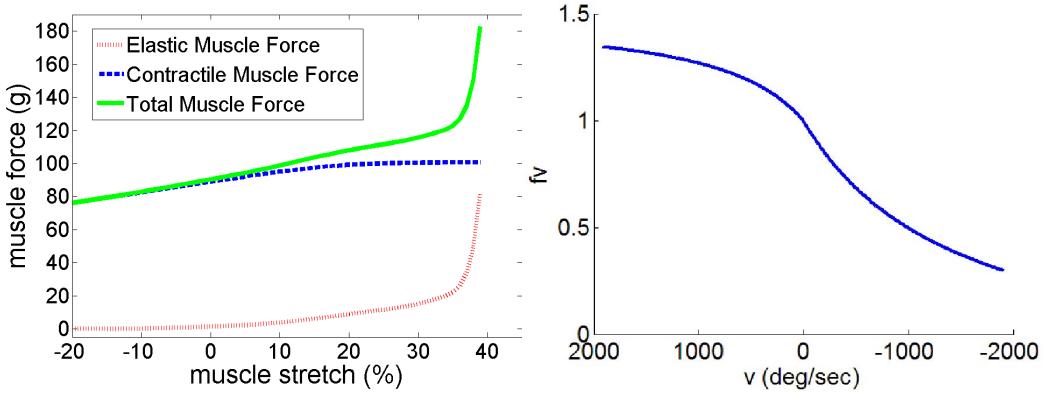

(a) Force-length relationship (b) Force-velocity relationship

Figure 5.6: (a) Force-length curves of EOMs, based on Orbit 1.8^{TM}. The contractile force is assumed on a fully innervation EOM. (b) Force-velocity relationship.

Non-contractile elastic strands are used to model tendons, pulley suspensions, and intermuscular bands. These strands are passively stretched because of the attachments; they do not actively contract to generate force. EOM tendons are very stiff and thus we apply high stiffness on the tendon strands. The mechanical properties of the pulley suspensions and intermuscular bands will be presented in Section 5.5.

5.3.2 Simulations

Two kinds of simulations are performed. In *inverse control simulations*, we compute the EOM innervations that hold the eye at the target position or follow the target trajectory. In *forward simulations*, given a set of EOM innervations, the equilibrium eye position or dynamic movement trajectory is computed.

We extend the activation (innervation) solver in Sueda et al. [2008] to compute innervations of the EOMs, $a \in [0,1]$ a unitless scalar, given the desired trajectory v_x, specified as the desired velocity of the globe:

$$\begin{aligned} \min_{a} \quad & w_a \|a\|^2 + w_x \|(H_x a + v_f) - v_x\|^2 \\ \text{s.t.} \quad & 1 \geq a_i > a_i^0 \; c_v(v_{eye}) \; c_p(p_{eye}) \end{aligned} \tag{5.1}$$

where w_a and w_x are blending weights and the lower bounds of the constraints are modulated as a function of eye velocity and position as described below.

The first term in the objective function minimizes the total activation such that among the numerous possible solutions, the set of innervations with the minimal summed energy are found. It also adds regularization to the quadratic problem. The second term guides the dynamics of the system towards the target motion. The matrix H_x can be thought of as the effective inverse inertia

experienced by the muscle activation levels in order to produce the target motion. The v_f vector is the velocity of the target due to the non-active forces acting on the system.

The constraint terms specify the innervation bounds of each EOM. The lower bound is non-zero to be consistent with the well known fact that the innervation in primary gaze at rest is not zero [Collins et al., 1975]. We denote this minimal innervation as a_i^0 for EOM_i. This lower bound is reduced to zero with increasing eye velocity so that lower bound is zero during saccades; such a constraint models the observation that an antagonist may completely cease firing during saccades [Sylvestre and Cullen, 1999]. We define

$$c_v(v_{eye}) = \max(0, \frac{v_{max} - |v_{eye}|}{v_{max}}), \tag{5.2}$$

$$c_p(p_{eye}) = \max(0, \frac{p_{max} - |p_{eye}|}{p_{max}}). \tag{5.3}$$

Here p_{eye} and v_{eye} are the position and velocity of the eye. v_{max} is the velocity defining the onset and offset of a saccade, which is set to $20^\circ/s$ [Sylvestre and Cullen, 1999]. The c_p factor linearly decreases the lower bound with the eccentric eye position. p_{max} is the maximum OFF direction eye position, at which the EOM's innervation is completely off; we assume $p_{max} = 30^\circ$ in our experiments.

In order to deal with the redundancy problem (3 degrees of freedom of the eye rotation vs. six EOMs), previous models [Robinson, 1975; Miller et al., 1995; Haslwanter et al., 2005] apply Sherrington's Law of Reciprocal Innervation by using a symmetric hyperbola function to explicitly define the innervation relationship of an agonist and antagonist pair. Realizing the deficiency of this symmetry assumption, Quaia et al. [2008] apply an asymmetric constraint and data-based heuristics on superior oblique/inferior oblique muscle innervation

computation. Our simulator does not incorporate the reciprocal control model but solves for the innervations of the six EOMs separately and simultaneously. Since we correctly model the orbital plant anatomy and physiology, the reciprocal innervation behavior of three EOM pairs is obtained automatically without being enforced as assumptions.

5.4 Idealized Pulley Model

The first model, called the *idealized pulley model*, represents the rectus muscle pulleys as prismatic joints. As the eye moves to different positions, a rectus muscle pulley moves longitudinally along the joint axis that is along the EOM tangent. The pulleys also restrict the transverse side-slip of the rectus muscles. Rectus muscle paths are inflected at pulley locations in secondary and tertiary gazes, consistent with MRI findings [Clark et al., 2000; Kono et al., 2002a].

In this model, we assume that the two contractile-elastic strands representing the global layer and orbital layer of a rectus muscle are anatomically and physiologically identical, and are always innervated equally. Therefore, the innervation variable, a in Equation 5.1, is a 6×1 vector corresponding to the six EOMs. The radius of each rectus layer strand is $\frac{1}{\sqrt{2}}$ times the radius of the whole rectus muscle such that the summed cross section of the two layer strands belonging to one rectus muscle equals the original cross section.

Figure 5.7 shows simulated horizontal eye movements. The influence of the pulleys on rectus muscle paths is clearly observed. As the eye rotates horizontally, the LR and MR pulleys move along the joint axes anteroposteriorly while the SR and IR pulleys remain stable in the mediolateral direction. The SR and LR pulleys cause sharp muscle path inflections – the posterior SR, IR muscle

bellies are stable relative to the orbit and their anterior paths follow rotation of the globe in eccentric gazes.

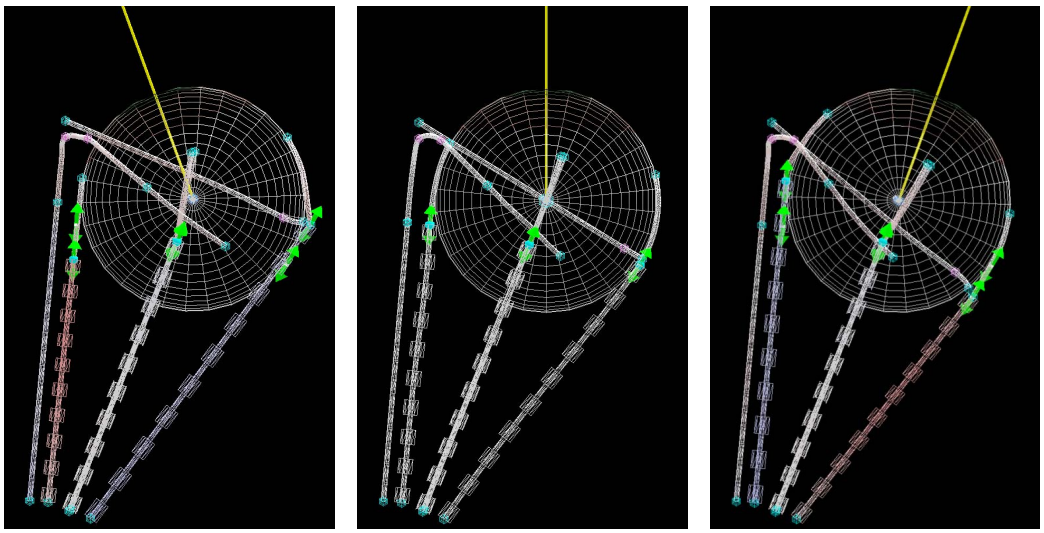

(a) Adduction gaze (b) Primary gaze (c) Abduction gaze

Figure 5.7: Simulated horizontal eye movements of the idealized pulley model. Rectus muscle pulleys are represented as prismatic joints, shown as green arrows. Note the inflection of the SR and IR muscle paths and anteroposterior movement using the LR and MR pulleys.

Figure 5.8 shows simulated vertical eye movements. Note that the LR and MR pulleys have no transverse side-slip in supraduction and infraduction gazes. Sharp inflections of the LR and MR muscle paths at their pulley locations are observed. The SR and IR pulleys move anteroposteriorly with the eye rotation.

In summary, by using prismatic joints to implement idealized pulleys, we apply zero longitudinal stiffness and infinitely large transverse stiffness on the pulleys to stabilize EOM paths. This simplified implementation of pulleys has the advantage of introducing fewer undetermined parameters while still capturing the main functions of pulleys.

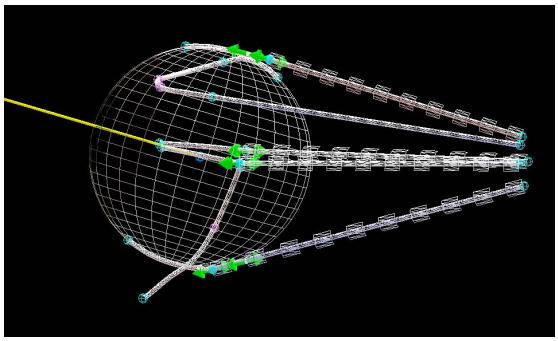

(a) Supraduction (elevation) gaze

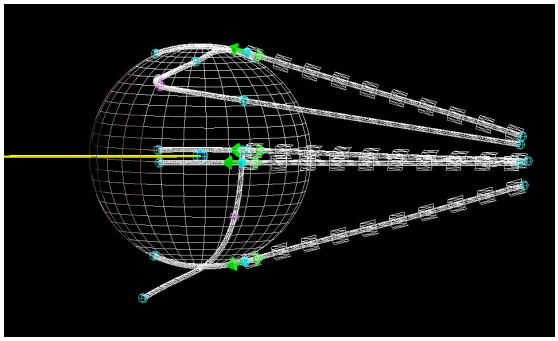

(b) Primary gaze

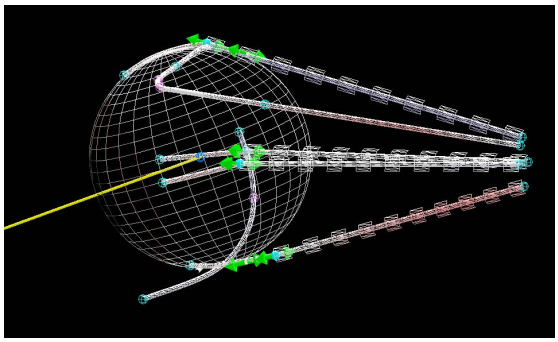

(c) Infraduction (depression) gaze

Figure 5.8: Simulated vertical eye movements using the idealized pulley model. Rectus muscle pulleys are represented as prismatic joints, shown as green arrows. Note the inflection of the LR and MR muscle paths.

5.4.1 Results

We validate the model by evaluating whether the simulated eye movements can reproduce empirical data. We first show that extraocular muscle strains in a simulated smooth pursuit movement are nonhomogeneous along the EOM

paths, consistent with the findings based on motion-encoded MRI (see Section 5.4.1. Simulation of fixations is presented in Section 5.4.1 to assess inversely computed muscle innervations. We then describe simulated saccadic eye movements using recorded abducens neuron firing rates as the control of the lateral rectus muscle in Section 5.4.1. The model generates realistic eye trajectories for saccades with different amplitudes. Realism of the orbital model is illustrated. Finally, in Section 5.4.1, we demonstrate that the idealized pulley model predicts both the static and dynamic deviation patterns of strabismus due to palsy of the superior oblique muscle (SOP). Surgical correction to eliminate vertical deviation caused by SOP is also simulated as a clinical application.

EOM Strains

Extraocular muscle deformation as a function of gaze and time is an important parameter in studying extraocular mechanics. We validate the dynamic EOM deformation pattern of our model by comparing simulation to the *in vivo* EOM motion data. Motion-encoded MRI was recently proposed to assess EOM motion during smooth pursuit eye movement [Piccirelli et al., 2007]. Sparse tissue points on the transverse imaging planes of tagged MRI were tracked as the subject was instructed to visually pursue a slowly moving stimulus. EOM deformation was inferred by analyzing recorded positions of the tissue points.

Stretch ratio, defined as the ratio between the deformed muscle length and its initial length, was used to quantify the deformation. Along the longitudinal axis in primary eye position, each EOM path was divided into three segments of equal length. Stretch ratios of the segments in the two horizontal rectus muscles were analyzed [Piccirelli et al., 2007].

We simulate the same smooth pursuit movement as in [Piccirelli et al.,

2007]. The eye moves horizontally from 20 degree in abduction to 20 degree in adduction with zero vertical movement. The velocity is a sinusoidal function with 2 second period. The maximum speed is $6.4 deg/sec$. Applying the same analysis scheme, we show the simulation results in Figure 5.9. For comparison, simulated EOM strains are overlaid on top of the *in vivo* EOM motion data reproduced from [Piccirelli et al., 2007].

Our simulated deformation of LR and MR muscles is consistent with the published data. All EOM segments have sinusoidal deformation pattern. Nonuniform shortening and elongation are observed in the two horizontal EOMs. The middle segment, which has larger cross sections, deforms more than the posterior segment. The anterior part contains more tendinous tissue and deforms the least. Our simulated deformation trends follow the MRI data. The disparity occurs at middle segments. Simulated LR and MR show larger deformation than the data. Due to low contrast, it is difficult to accurately identify EOM insertions from MR images. The tracking curves manually placed on the images (see Figure 2. in [Piccirelli et al., 2007]) show more posterior insertional ends than the actual insertions. We suspect that this variation in delineating muscle paths may partially contribute to the discrepancy in the analyzed muscle strains.

Simulation of Fixations

We simulate fixations at nine eye positions $\pm 20^{\circ}$ in a 3×3 grid. The EOM innervations that move the eye to each position are first computed from the inverse activation solver described in Section 5.3.2. Applying the computed EOM innervations, we then perform a forward simulation. Figure 5.10 shows the simulated fixation positions, which are close to the target positions. We

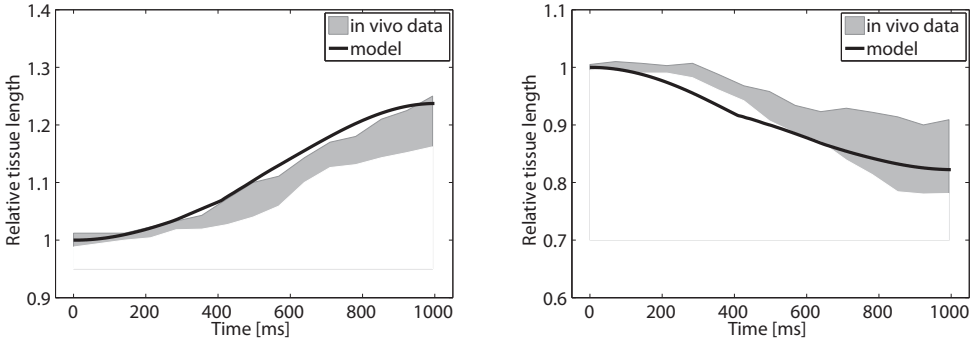

(a) LR Anterior Segment

(b) MR Anterior Segment

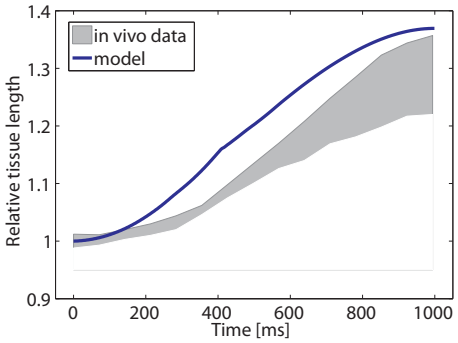

(c) LR Middle Segment

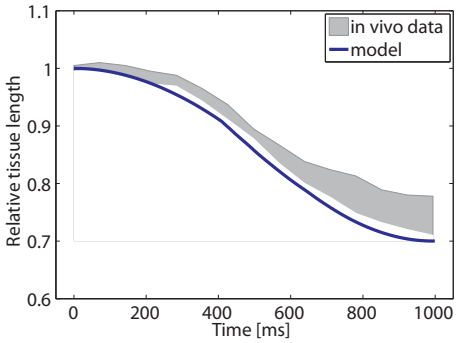

(d) MR Middle Segment

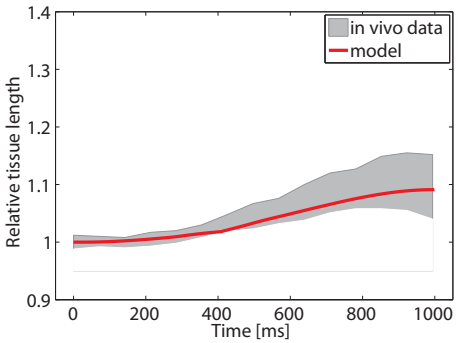

(e) LR Posterior Segment

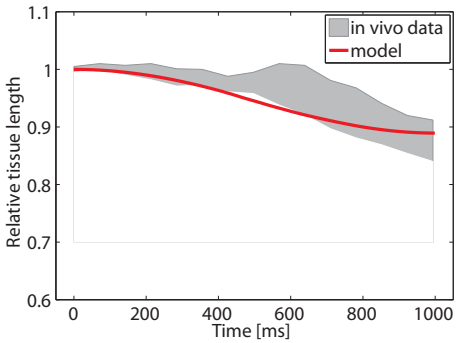

(f) MR Posterior Segment

Figure 5.9: Comparison of lateral rectus and medial rectus muscle strains from simulation and imaging data. Shaded regions show the average stretch ratios (mean $\pm 1 S.D.$) from 7 subjects over time (reproduced from [Piccirelli et al., 2007]). Solid curves show simulated strain. Values larger than one indicate muscle lengthening; values smaller than one indicate muscle shortening.

conclude that estimated EOM innervations are capable of stabilizing the eye at desired gazes.

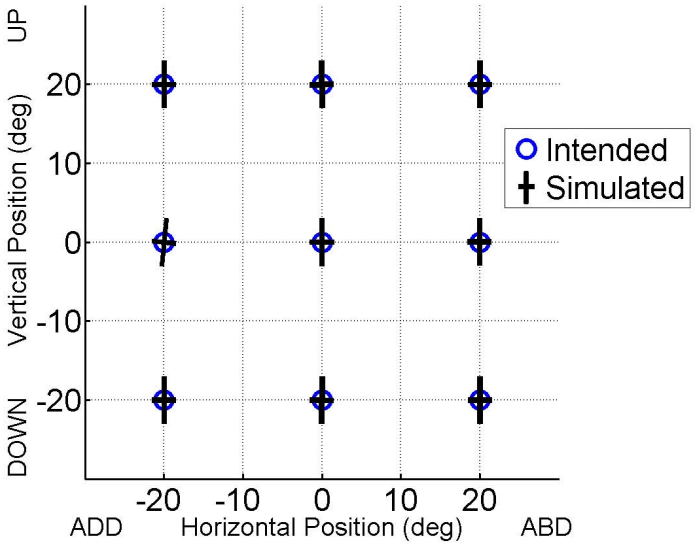

Figure 5.10: Simulated fixations using computed EOM innervations. Cyclorotation is shown as the tilt of the crosses.

Simulation of Saccades

The neural drive to produce a rapid saccadic eye movement can be characterized by a *pulse* component to overcome the viscoelasticity of the orbital plant, a *step* component to stabilize the eye in the new position, and a *slide* component that models the gradual transition between the pulse and step [Robinson, 1964].

The neural control of saccadic fast movement has been studied extensively [Robinson, 1964; Fuchs and Luschei, 1970; Sylvestre and Cullen, 1999]. The activities of neurons are characterized by discharge rates recorded at the neuronal sites. In particular, the abducens neuron discharges during saccades can be approximated as a first order equation [Sylvestre and Cullen, 1999]:

$$FR = b + kE + r\dot{E}. \tag{5.4}$$

The model approximates the abducens motoneurons (ABNs) firing rates as a linear function of the eye position E and velocity $\dot{E}$. b is a bias constant, which is the neural activities at stationary central eye position. k and r are constants and their optimal values have been estimated through fitting the above model to actual neuron discharge recordings.

Figure 5.11 shows simulation of an abduction saccade of 20 degrees while the eye is elevated by 20 degrees. This saccadic movement from a secondary position to a tertiary position is more interesting and challenging than a one-dimensional horizontal saccade. The torsional component in the tertiary gaze is a key parameter to evaluate the accuracy of an eye movement and plausibility of a biomechanical plant.

Figure 5.11a shows the saccadic trajectory which starts from a secondary position in 20 degree elevation. Figure 5.11b shows the approximated abducens motoneuron firing rate profile for a 20 degree saccade based on the model in Equation 5.4. The three coefficients of the model are $b = 156$, $k = 4.2$, and $r = 5.0$. Figure 5.11c plots our estimated innervations of LR and MR muscles, the major rectus muscles contributing to this horizontal saccade. Note that the computed LR innervation has the pulse-slide-step characteristics of saccadic neural control. Also note that the computed MR innervation realistically models the behavior of antagonist motoneurons during OFF direction saccades – most of them completely cease firing after saccade onsets [Sylvestre and Cullen, 1999; Horn and Cullen, 2009]. The model-based firing rate profile in Figure 5.11b is linearly scaled such that the starting and ending values match the computed innervation. The scaled profile is plotted in Figure 5.11c, overlaying on the estimated innervation for comparison. We observe that the

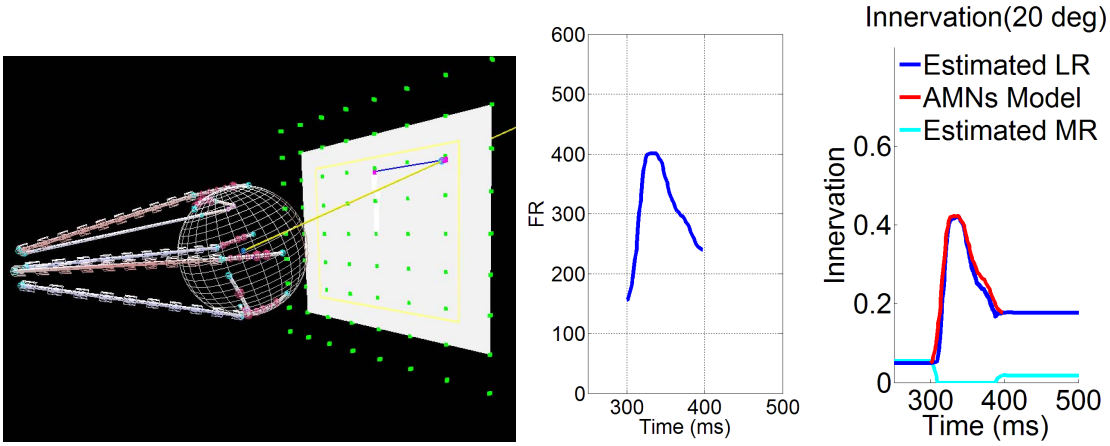

(a) 20 degree saccade (b) Model-based firing rate (c) Innervation

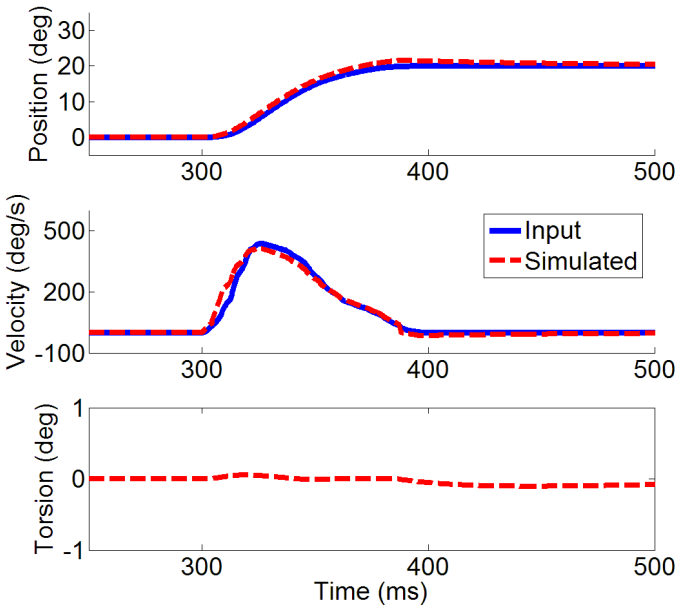

(d) Simulation validation

Figure 5.11: Simulated 20 degree abduction saccade in 20 degree elevation.

computed LR innervation dynamics agrees with the fitted empirical ABNs discharge dynamics. We use the scaled empirical neural discharge profile as the neural drive of LR and simulate the 20 abduction saccade. The simulation results in Figure 5.11d show that the simulated saccade treasonably follows the

desired saccadic trajectory. Note that associated torsion is very small, which further demonstrates the accuracy of the simulation and plausibility of the plant model.

We also simulate abduction saccades at other amplitudes, 10 and 30 degrees. Simulation results are shown in Figure 5.12 and Figure 5.13. Agreement on the eye position and velocity trajectories is also achieved.

One interesting observation is that the inversely computed saccadic control has a short delay from the empirical ABNs discharges. One possible explanation is that the delay is due to the dynamic coupling of the LR and MR innervations. Looking at the innervation plots in Figure 5.13c for instance, we see that the LR innervation does not start climbing until MR completely ceases firing. When the eye is moving at lower speed at the beginning of an abduction saccade, both the LR increment and the MR decrease contribute to the lateral movement. There are many possible combinations of the six EOM innervations, as long as the net force from the EOMs and the passive orbital tissues drives the orbital plant to achieve the same movement. Because we do not apply Sherrington's reciprocal innervation law explicitly, the control solver knows nothing about the paired agonist-antagonist EOMs. It treats all EOMs independently and picks one solution based on its formulation.

Simulation of Superior Oblique Palsy

In the following, we study a pathological case caused by abnormal EOM neural control. When the innervation of an EOM is impaired (completely lost), it is said to have *paresis* (*paralysis*). Although the pathology is due to muscle innervation, EOM palsy changes the mechanical properties of the oculomotor plant and consequently affects the ocular motility. More specifically, because

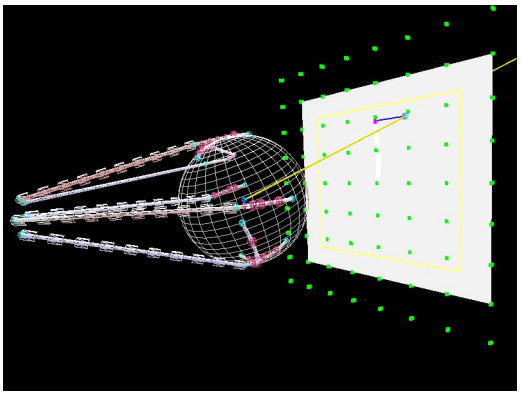

(a) 10 degree saccade

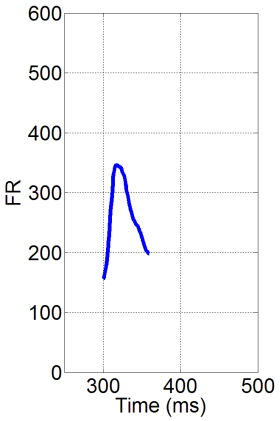

(b) Model-based firing rate

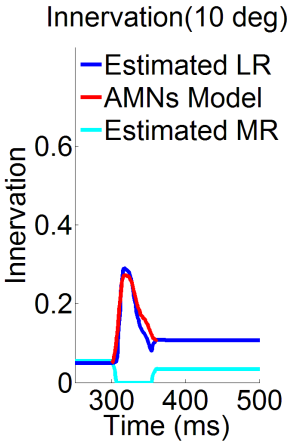

(c) Innervation

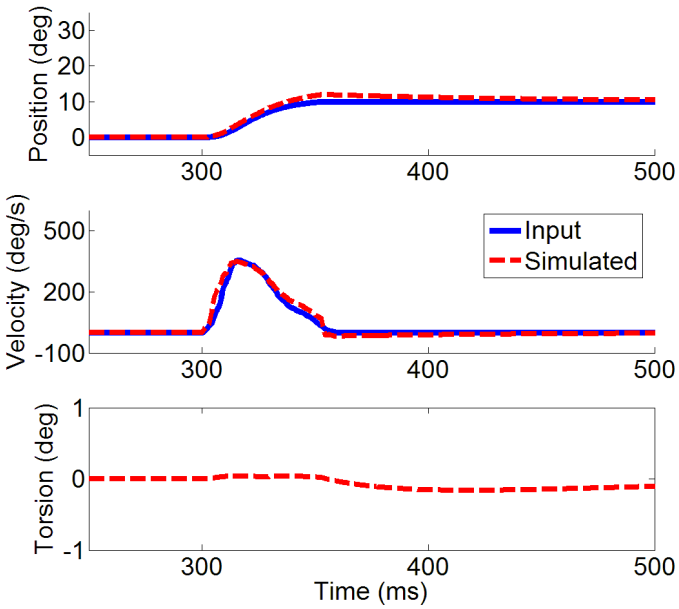

(d) Simulation validation

Figure 5.12: Simulated 10 degree abduction saccade in 20 degree elevation.

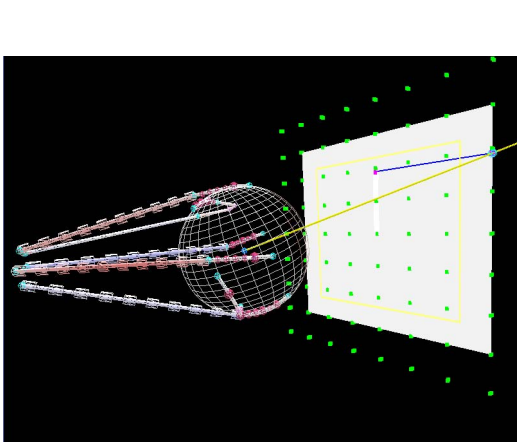

(a) 30 degree saccade

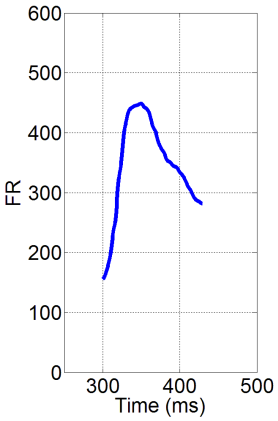

(b) Model-based firing rate

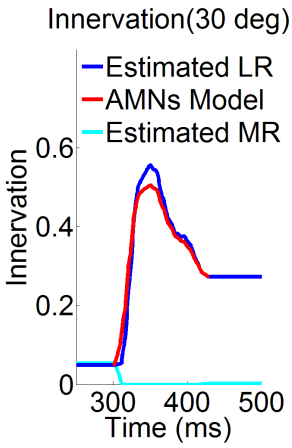

(c) Innervation

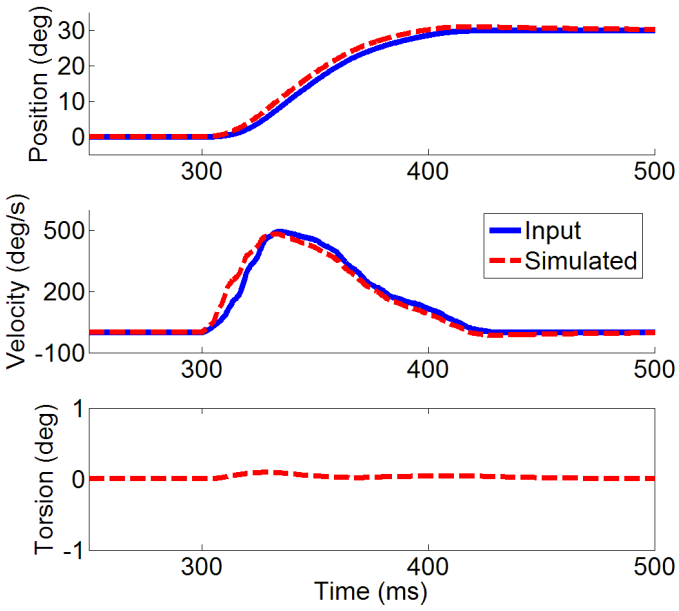

(d) Simulation validation

Figure 5.13: Simulated 30 degree abduction saccade in 20 degree elevation.

the contractibility is diminished, a paretic EOM's generated force is inadequate in moving the eye to the target gaze. As a result, ocular misalignment occurs.

EOM Paresis is one of the causes of incomitant strabismus – the deviation angle varies as a function of eye positions, depending on which muscles are impaired. Biomechanical simulation of these pathological cases is useful for quantitatively and systematically understanding the mechanical effects of paretic EOMs. Surgical procedures on paretic muscles typically involve recession, resection, or Botox injection to the antagonist muscle [von Noorden and Campos, 2001]. We simulate surgical manipulation on EOMs to correct the deviation and aim to provide insights for operational treatment.

We look at the case in which the superior oblique (SO) muscle action is weakened due to paralysis of the Fourth cranial nerve (trochlear nerve). In order to simulate superior oblique palsy (SOP), we first compute the muscle innervations that stabilize a normal eye in various eye positions. Figure 5.14 shows the innervations for fixating at nine eye positions within the range ± 20 degrees. The nine eye positions are simulated sequentially. To mimic a completely paralyzed SO, we set the SO innervation to zero. Then we apply the updated EOM innervations to move the eye and record new fixation locations that are the predicted eye positions of a pathological eye with SOP. The SOP simulation is shown in Figure 5.14.

We compare simulation results with published empirical data from a monkey with acute SOP [Shan et al., 2007a; Quaia et al., 2008]. In their experiment, the intracranial trochlear nerve that innervates SO was severed and the postoperational changes in ocular alignment were investigated. We choose this data for comparison because that the nicely controlled experimental procedure rules out other abnormalities contributing to the deviation.

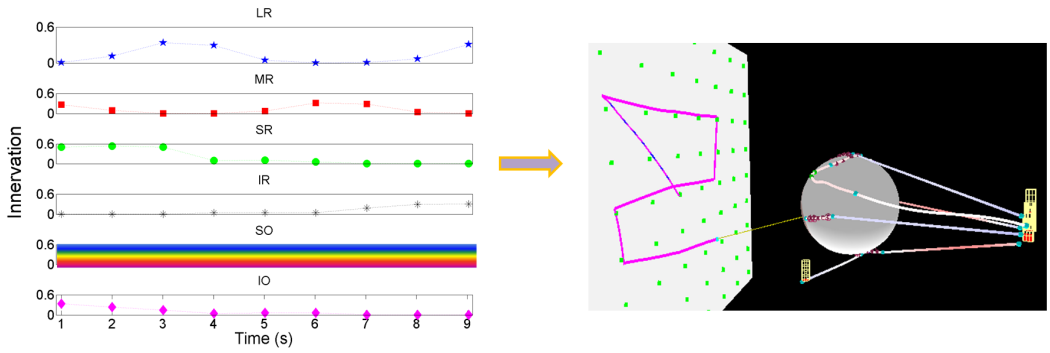

Figure 5.14: Simulation of superior oblique palsy. Computed innervations of the six EOMs to stabilize the eye in nine eye positions are shown on the left. The SO innervation is set to zero, which models the zero contractility of a paralyzed SO muscle. The biomechanical model is driven by the computed innervations with zero SO innervation to predict new eye positions of a pathological eye with SOP.

Our goal is to evaluate whether our model is able to predict deviation patterns that are qualitatively consistent with observed pathology. Quantitative assessment is difficult because the degree of deviation due to SOP varies much due to anatomical variations [Quaia et al., 2008].

The predicted eye positions of a SOP eye are plotted in Figure 5.15. Monkey alignment data, reproduced from [Quaia et al., 2008], is also presented for comparison.

Incomitant deviation, which is dependent on eye position, is observed. Our simulation shows a vertical deviation for every fixation; the deviation is greatest with the eye adducted and down. Extorsional deviation is also observed, presented as the angle between the vertical bar of the cross and the vertical axis. We conclude that simulated SOP alignment shows static deviation patterns consistent with experimental acute SOP data in [Quaia et al., 2008].

We also study the dynamic characteristics of SOP and compare our simulation to the monkey data reported in [Shan et al., 2007b]. Figure 5.16 shows the results of a 20 degree downward saccade in 10 degree adduction. It is the same

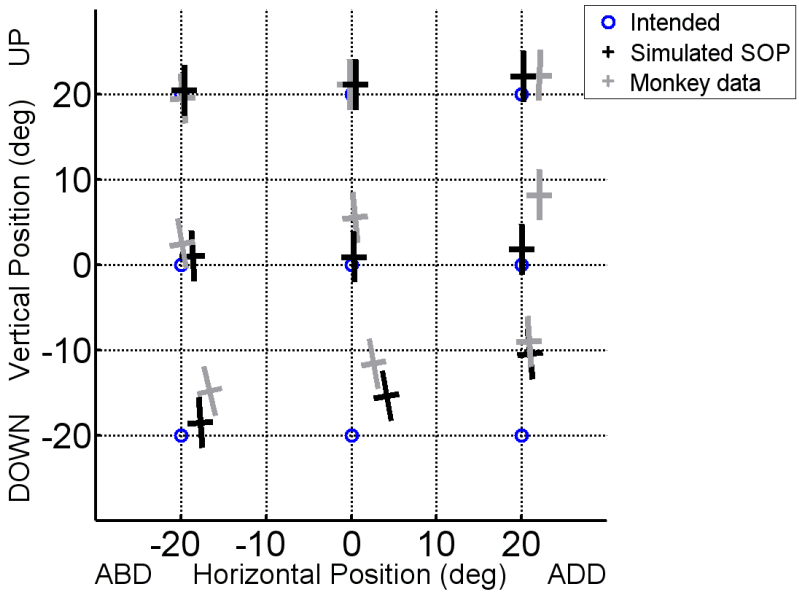

Figure 5.15: Simulated eye positions of a SOP eye shown as black crosses. Grey crosses are monkey data, reproduced from [Quaia et al., 2008]. Cyclorotation, multiplied by 1.5 for better visualization, is shown as the vertical tilt of the crosses. Courtesy of Christian Quaia for the monkey data.

saccadic movement from which the monkey data was recorded [Shan et al., 2007b]. The simulation procedure is similar to the static SOP simulation. Computed IR and SO innervations in Figure 5.16b clearly have the pulse-slide-step characteristics of saccadic neural control. Innervations of the two antagonists, SR and IO, are completely ceased during the execution of saccade, which is physiologically realistic. The vertical and torsional deviation patterns in Figure 5.16e and Figure 5.16f show qualitative agreement with the reported acute SOP dynamic data (see Figure 1. in [Shan et al., 2007b]). Our SOP simulation shows that the saccade vertical amplitude becomes smaller by about 5 degrees. Static torsion towards extorsion (positive) is observed, which is up to 3 degrees.

We also simulate a 20 degree downward saccade in 10 degree abduction. The simulation results in Figure 5.17 are qualitatively consistent with the empirical data from the same saccadic movement (see Figure 1. in [Shan et al.,

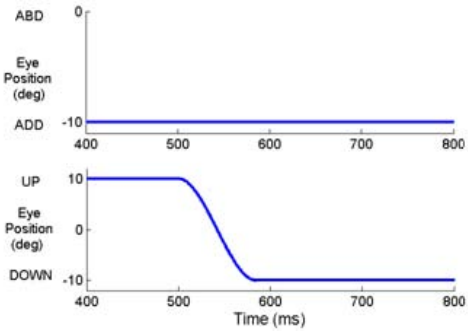

(a) Horizontal and vertical saccade trajectory

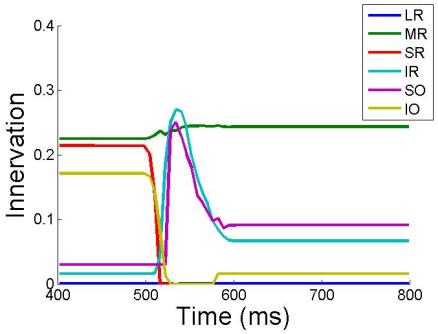

(b) Estimated EOM innervations

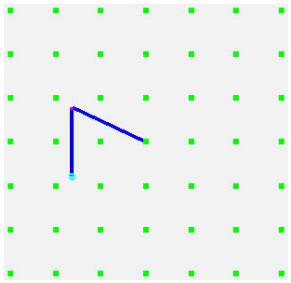

(c) Normal downward saccade in adduction

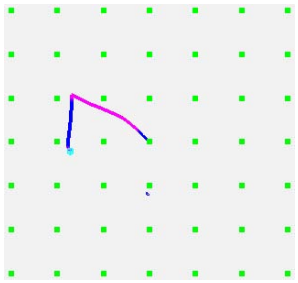

(d) Downward saccade in adduction with SOP

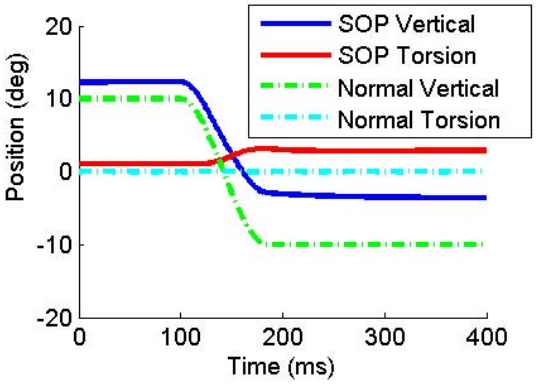

(e) Temporal vertical and torsional positions

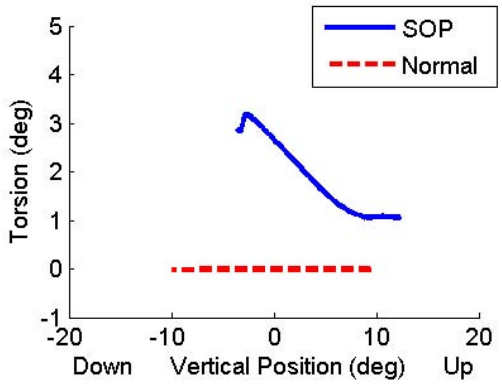

(f) Torsion as a function of eye position

Figure 5.16: Simulated SOP vertical and torsional deviation in a 20 degree downward saccade in 10 degree adduction.

2007b]). The decrease of vertical saccade amplitude is about 3 degrees, smaller than the adduction movement. Static torsion towards extorsion up to 5 degrees is observed.

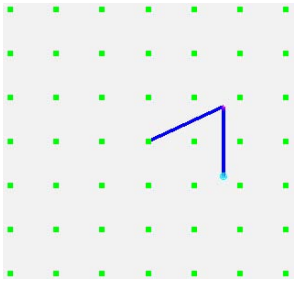

(a) Normal downward saccade in abduction

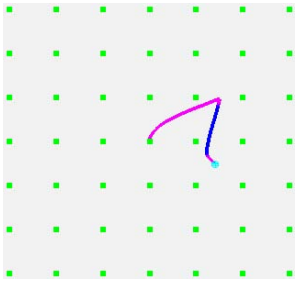

(b) Downward saccade with SOP in abduction

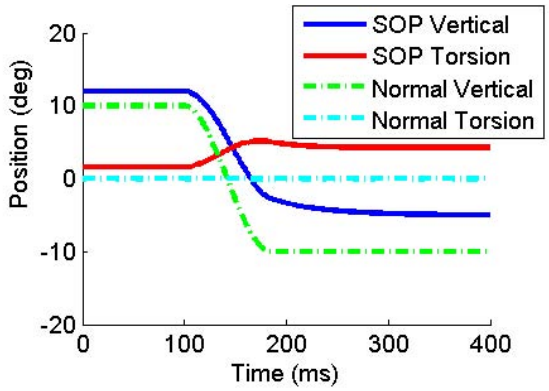

(c) Temporal vertical and torsional positions

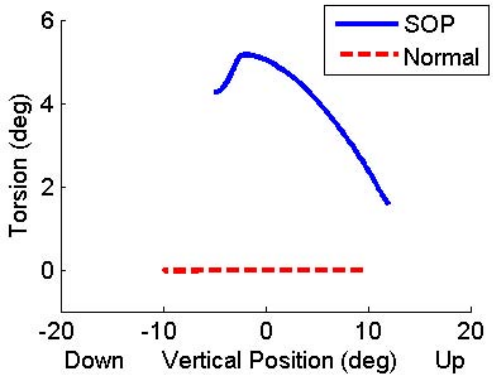

(d) Torsion as a function of eye position

Figure 5.17: Simulated SOP vertical and torsional deviation in a 20 degree downward saccade in 10 degree abduction.

There are several surgical operations for treating strabismus due to SOP. We show an example of simulating surgical correction on SOP. We model the procedures of tucking SO muscle by $5mm$ and recessing IR muscle by $3.5mm$. The former strengthens SO and the latter weakens IR for a more balanced configuration. The primary goal is to reduce or ideally eliminate the vertical deviation in the primary eye position. Operations on other EOMs might also be performed to treat associated horizontal and torsional deviations. As Figure 5.18 shows, after the EOM manipulations, the vertical deviation at primary gaze as

well as secondary horizontal gazes is corrected.

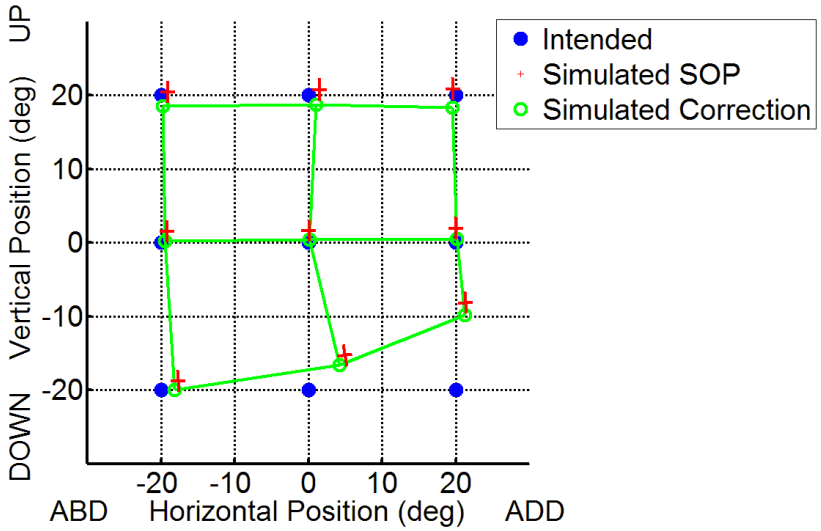

Figure 5.18: Simulated surgical correction on SOP. Vertical deviation in the primary gaze and other horizontal gazes is reduced.

5.5 Physiological Pulley Model

Different from the idealized pulley model in Section 5.4, the second model explicitly represents the mechanical linkages of the rectus muscle pulleys and the inter-muscular couplings based on histological and MRI findings. Gaze-related transverse shifts of rectus muscle pulleys, observed from MRI of human subjects under normal physiological conditions [Clark et al., 1997], are included. The second model is a realistic implementation of the orbital connective tissue architectures and the Active Pulley Hypothesis (APH) [Demer et al., 2000; Kono et al., 2002a; Demer, 2002]. Since a lot of physiological evidences are incorporated, the model is called the *physiological pulley model*. It is suitable for understanding the APH and facilitating the surgical treatment of strabismus caused by pulley pathologies.

In Section 5.5.1, we first review the active pulley hypothesis that is the foundation of the model. Then we present the details of pulley implementation in Section 5.5.2 and EOM innervation solver and Section 5.5.3. Finally we describe simulation results on system validation and strabismus in Section 5.5.4.

5.5.1 Active Pulley Hypothesis

Histological examinations on the orbital connective tissue architectures and the fiber layers of rectus muscles have been conducted [Demer et al., 2000; Kono et al., 2002a; Demer, 2002; Lim et al., 2007]. Demer et al. [1995] demonstrate a diagrammatic representation of the orbital connective tissues on a coronal plane posterior to the globe equator, shown in Figure 5.19a. This complex fibromuscular structure consists of dense collagen, elastin, and smooth muscles [Demer et al., 1995]. Based on these histological evidences and extensive MRI studies, Demer et al. [2000] propose the Active Pulley Hypothesis (APH). A schematic representation of the structures in APH from [Demer, 2002] is shown in Figure 5.19b.

In the following, we briefly introduce the APH; details of APH can be found in [Demer et al., 2000; Demer, 2002; Miller, 2007; Demer, 2007]. Rectus muscle pulleys are rings of collagenous tissues that encircle the EOMs posterior to the globe equator (see Figure 5.19b). Each rectus muscle has a global layer (GL) and an orbital layer (OL). The GL passes through the pulley ring. Anteriorly GL becomes tendinous and inserts on the sclera. The OL inserts on the pulley connective tissues and moves the pulley anteroposteriorly in coordination with the EOM insertion. The vertical positions of the pulleys are stabilized through suspensory connective tissues and intermuscular couplings shown in Figure 5.19a. Rectus pulleys act as the functional origins of the rectus muscles;

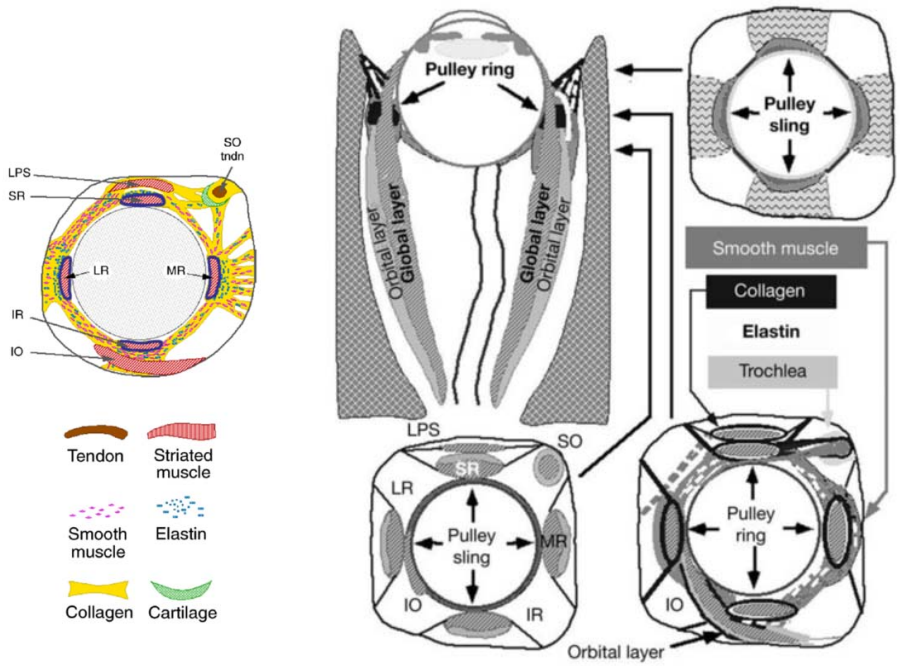

(a) Coronal view of connective tissues

(b) Connective tissues and EOM fiber layers

Figure 5.19: Schematic representation of orbital connective tissues and rectus muscle layers in the active pulley hypothesis. (a) is from [Demer et al., 1995] and (b) is from [Demer, 2002] with permission. Courtesy of Dr. Joseph Demer.

they make the rotational axis of the eye no longer fixed in the orbit but dependent on the gaze. With coordinated pulleys, the kinematics of the oculomotor plant implements Listing's law in head-fixed eye movement [Demer, 2007].

Although the functions of pulleys are still controversial, there is no doubt that the discovery of pulley connective tissues has significant implications on understanding the underlying mechanism of eye movement and associated disorders. While extensive experiments in anatomy, neurophysiology, histology, and MRI are being carried out, it has also been realized that a biomechanical model is essential in describing pulleys' kinematic functions.

The development of the two models presented in this chapter aims to provide such a computational framework. The question that we want to answer

from this study is whether the APH is mechanically plausible, that is, whether we can build a model of the orbital plant implementing the APH such that its behavior agrees with experimental data. If so, the model can then be used for further scientific research on ocular motility and clinical applications.

5.5.2 Model Description

Figure 5.20 shows the physiological pulley model. We use MR muscle as an example to describe how the APH is implemented; the modeling choices directly apply to the other rectus muscles.

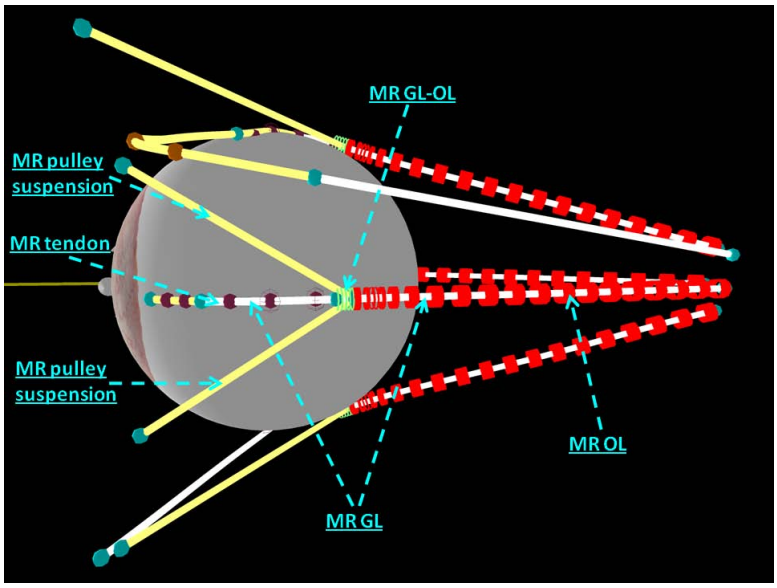

Figure 5.20: Physiological pulley model.

Similar to the idealized pulley model, each of the four rectus muscles has two contractile-elastic strands modeling the global layer (GL, shown as a white curve) and the orbital layer (OL, shown as a red string of disks). To be anatomically realistic, the lengths and cross sections of GL and OL are changed. Instead of being treated equally, now the GL strand is longer than OL in order to realistically represent the dual insertions of GL and OL [Demer, 2007]. The

lengths of the extraocular muscles and tendons in a simulated normal model are summarized in Table 5.1. They agree with the published EOM lengths [von Noorden and Campos, 2001] and the model parameters in Orbit 1.8^{TM} [Miller et al., 1995]. Because the OL contains approximately 40% of the muscle fibers, its cross section is set to 40% of the total cross section along its path before decreasing to zero near its insertional end (see Figure 5.21 for an example).

	LR	MR	SR	IR	SO	IO
Global Layer	40.7	38.2	39.5	39.9	31.1	36.7
Orbital Layer	33.2	28.6	30.8	31.1		
Tendon	6.4	3.8	5.0	5.0	31.2	-

Table 5.1: Extraocular muscle and tendon lengths (mm) of a normal model.

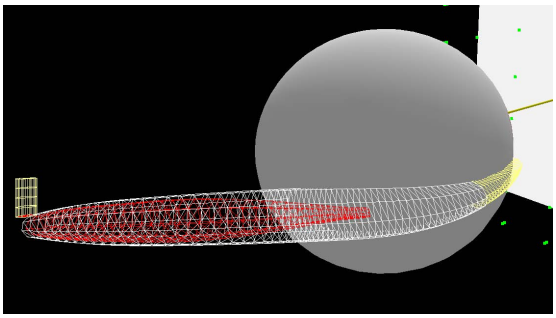

Figure 5.21: Cross sections of the GL strand (in white) and OL strand (in red) of the LR muscle. Each strand is visualized as a generalized cylinder, the radius of which is a parameter that varies along the strand path. The cross section of the OL strand is about 40% of the total cross section; the cross section of the GL strand is about 60%.

A rectus muscle also has the following noncontractile strands: a stiff elastic tendon (yellow curve anterior to GL), two elastic musculo-orbital pulley suspensions branching away from the globe (yellow segments), and an elastic intermuscular band coupling GL and OL (green dashed segment). In total, each rectus muscle has six strands.

The tendon strand has very high stiffness since EOM tendon is nearly inextensible. Two pulley suspension strands insert on the OL insertional end

and stabilize the transverse shift of the rectus muscle belly. The origins of the pulley suspension course anteriorly and attach to the orbital wall. Figure 5.22 shows the stretch-force function specified on the pulley suspension strands. The stretch-force curve is chosen based on two criteria. Firstly, the two pulley suspensions of each rectus muscle should exert sufficiently large force transversely to stabilize the rectus muscle path. Secondly, the longitudinal component of the pulley suspension force should be small compared to the rectus muscle contraction force; otherwise, the anteroposterior movement of the pulley would be restricted.

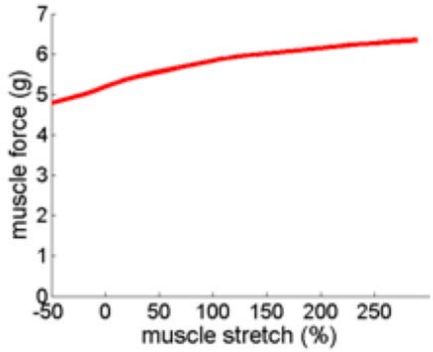

Figure 5.22: Stretch-force curve of the passive pulley suspensions.

In primary gaze, the eight pulley suspensions of the four rectus muscles are under tension, and their lengths are set to be 200% beyond their rest lengths. Enforcing tension in the primary gaze ensures that the pulley suspensions are always under positive tension even in the OFF direction movement. As a result, strand slacking never occurs.

The insertional end of OL is elastically coupled with GL through an elastic strand (shown as the short green dashed strand in Figure 5.20), called a GL-OL coupling strand. It simulates the possible laminar movement between GL and OL [Miller, 2007]. A GL-OL strand has linear elasticity (constant Young's modulus between $50kPa$ and $70kPa$) and deforms through its attachments to GL

and OL. Its length is gaze-dependent, which is affected by its stiffness, the pulley suspension stiffness, and innervations of GL and OL (will be discussed in Section 5.5.3). To avoid transverse separation of GL from OL, GL is constrained to frictionlessly slide through OL's insertional end. A prismatic joint defined on OL (not fixed in the orbit) is used to allow longitudinal movement of GL relative to OL's insertional end (pulley) and minimize their relative separation in the transverse direction.

Figure 5.23 shows simulated horizontal eye movements. The influence of the rectus pulleys on rectus muscle paths is clearly observed. As the eye rotates horizontally, the LR and MR pulleys move anteroposteriorly in coordination with the LR and MR insertions. The SR and IR pulleys remain relatively stable in the mediolateral direction to stabilize the muscle bellies as the eye rotates. In Section 5.5.4, we show that different from the idealized pulley model, SR and IR pulleys do have small transverse shifts within physiological range, which is hard to see from these figures. The SR muscle path is inflected at its pulley position and its interior path follows movement of the SR insertion. Note that lengths of the pulley suspensions change, as the pulleys move coordinately with eye positions. As the eye moves in the ON direction of an EOM, its suspension strands are elongated towards the EOM origin; as the eye moves in the OFF direction of an EOM, its suspension strands shorten.

Figure 5.24 shows simulated vertical eye movements. The transverse shift of the LR pulley (and MR pulley on the medial side hidden by the globe) is very small. LR (and MR) path is sharply inflected at its pulley location. The SR and IR pulleys move anteroposteriorly with eye rotation and lengths of the SR and IR pulley suspensions change accordingly. There is another intermuscular elastic strand modeling the coupling between LR and IO [Demer et al., 2003b],

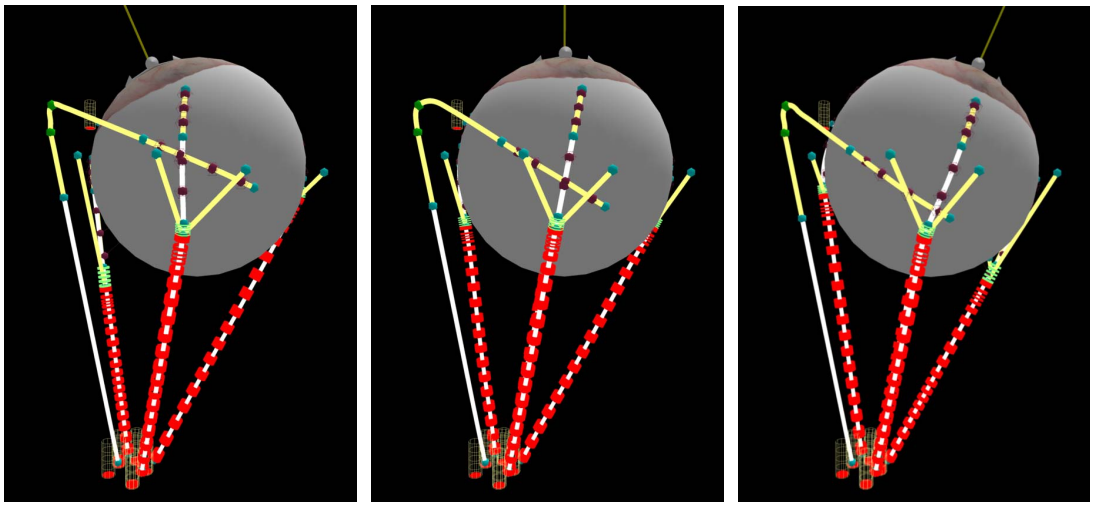

(a) Adduction gaze (b) Primary gaze (c) Abduction gaze

Figure 5.23: Simulated horizontal eye movements using the physiological pulley model. Note the SR muscle path inflection and the anteroposterior movement of the LR and MR pulleys.

visible in Figure 5.24a and Figure 5.24c. It is named the LR-IO strand and also contributes to stabilizing the LR pulley in the transverse direction.

The SO muscle is modeled as a contractile-elastic muscle strand and a very stiff tendon strand. The IO muscle is represented as a single contractile-elastic muscle strand and its short tendon is negligible. The IR-IO coupling [von Noorden and Campos, 2001; Demer et al., 2003b] is modeled as a linearly elastic strand, attached to IR and IO at their intersection in primary gaze. In a non-primary gaze, the IR-IO strand is elongated passively to constrain the relative movement between IR and IO, shown in Figure 5.25. MRI studies have shown that IO moves anteroposteriorly by about 50% of the IR insertion's travel [Demer et al., 2003b]. Young's modulus of the IR-IO strand is chosen as $750Pa$ such that the half distance relationship is implemented at good approximation.

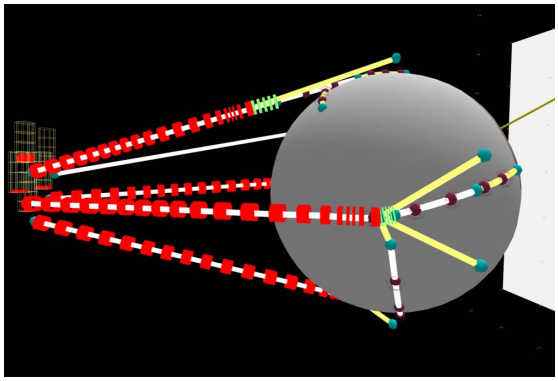

(a) Supraduction (elevation) gaze

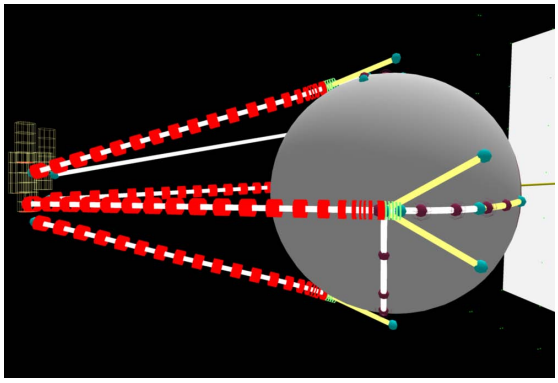

(b) Primary gaze

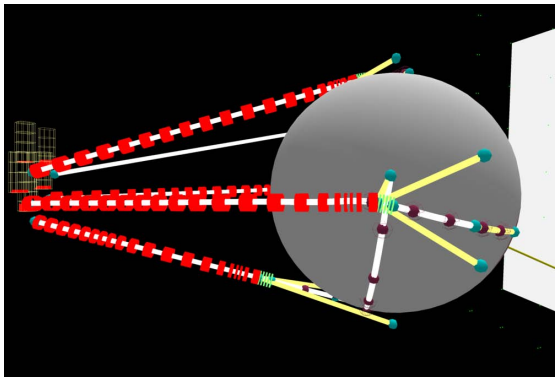

(c) Infraduction (depression) gaze

Figure 5.24: Simulated vertical eye movements using the physiological pulley model. Note the LR muscle path inflection.

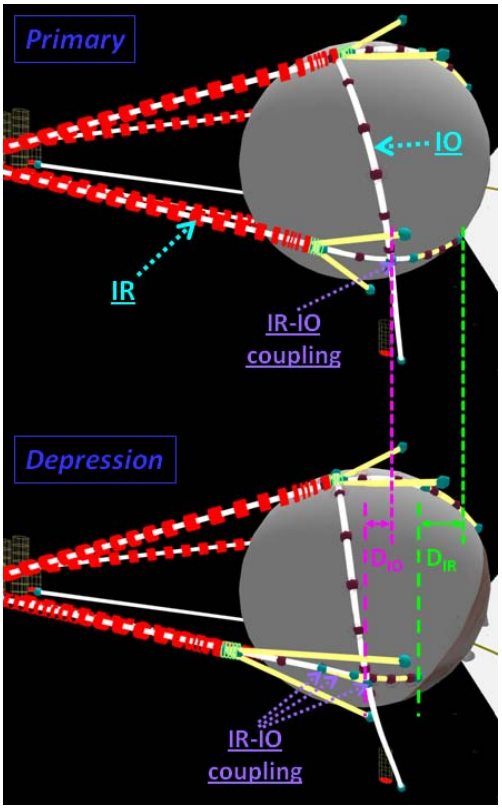

Figure 5.25: The IR-IO coupling is modeled as an elastic strand connecting IR and IO at their intersection. The strand is stretched in a depressed gaze. The IO moves nearly half as far as IR insertion travels $D_{IO} = 0.5D_{IR}$.

5.5.3 Innervation Computation

EOM innervations are computed to follow desired trajectories. Different from the previous model, now each rectus muscle has two different contractile-elastic strands that need to be solved. Modeling the possibly, slightly differential control of GL and OL [Miller, 2007], the system is even more over-constrained than the previous one. The innervation variable a is a 10×1 vector composed of innervations of the ten contractile-elastic EOM strands (two for the GL and OL of each rectus muscle plus one for SO and one for IO).

The objective function of the innervation optimization for this more complicated model has extra constraints than the objective in Equation 5.1, and is

given as follows:

$$\begin{aligned} \min_{a} \quad & w_a\|a\|^2 + w_x\|(H_x a + v_f) - v_x\|^2 \\ \text{s.t.} \quad & 1 \geq a_i > a_i^0 \; c_v(v_{eye}) \; c_p(p_{eye}) \\ & a_i^{OL} - a_i^{GL} \geq \triangle a \qquad\qquad EOM_i\text{'s ON direction} \end{aligned} \tag{5.5}$$

The additional constraint $a_i^{OL} - a_i^{GL} \geq \triangle a$ models the relationship between the innervations of GL and OL of a rectus muscle. The constraint enforces that when the eye is moving or fixating in the ON direction, the OL innervation is at least $\triangle a$ higher than the GL innervation. This constraint term is an approximation of Collins' measured GL and OL fiber activities in various fixation positions (see Figure 5 in [Collins et al., 1975]), which show a nearly constant offset.

5.5.4 Results

Computed EOM Innervations

We first simulate fixations at nine eye positions over the range $\pm 20^\circ$. Figure 5.26 shows estimated EOM innervations as a function of horizontal and vertical eye positions.

Innervations are interpolated and plotted as iso-innervation curves to illustrate innervation levels more clearly. The GL and OL strands of a rectus muscle have similar innervation patterns, with nearly constant difference. The LR and MR innervations are mainly dependent on the horizontal eye position, implying separable control of the horizontal EOMs. The result is consistent with known anatomy and neurophysiology of the horizontal EOMs [von Noorden and Campos, 2001]. Computed innervations of the vertical and oblique EOMs are more complex, due to their non-orthogonal anatomical arrangement

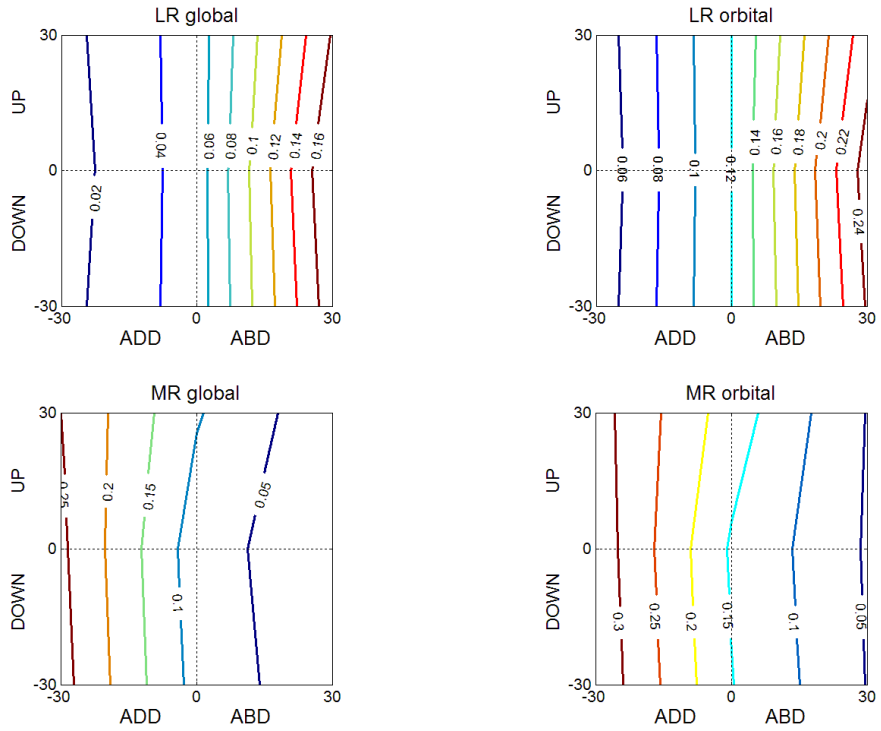

Figure 5.26: Computed EOM innervations shown as iso-innervation curves over the two-dimensional eye positions.

and coupled actions. Different from LR and MR, each of these four EOMs contributes to all three degrees of freedom of eye rotation; nevertheless, their primary and secondary action directions are different [von Noorden and Campos, 2001].

EOM Paths in Secondary Gazes

To validate the physiological pulley model, we first check the locations of the rectus pulleys in secondary gazes. Figure 5.27 shows the muscle paths in four secondary gazes ($\pm 24°$), plotted in the same way as the measured pulley positions from MRI [Clark et al., 2000].

One characteristics of this pulley model is that the physiological transverse

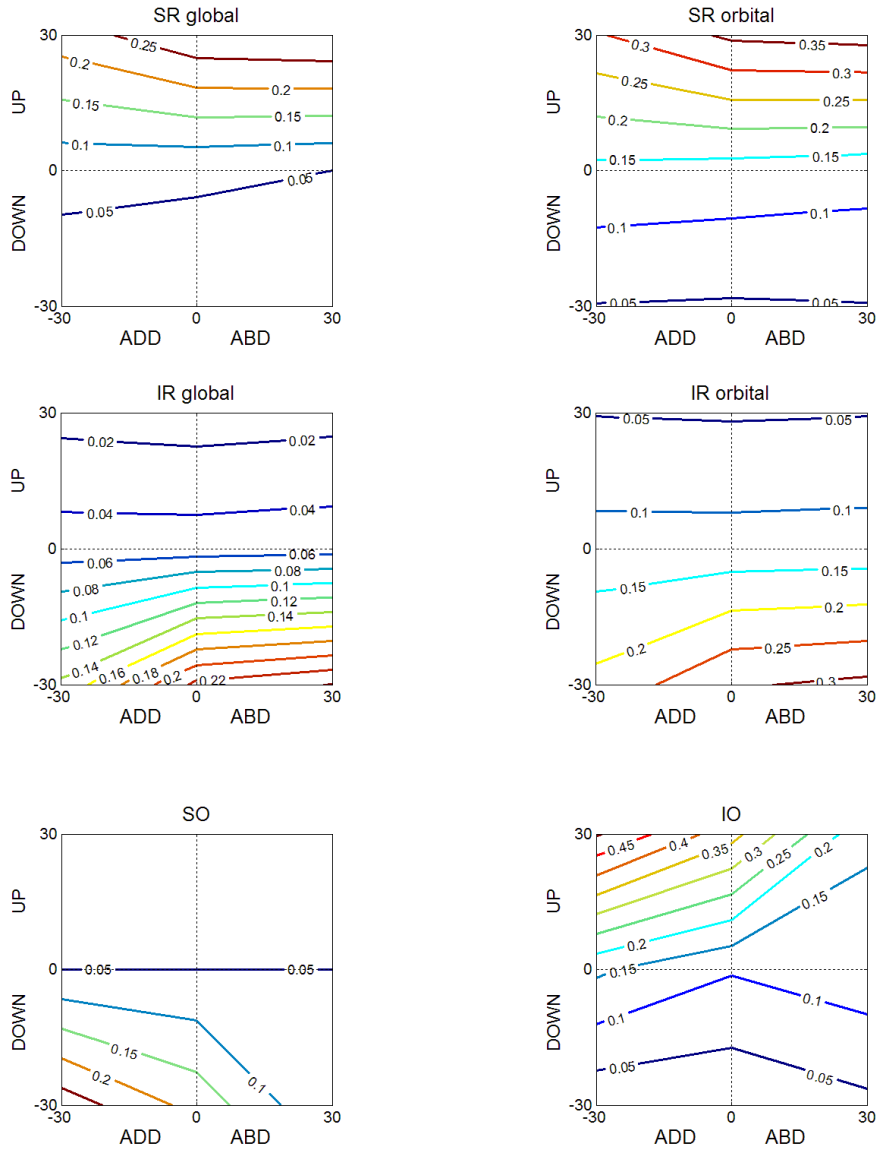

Figure 5.26: Computed EOM innervations shown as iso-innervation curves over the two-dimensional eye positions.

shifts of the rectus pulleys are allowed. The shifts are still sufficiently small such that rectus muscle bellies are stabilized. Clark et al. [2000] report approximately 0.5mm side-slip of MR in the direction of gaze. As Figure 5.27b shows, simulated MR pulley has maximal sideslip about 0.7mm, consistent with the MRI data. Clark et al. [2000] report approximately 0.5mm side-slip of LR in the

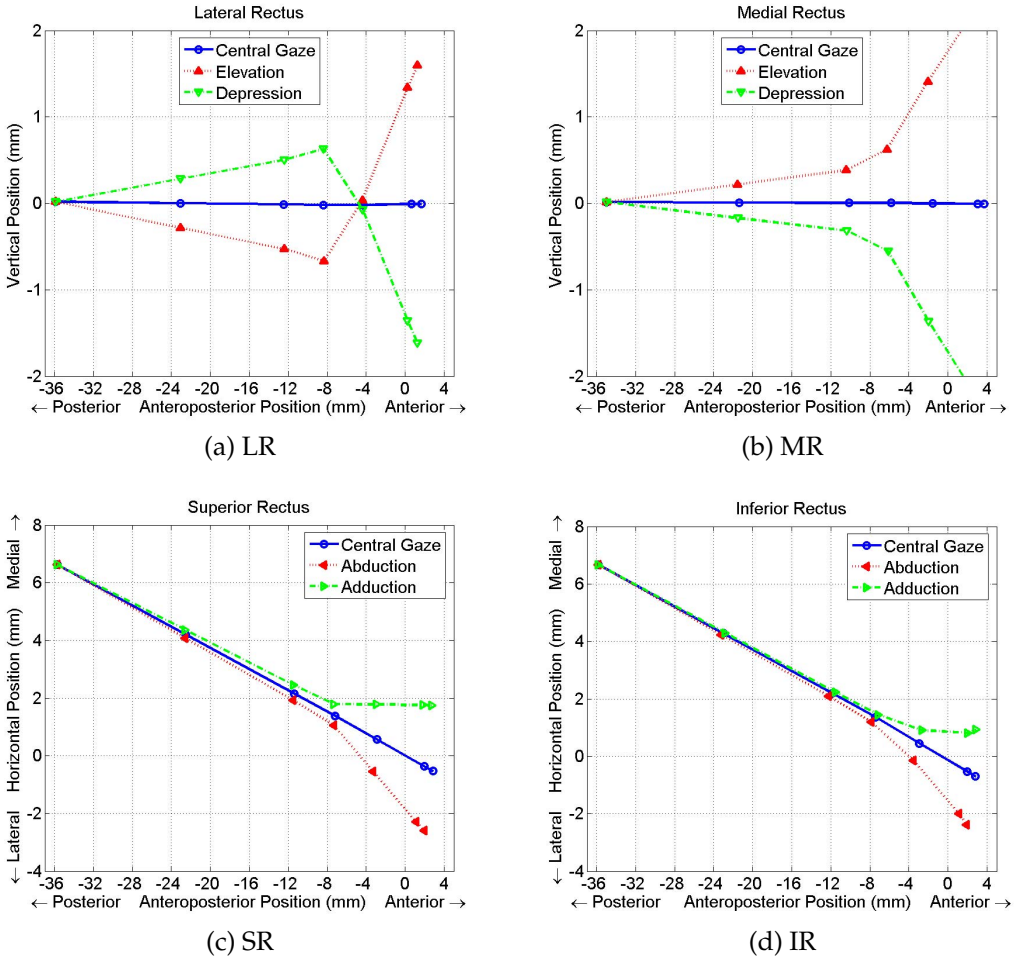

(a) LR (b) MR

(c) SR (d) IR

Figure 5.27: Rectus muscle paths in secondary gazes.

opposite direction of gaze, due to the coupling between LR and IO. Simulated LR pulley in Figure 5.27a exhibits side-slip about $0.8mm$ in the opposite direction of gaze, realistically modeling this interesting phenomenon. The LR-IO strand in our model is the key component that results in realistic LR pulley shifts. The simulated SR pulley has small side-slip in the same direction of gaze, consistent with [Clark et al., 2000]. The only discrepancy occurs on IR. The small transverse shift of simulated IR pulley is also in the gaze direction, whereas Clark et al. [2000] find IR shift in the opposite direction. We suspect that it is due to the implementation of the IR-IO coupling, which needs to be

improved. To conclude, this model produces plausible pulley movements that are in good agreement with the MRI data in [Clark et al., 2000].

Pulley Locations in Tertiary Gazes

We record rectus pulley positions in tertiary gazes to validate the model's implementation of the active pulley hypothesis. Nine eye positions $\pm 24^{\circ}$ are simulated and analyzed using the analysis approach in [Kono et al., 2002a]. Simulation results are presented in Figure 5.28.

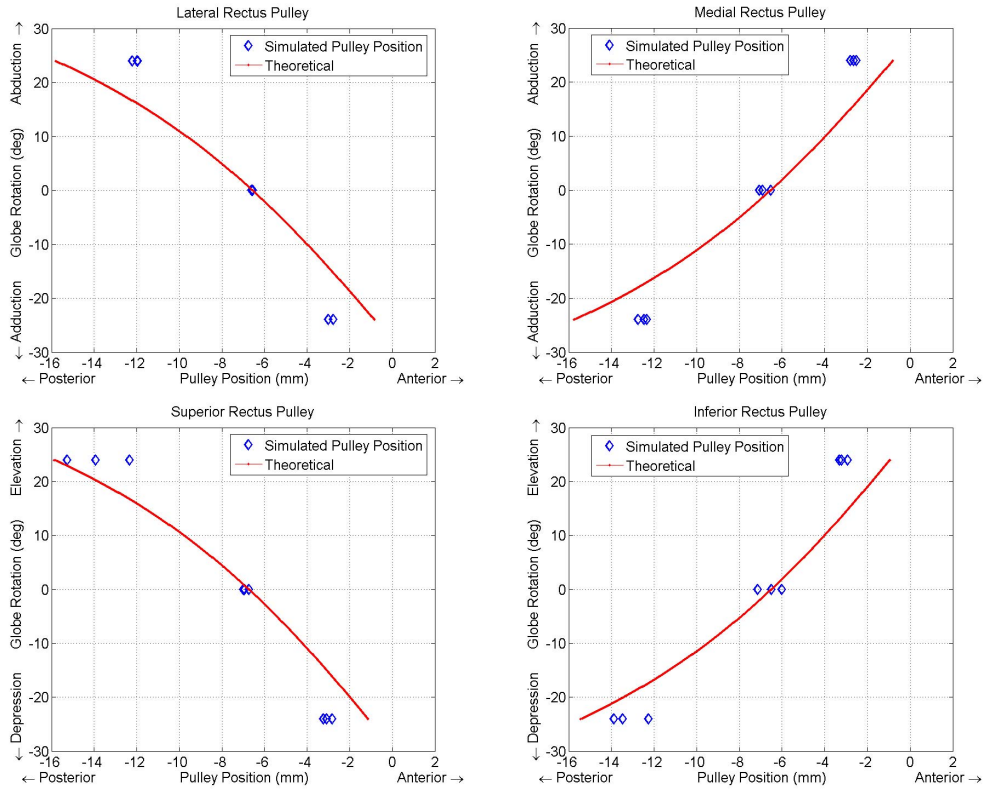

Figure 5.28: Relationship of the anteroposterior positions of the rectus pulleys to eye positions. Abscissa zero is referenced to the globe center.

The theoretical pulley positions are estimated from the EOM insertions. As the APH describes, ideally, the distance from an EOM insertion to the globe center and the distance from its pulley to the globe center are equal at any eye

position. Our simulated pulley anteroposterior positions show desired gaze-dependent characteristics and reasonably approximate the theoretical pulley locations.

Simulation of Superior Oblique Palsy

We simulate the ocular misalignment due to palsy of the superior oblique muscle (SOP). The simulation procedure is the same as the first model (see Section 5.4.1). The result is shown in Figure 5.29.

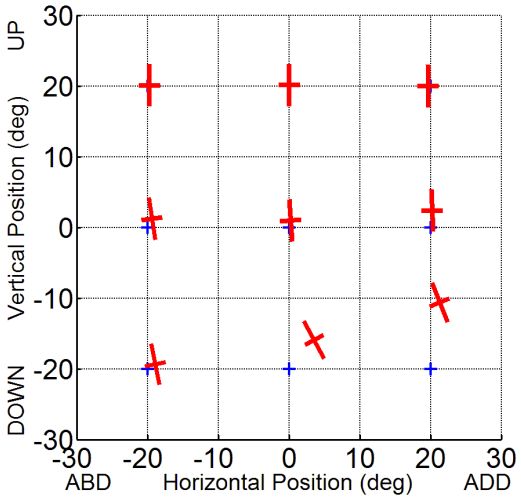

Figure 5.29: Simulated eye positions of an eye with SOP, shown as the red crosses. Cyclorotation, multiplied by 3 for better visualization, is shown as the tilt of the crosses.

Similar to the previous simulation, we observe vertical deviation that is greatest with the eye adducted and down. The simulation also shows gaze dependent torsional deviation as well as horizontal deviation that are the greatest in depression. We demonstrate that the physiological pulley model is also able to predict the deviation patterns caused by SOP.

Simulation of LR Sagging

Clinical studies have shown that the degeneration of the elastic band coupling SR muscle and LR muscle due to aging could lead to strabismus [Rutar and Demer, 2009]. Due to the decreased elasticity of the SR-LR band, in these patients, LR normally has an vertical displacement inferior to the vertical center of the globe. As a mechanical consequence, the effective force of LR muscle is diverted from lateral to inferior and cyclotorsion. Therefore, LR muscle is less effective as an actuator in the abduction direction. Esotropia and hypotropia are typically observed from these elderly patients. SR muscle might also exhibit deviation in the temporal direction, but is mechanically negligible.

To better understand the mechanical effects of LR sagging, we simulate this pathology using our model. The SR-LR band is modeled as a noncontractile elastic strand, coupling SR and LR and sliding on the globe surface. The stiffnesses of the LR pulley suspensions and the LR-SR band are adjusted to model the LR-SR degeneration. The LR rest length is increased by 10%. As a result, LR muscle is displaced inferiorly by $5.7mm$ and SR muscle is displaced temporally by $0.7mm$ in primary gaze. Figure 5.30 shows the simulated model without and with sagged LR. Note how the LR muscle is displaced inferiorly.

We first estimate the EOM innervations using the normal model in Figure 5.30a. We then simulate the model with sagged LR using the computed innervations and show the results in Figure 5.31. Esotropia and hypotropia are observed, consistent with clinical findings [Rutar and Demer, 2009]. Esotropia is the largest in depression and abduction. Hyoptropia is larger in elevation.

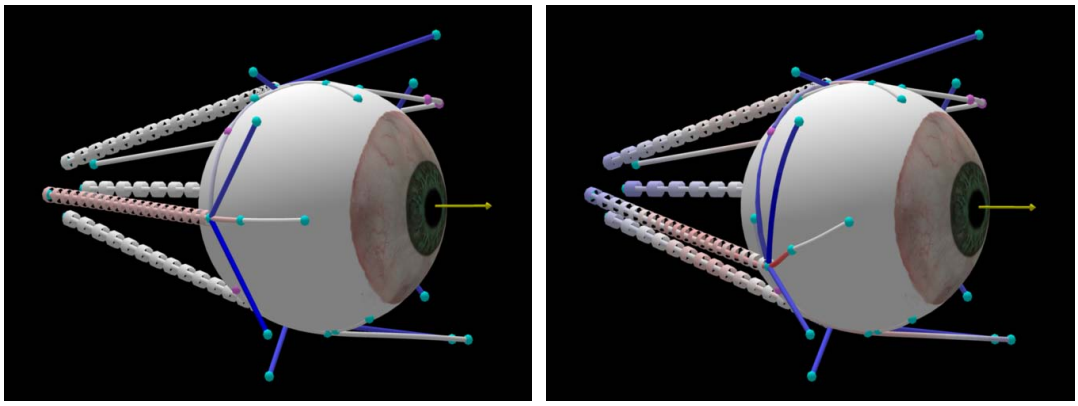

(a) Normal (b) LR sagging

Figure 5.30: Comparison of the model (a) without and (b) without LR sagging.

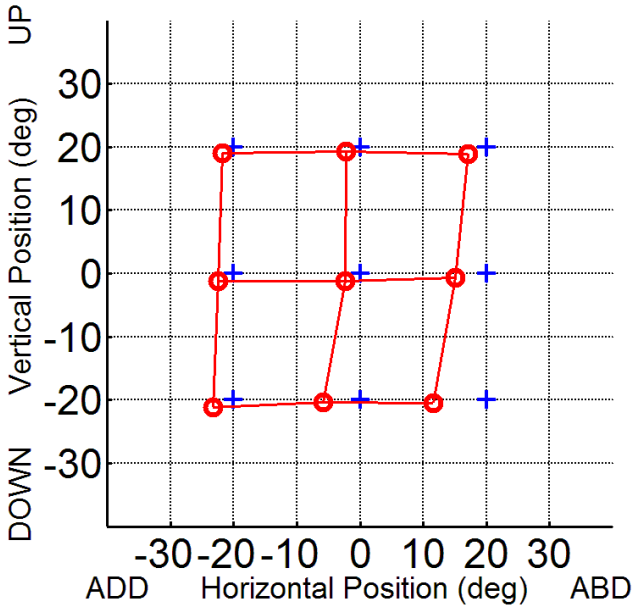

Figure 5.31: Simulation of ocular misalignment due to LR sagging.

5.6 Conclusions

We present a 3D biomechanical simulation framework for studying the mechanics and neural control of human eye movement and facilitating surgical treatment. Limitations of previous models are addressed. Our biomechanical model of the oculomotor plant takes into account the nonlinear EOM geometry and can include individualized anatomical data. We model EOMs as

strands, which are musculotendinous modeling primitives. Complicated EOM constitutive models derived from empirical data are incorporated in the plant mechanics. Various kinds of eye movements, including fixations, smooth pursuits, and saccades can be simulated. We develop two models that provide different implementation of the rectus pulleys.

The first model, called the *idealized pulley model*, represents the rectus muscle pulleys as prismatic joints. Anteroposterior movements of pulleys are allowed and transverse pulley shifts are strictly restricted. Due to its simplicity, fewer undetermined parameters are introduced into the model, which makes it suitable for studying the dynamics and neural control of ocular motility. Simulation results show nonhomogeneous EOM deformation during smooth pursuit movement, consistent with motion encoded MRI data. Given EOM innervations, the model generates realistic saccadic trajectories. Strabismus deviation patterns caused by superior oblique palsy can also be predicted.

The second model, called the *physiological pulley model*, explicitly represents the mechanical linkages of the rectus muscle pulleys and the inter-muscular couplings based on the Active Pulley Hypothesis. Known physiological evidence of the orbital connective tissues are incorporated in the model. Gaze-related transverse shifts of rectus muscle pulleys are modeled. From simulations and validations, we show that the active pulley hypothesis is mechanically plausible using strands to represent EOMs and pulleys. The model has important clinical application in simulating strabismus caused by pulley pathologies.

Chapter 6
Conclusion

This dissertation presented several studies on biomechanical modeling and simulation of human eye movement. Our objective is to lay the foundation of a biomechanical and computational framework that possesses fewer assumptions than previous models and is sufficiently general for both scientific research and clinical applications. To achieve this goal, we developed several methodologies and validate simulation results against experimental data.

Plausible biomechanical simulation requires models with realistic anatomical properties. Building subject-specific 3D models of the orbit from medical imaging data is especially important for potential clinical simulation of surgical outcomes, which needs to incorporate patient-specific characteristics and pathologies. We presented an efficient and robust method on reconstructing 3D geometric models of the orbit from magnetic resonance images acquired from human subjects. A template model is used as the prior and is deformed to fit individual data. The template resolves the uncertainty in the boundary between EOM and tendon due to limited image contrast, and leads to a complete model. Our method is suitable for reconstructing geometric models with minimum manual work for many subjects and at different eye positions. We also applied the template fitting approach to build detailed 3D meshes of the eyeball from MRI, which can potentially be used in simulation and analysis of clinical myopia.

Measuring EOM deformation *in vivo* is useful for understanding EOM biomechanics but is also challenging. Motivated by the difficulty of inferring deformation properties directly from conventional images, we proposed a longitudinal strain estimation approach. Our method is sufficiently general for studying the mechanical properties of fusiform muscles (for instance, extraocular muscles) and tendons *in vivo*. The fiber bundles in these tissues are arranged in parallel and the functionally most important deformation is along the longitudinal axis. We took advantage of the incompressibility of soft tissues to find correspondences between discrete tissue segments in different deformation states. Our approach uses geometric models as input, and is independent of image intensity-based correspondences that are harder to get. We validated the accuracy of the method through MRI phantoms and computer simulation. We also computed EOM deformation at various horizontal gazes by using reconstructed EOM models. We observed inhomogeneous muscle deformation as a function of eye positions. The method is very efficient to compute and enables estimation of soft tissue deformation when advanced imaging facilities are unavailable.

Utilizing the reconstructed 3D models of the extraocular muscles and the estimated longitudinal strains, we demonstrated that EOM meshes in various eye positions can be registered and correlated. We described an algorithm to apply deformation properties in surface registration such that the resulting geometries provide direct correspondences in the material coordinates. Normally, geometric models reconstructed from different deformed states only represent the shape variations; they do not show consistent deformation and are independent of each other. We enforced physical consistency constraints in surface fitting to regulate positions of the mesh points. The method can be

generalized to create realistic models for biomechanical simulation.

To understand the mechanics and neural control of human eye movement, it is important to have a model of the oculomotor plant that incorporates its anatomical and physiological properties. We developed such a biomechanical model that satisfies the requirements for scientific research and clinical use. The extraocular muscles are represented as strands, which are musculotendinous modeling primitives. Realistic EOM paths and cross sectional areas of these EOM strands are based on geometric models reconstructed from human subject MRI, applying our proposed template fitting approach. Nonlinear constitutive properties are associated with the EOMs. Our simulator is the first biomechanical model of the orbital plant that simulates dynamic eye movements. An important contribution of our model is that we represent the mechanical functions and architectures of the pulley connective tissue. The active pulley hypothesis (APH) is realistically modeled. We showed that the mechanical linkages and intermuscular couplings hypothesized in APH are quantitatively plausible, which is a major step towards investigating pulley functions in ocular motility.

Before using the biomechanical model to answer scientific questions and for clinical simulations, we need to assess the plausibility and accuracy of the simulator. We performed several validations from different aspects, which not only evaluate the realism of our strand-based biomechanical model of the orbit, but also provide guidance for choosing model parameters. EOM deformation during smooth pursuit was examined and compared to published motion-encoded MRI data. Consistent deformation patterns were observed. We simulated saccadic eye movements that abduct at different amplitudes. Empirical

abducens motoneuron discharges were used to drive the lateral rectus muscle, the primary EOM that is active in these eye movements. We found that the simulated saccadic trajectories reasonably follow the desired trajectories, which shows the realism of the plant mechanics. We also simulated strabismus caused by superior oblique muscle palsy. The predicted deviations in various directions were qualitatively consistent with experimental data from controlled subjects. Finally, EOM paths at different gazes were quantitatively analyzed to ensure the transverse stability of pulleys. Based on the results, we conclude that our simulator with nonlinear orbital mechanics and MRI-based anatomical properties is able to generate realistic static and dynamic eye movements and can be applied in further scientific and clinical studies.

6.1 Future Work

In future studies, we would like to extend our current work in the following directions.

6.1.1 Functional Reconstruction

We plan to visualize orbital connective tissues from histological images [Miller et al., 2003; Kono et al., 2002b; Demer, 2008] and build a complete biomechanical model of the orbit including these structures. To understand the two-layer structures of extraocular muscles and the connective tissue pulleys, high resolution digital light micrographs were taken from histologically stained extraocular muscles and representative fascicles were traced manually from those images [Lim et al., 2007]. It would be useful to develop an automated approach

to track a majority of the EOM fibers to learn their architectures. With an efficient tracing program, we can also study the physiological change of EOMs associated with certain pathology, such as acute superior oblique palsy.

6.1.2 Statistical Eyeball Shape Analysis

We will perform a statistical analysis of eyeball shape on a larger population of normal subjects, by using either principal component analysis (PCA) or spherical harmonics to describe the shape variations. It is clinically useful to investigate the relationship of eye shape to refractive error and to strabismus. Another important topic is to quantify eyeball deformation as a function of eye position; it has not been analyzed previously. All of these studies will provide information about impact of globe shape on ocular motility.

6.1.3 General Strain Estimation

We plan to study strain estimation from more general deformation with shearing and non-homogeneous tissue properties. If few sparse correspondences are available, we will exploit the incompressibility constraint to deal with structures that are more complex. We would also like to apply physically registered models in finite element models and strand simulations to analyze other properties of the extraocular muscles.

6.1.4 Ocular Biomechanics

One of the motivations of developing a realistic computational model is the need of such a model to understand the complex behaviors of the oculomotor plant. One central question under debate is how Listing's law is implemented. By using computational models, it has been shown mathematically that properly placed pulleys simplify the neural control of saccades – a commutative saccadic generator can produce realistic saccades obeying Listing's law [Raphan, 1998; Quaia and Optican, 1998]. However, these models made linearity assumptions on the orbital plant. In order to accurately study the kinematic functions of the extraocular muscle pulleys, nonlinearity of the ocular mechanics needs to be incorporated. Our biomechanical model provides anatomical and physiological realism and has been validated against experimental data. We would like to drive the model by the proposed controllers, and test the plausibility of the pulley hypothesis.

6.1.5 Quantitative Clinical Simulation

Our biomechanical model is suitable for simulating strabismus and its surgical outcomes. The model is customizable for individual patients for subject-specific prediction. It is easy to incorporate anatomical properties (such as EOM paths and cross sections) and orbital pathologies (such as pulley heterotopy). Proper parameters can be estimated such that the predicted behavior of the individual plant model matches the clinical measurement of the subject, for instance the alignment chart. Then surgical treatment can be simulated and planned. We would like to conduct quantitative clinical simulation along this line by first validating the model against post-operative data.

Bibliography

AAPOS. `http://www.aapos.org`. 1

B. Allen, B. Curless, and Z. Popović. The space of human body shapes: Reconstruction and parameterization from range scans. *ACM Transactions on Graphics (SIGGRAPH 2003)*, pages 587–594, 2003. 80

N. Amenta, M. Bern, and M. Kamvysselis. A new voronoi-based surface reconstruction algorithm. *ACM SIGGRAPH 1998*, 1998:415–421, 32. 20

D. S. Asakawa, G. P. Pappas, S. S. Blemker, J. E. Drace, and S. L. Delp. Cine phase-contrast magnetic resonance imaging as a tool for quantification of skeletal muscle motion. *Seminars in Musculoskeletal Radiology*, 7(4):287–295, 2003. 58

D. A. Atchison, N. Pritchard, K. L. Schmid, D. H. Scott, C. E. Jones, and J. M. Pope. Shape of the retinal surface in emmetropia and myopia. *Investigative Ophthalmology and Visual Science*, 46:2698–2707, 2005. 18, 49

C. Baur and S. P. Fekete. *Approximation of Geometric Dispersion Problems*, chapter 63-75. Springer-Verlag, 1998. 45

S. F. Bensamoun, S. I. Ringleb, Q. Chen, R. L. Ehman, K. N. An, and M. Brennan. Thigh muscle stiffness assessed with magnetic resonance elastography in hyperthyroid patients before and after medical treatment. *Journal of Magnetic Resonance Imaging*, 26(3):708–713, 2007. 57

S. S. Blemker and S. L. Delp. Three-dimensional representation of complex muscle architectures and geometries. *Annals of Biomedical Engineering*, 33(5):661–673, 2005. 41, 77, 80

J. Canny. A computational approach to edge detection. *IEEE Trans. Pattern Analysis and Machine Intelligence*, 8:679–714, 1986. 25

M. Chen, T. Kanade, and D. Pomerleau. Bootstrap a statistical brain atlas. *Fifth IEEE Workshop on Applications of Computer Vision*, pages 114–119, 2000. 21

M. R. Clark and L. Stark. Control of human eye movements: I. modelling of extraocular muscles; II. a model for the extraocular plant mechanism; III. dynamic characteristics of the eye tracking mechanism. *Math. Biosci.*, 20:191–265, 1974. 95, 96

R. A. Clark and J. L. Demer. Effect of aging on human rectus extraocular muscle paths demonstrated by magnetic resonance imaging. *American Journal of Ophthalmology*, 134(6):872–878, 2002. 4

R. A. Clark and J. L. Demer. Magnetic resonance imaging of the effects of horizontal rectus extraocular muscle surgery on pulley and globe positions and stability. *Investigative Ophthalmology & Visual Science*, 47:188–194, 2006. 4, 37

R. A. Clark, J. M. Miller, and J. L. Demer. Location and stability of rectus muscle pulleys. *Investigative Ophthalmology and Visual Science*, 38:227–240, 1997. 17, 124

R. A. Clark, J. M. Miller, and J. L. Demer. Three-dimensional location of human rectus pulleys by path inflections in secondary gaze positions. *Investigative Ophthalmology & Visual Science*, 41:3787–3797, 2000. 4, 13, 33, 55, 78, 91, 101, 107, 135, 136, 137, 138

R. A. Clark, J. M. Miller, A. L. Rosenbaum, and J. L. Demer. Heterotopic muscle pulleys or oblique muscle dysfunction? *Journal of American Association for Pediatric Ophthalmology and Strabismus*, 2(1):17–25, February 1998. 17

E. Cohen, R. F. Riesenfeld, and G. Elber. *Geometric Modeling With Splines: An Introduction*. A. K. Peters, Ltd., Natick, MA, USA, 2001. ISBN 1-56881-137-3. 24

L. D. Cohen and I. Cohen. Finite-element methods for active contour models and balloons for 2-D and 3-D images. *IEEE Trans. Pattern Anal. Mach. Intell.*, 15(11):1131–1147, 1993. 34

C. C. Collins. *The control of eye movements*, chapter Orbital mechanics, pages 283–325. Academic Press, New York, 1971. 95

C. C. Collins, D. O'Meara, and A. B. Scott. Muscle tension during unrestrained human eye movements. *Journal of Physiology*, 245(2):351–369, February 1975. 96, 106, 134

G. Cook and L. Stark. Deviation of a model for the human eye-positioning mechanisms. *Bull. Math. Biophys.*, 29(153), 1967. 96

L. E. DeFrate, A. van der Ven, P. J. Boyer, T. J. Gill, and G. Li. The measurement of the variation in the surface strains of Achilles tendon grafts using imaging techniques. *Journal of Biomechanics*, 39:399–405, 2006. 57, 58, 59

J. L. Demer. The orbital pulley system: A revolution in concepts of orbital anatomy. *Annals of the New York Academy of Sciences*, 956(1):17–32, 2002. 124, 125, 126

J. L. Demer. Pivotal role of orbital connective tissues in binocular alignment and strabismus the friedenwald lecture. *Investigative Ophthalmology and Visual Science*, 45:729–738, 2004. 1, 7, 91, 101

J. L. Demer. *Neuro-Ophthalmology: Neuronal Control of Eye Movement, Developments in Ophthalmology*, volume 40, chapter Mechanics of the Orbita, page 132157. Karger, 2007. 1, 2, 10, 13, 37, 91, 125, 126, 127

J. L. Demer. *Clinical Ophthalmology*, volume 1, chapter Extraocular muscles. Phila-delphia: Lippincott Williams and Wilkins, 2 edition, 2008. 146

J. L. Demer, R. Kono, and W. Wright. Magnetic resonance imaging of human extraocular muscles in convergence. *Journal of Neurophysiology*, 89:2072–2085, 2003a. 4

J. L. Demer and J. M. Miller. Magnetic resonance imaging of the functional anatomy of the superior oblique muscle. *Investigative Ophthalmology and Visual Science*, 36:906–913, 1995. 17

J. L. Demer, J. M. Miller, E. Y. Koo, and A. L. Rosenbaum. Quantitative magnetic resonance morphometry of extraocular muscles: A new diagnostic tool in paralytic strabismus. *Journal of Pediatric Ophthalmology and Strabismus*, 31:177188, 1994. 4, 17

J. L. Demer, J. M. Miller, V. Poukens, H. V. Vinters, and B. J. Glasgow. Evidence for fibromuscular pulleys of the recti extraocular muscles. *Investigative Ophthalmology & Visual Science*, 36:1125–1136, 1995. 13, 125, 126

J. L. Demer, S. Y. Oh, R. A. Clark, and V. Poukens. Evidence for a pulley of the inferior oblique muscle. *Investigative Ophthalmology & Visual Science*, 44:3856–3865, 2003b. 4, 130, 131

J. L. Demer, S. Y. Oh, and V. Poukens. Evidence for active control of rectus extraocular muscle pulleys. *Invest Ophthalmol Vis Sci*, 41:1280–1290, 2000. 13, 101, 124, 125

M. A. Dresner, G. H. Rose, P. J. Rossman, R. Muthupillai, A. Manduca, and R. L. Ehman. Magnetic resonance elastography of skeletal muscle. *Journal Of Magnetic Resonance Imaging*, 13(2):269–276, 2001. 57

H. Edelsbrunner and E. P. Mucke. Three-dimensional alpha shapes. *ACM Transactions on Graphics*, 13:43–72, 1994. 20

M. Epstein, M. Wong, and W. Herzog. Should tendon and aponeurosis be considered in series? *Journal of Biomechanics*, 39(11):2020–2025, 2006. 59

J. W. Fernandez, P. Mithraratne, S. F. Thrupp, M. H. Tawhai, and P. J. Hunter. Anatomically based geometric modelling of the musculo-skeletal system and other organs. *Biomechanics and Modeling in Mechanobilogy*, 2(3):139–155, 2004. 21

N. Fiorentino, J. Lin, M. Guttman, A. Derbyshire, D. Mazilu, N. Evoy, E. McVeigh, and S.S. Blemker. Characterizing hamstrings muscle dynamics during knee flexion-extension using real-time MRI. *American Society of Biomechanics Annual Conference*, 2007. 57

A. F. Fuchs and E. S. Luschei. Firing patterns of abducens neurons of alert monkeys in relationship to horizontal eye movement. *Journal of Neurophysiology*, 33:382–392, 1970. 113

C. L. Gilchrist, J. Q. Xia, L. A. Setton, and E. W. Hsu. High-resolution determinination of soft tissue deformations using MRI and first-order texture correlation. *IEEE Transactions on Medical Imaging*, 23(5):546–553, 2004. 57

B. Gilles, L. Moccozet, and N. Magnenat-Thalmann. Anatomical modelling of the musculoskeletal system from MRI. *Proceedings of 9th International conference on medical image computing and computer assisted intervention (MICCAI'06)*, 4190:289–296, October 2006. 22

C. F. Gonzales, M. H. Becker, and J. C. Flanagan, editors. *Diagnostic Imaging in Ophthalmology*. Springer-Verlag: Berlin, 1986. ISBN 978-0-387-96140-8. 4

T. Haslwanter. Mechanics of eye movements: Implications of the "orbital revolution". *Annals of the New York Academy of Sciences*, 956:33–41, 2002. 2, 91

T. Haslwanter, M. Buchberger, T. Kaltofen, R. Hoerantner, and S. Priglinger. SEE++: Biomechanical model of the oculomotor plant. *Annals of the New York Academy of Sciences*, 1039:9–14, 2005. 7, 18, 94, 106

A. V. Hill. The heat of shortening and the dynamic constants of muscle. In *Proceedings of the Royal Society of London*, volume B126, pages 136–195. 1938. 96

R. Hoerantner, T. Kaltofen, S. Priglinger, C.M. Fock, M. Buchberger, and T. Haslwanter. Model based improvements in the treatment of patients with strabismus and axial high myopia. *Investigative Ophthalmology and Visual Science*, 48:1133–1138, 2007. 4

H. Hoppe, T. DeRose, T. Duchamp, J. McDonald, and W. Stuetzle. Surface reconstruction from unorganized points. *ACM SIGGRAPH 1992*, pages 71–78, 1992. 20

K. Hormann. Fitting free form surfaces. In B. Girod, G. Greiner, and H. Niemann, editors, *Principles of 3D Image Analysis and Synthesis*, The Kluwer International Series in Engineering and Computer Science, chapter 4.7, pages 192–202. Kluwer Academic Publishers, Boston, 2000. 31

M. R. Van Horn and K. E. Cullen. Dynamic characterization of agonist and antagonist oculomotoneurons during conjugate and disconjugate eye movements. *Journal of Neurophysiology*, 102:28–40, April 2009. 114

X. Huang, D. Metaxas, and T. Chen. Metamorphs: Deformable shape and texture models. *2004 IEEE Computer Society Conference on Computer Vision and Pattern Recognition (CVPR'04)*, 1:496–503, 2004. ISSN 1063-6919. 22, 27

M. Kass, A. Witkin, and D. Terzopoulos. Snakes: active contour models. *International Journal of Computer Vision*, 1(4):321–331, 1987. 21

R. Kono, R. A. Clark, and J. L. Demer. Active pulleys: Magnetic resonance imaging of rectus muscle paths in tertiary gazes. *Investigative Ophthalmology and Visual Science*, 43:2179–2188, 2002a. 4, 7, 13, 55, 91, 107, 124, 125, 138

R. Kono, V. Poukens, and J. L. Demer. Quantitative analysis of the structure of the human extraocular muscle pulley system. *Investigative Ophthalmology and Visual Science*, 43:2923–2932, 2002b. 13, 91, 101, 102, 146

G. K. Lang. *Ophthalmology: A Short Textbook*. Thieme Medical Publishers, 2000. 16

R. J. Leigh and D. S. Zee. *The Neurology of Eye Movements*. Oxford University Press, USA, 4 edition, 2006. 9

D. I.W. Levin, B. Gilles, B. Mädler, and D. K. Pai. A fiber tracking method for building patient specific dynamic musculoskeletal models from diffusion tensor data. *MICCAI Workshop on Computational Diffusion MRI*, pages 62–71, 2008. 49

Z. Li, C. Chui, Y. Cai, S. Amrith, P. Goh, J. H. Anderson, J. Teo, C. Liu, I. Kusuma, Y. Siow, and W. L. Nowinski. Modeling of the human orbit from MR images. *Proceedings of the 5th International Conference on Medical Image Computing and Computer-Assisted Intervention-Part II (MICCAI'02)*, 2489:339–347, 2002. 18, 20

K. H. Lim, V. Poukens, and J. L. Demer. Fascicular specialization in human and monkey rectus muscles: evidence for structural independence of global and orbital layers. *Investigative Ophthalmology and Visual Science*, 48:3089–3097, 2007. 125, 146

Y. Liu, H. Pottmann, and W. Wang. Constrained 3D shape reconstruction using a combination of surface fitting and registration. Technical report, Department of Computer Science, The University of Hong Kong, 2005. 22

C. Loop. *Smooth Subdivision Surfaces Based on Triangles*. Master's thesis, University of Utah, 1987. 51

W. E. Lorensen and H. E. Cline. Marching cubes: a high resolution 3D surface construction algorithm. *ACM Computer Graphics*, 21(4):163–169, 1987. 20

M. A. Lubinski, S. Y. Stanislav, K. R. Raghavan, A. E. Yagle, A. R. Skovoroda, and M. O'Donnell. Lateral displacement estimation using tissue incompressibility. *IEEE Transactions on Ultrasonics, Ferroelectrics, and Frequency Control*, 43(2):247–256, 1996. 57, 59

T. McInerney and D. Terzopoulos. Deformable models in medical image analysis: a survey. *Medical Image Analysis*, 1(2):91–108, 1996. 21

D. Metaxas and D. Terzopoulos. Shape and nonrigid motion estimation through physics-based synthesis. *IEEE Transactions on Pattern Analysis and Machine Intelligence*, 15(6):580–591, 1993. 21

J. M. Miller. Functional anatomy of normal human rectus muscles. *Vision Res.*, 29:223–240, 1989. 1, 4, 7, 13, 78, 91, 92

J. M. Miller. Understanding and misunderstanding extraocular muscle pulleys. *Journal of Vision*, 7(11):1–15, 2007. 2, 13, 103, 125, 129, 133

J. M. Miller and J. L. Demer. *Clinical Strabismus Management*, chapter Clinical Applications Of Computer Models For Strabismus, pages 100–105. Saunders, Philadelphia, 1999. 1

J. M. Miller, J. L. Demer, V. Poukens, D. S. Pavlovski, H. N. Nguyen, and E. A. Rossi. Extraocular connective tissue architecture. *Journal of Vision*, 3(3):240–251, 2003. 2, 18, 91, 101, 146

J. M. Miller, D. S. Pavlovski, and I. Shamaeva. *Orbit^{tm}* 1.8 gaze mechanics simulation. Eidactics, San Francisco, 1995, 1995. 7, 18, 24, 40, 94, 104, 106, 128

J. M. Miller and D. A. Robinson. A model of the mechanics of binocular alignment. *Computers and Biomedical Research*, 17(5):436–470, 1984. 7, 94

J. M. Miller, E. A. Rossi, M. Wiesmair, D. E. Alexander, and O. Gallo. Stability of gold bead tissue markers. *Journal of Vision*, 6(5):616–624, 2006. 5, 58, 74

K. L. Moore and A. F. Dalley. *Clinically Oriented Anatomy*. Lippincott Williams & Wilkins, 1999. 24

R. Muthupillai and R. L. Ehman. Magnetic resonance elastography. *Nature Medicine*, 2:601–603, 1996. 5, 57

D. O. Mutti, J. R. Hayes, G. L. Mitchell, L. A. Jones, M. L. Moeschberger, S. A. Cotter, R. N. Kleinstein, R. E. Manny, J. D. Twelker, and K. Zadnik. Refractive error, axial length, and relative peripheral refractive error before and after the onset of myopia. *Investigative Ophthalmology & Visual Science*, 48:2510–2519, 2007. 4, 49

T. O'Donnell, T. E. Boult, X. Fang, and A. Gupta. The extruded generalized cylinder: A deformable model for objectrecovery. *Proceedings of IEEE Computer Society of Computer Vision and Pattern Recognition (CVPR'94)*, pages 174–181, 1994. 59

S. Y. Oh, R. A. Clark, F. Velez, A. L. Rosenbaum, and J. L. Demer. Incomitant strabismus associated with instability of rectus pulleys. *Investigative Ophthalmology and Visual Science. 2002;43:2169-2178.*, 43:2169–2178, 2002. 4

N. F. Osman, W. S. Kerwin, E. R. McVeigh, and J. L. Prince. Cardiac motion tracking using cine harmonic phase (HARP) magnetic resonance imaging. *Journal of Magnetic Resonance Imaging*, 42(6):1048–1060, 1999. 5, 57

D. K. Pai, S. Sueda, and Q. Wei. Fast physically based musculoskeletal simulation. In *ACM Siggraph Sketches*. 2005. 97

X. Papademetris, A. J. Sinusas, D. P. Dione, R. D. Constable, and J. S. Duncan. Estimating 3D strain from 4D cine-MRI and echocardiography: In-vivo validation. *Medical Image Computing and Computer-Assisted Intervention (MICCAI 2000)*, (678-686), 2000. 58

G. P. Pappas, D. S. Asakawa, S. L. Delp, F. E. Zajac, and J. E. Drace. Nonuniform shortening the biceps brachii during elbow flexion. *Journal of Applied Physiology*, 92:2381–2389, 2002. 77

M. Piccirelli, R. Luechinger, A. K. Rutz, P. Boesiger, and O. Bergamin. Extraocular muscle deformation assessed by motion-encoded MRI during eye movement in healthy subjects. *Journal of Vision*, 7(10):1–10, 2007. 57, 75, 78, 110, 111, 112

G. Pokhai, K. Gordon, and M. Oliver. Development of a laser reflectance system to measure the cross-sectional area of soft tissue. *Meeting of North American Congress on Biomechanics*, 2008. 90

T. Popa, D. Julius, and A. Sheffer. Material-aware mesh deformations. *Proceedings of the IEEE International Conference on Shape Modeling and Applications 2006 (SMI06)*, page 22, 2006. 80

J. Porrill, P. A. Warren, and P. Dean. A simple control law generates listing's positions in a detailed model of the extraocular muscle system. *Vision Res*, 40:3743–3758, 2000. 94

J. D. Porter, R. S. Baker, R. J. Ragusa, and J. K. Brueckner. Extraocular muscles: basic and clinical aspects of structure and function. *Survey of Ophthalmology*, 39:451–484, 1995. 13

H. Pottmann and S. Leopoldseder. A concept for parametric surface fitting which avoids the parametrization problem. *Computer Aided Geometric Design*, 20:343–362, 2003. 31

E. Praun, W. Sweldens, and P. Schröder. Consistent mesh parameterizations. *ACM Transactions on Graphics (SIGGRAPH 2001)*, pages 179–184, 2001. 80

A. Qian, W. Lee, E. E. Konofagou, D. N. Metaxas, and L. Axel. Ultrasound myocardial elastography and registered 3D tagged MRI: quantitative strain comparison. *Medical Image Computing and Computer-Assisted Intervention (MICCAI 2007)*, 1:800–808, 2007. 57

C. Quaia and L. M. Optican. Commutative saccadic generator is sufficient to control a 3-D ocular plant with pulleys. *J Neurophysiol*, 79:3197–3215, 1998. 7, 40, 93, 148

C. Quaia and L. M. Optican. Dynamic eye plant models and the control of eye movement. *Strabismum*, 11(1):17–31, 2003. 7, 93, 94

C. Quaia, X. Shan, J. Tian, H. Ying, L. M. Optican, M. Walker, R. Tamargo, and Zee D.S. Acute superior oblique palsy in the monkey: effects of viewing conditions on ocular alignment and modelling of the ocular motor plant. *Progress in Brain Research*, 171:47–52, 2008. 94, 106, 119, 120, 121

C. Quaia, H. S. Ying, A. M. Nichols, and L. M. Optican. The viscoelastic properties of passive eye muscle in primates. I: Static forces and step responses. *PLoS ONE*, 4(4):e4850, 2009a. 95, 96

C. Quaia, H. S. Ying, and L. M. Optican. The viscoelastic properties of passive eye muscle in primates. II: Testing the quasi-linear theory. *PLoS ONE*, 4(8):e6480, 08 2009b. 96

T. Raphan. Modeling control of eye orientation in three dimensions:i. role of muscle pulleys in determining saccadic trajectory. *Journal of Neurophysioly*, 79:2653–2667, 1998. 7, 93, 148

M. K. Reed and P. K. Allen. 3-D modeling from range imagery: An incremental method with a planning component. In *Image and Vision Computing*, volume 17, page 99111. 1999. 20

N. Reichek. MRI myocardial tagging. *Journal of Magnetic Resonance Imaging*, 10(5):609–616, 1999. 57

D. A. Robinson. The mechanics of human saccadic eye movement. *Journal of Physiology*, 174:245–264, 1964. 95, 96, 113

D. A. Robinson. A quantitative analysis of extraocular muscle cooperation and squint. *nvest Ophthalmol*, 14:801–825, 1975. 7, 92, 93, 96, 104, 106

D. A. Robinson. Models of the mechanics of eye movements. *Models of oculomotor behavior and control*, pages 21–41, 1981. 95, 96, 97, 101, 103, 104

D. A. Robinson, D. M. OMeara, A. B. Scott, and C. C. Collins. Mechanical components of human eye movements. *Journal of Applied Physiology*, 26(5):548–553, May 1969. 95, 96

S. Rusinkiewicz and M. Levoy. Efficient variants of the ICP algorithm. *Proceedings of the 3rd International Conference on 3-D Digital Imaging and Modeling (3DIM 2001)*, pages 145–152, 2001. 19

T. Rutar and J. L. Demer. "Heavy eye syndrome" in the absence of high myopia: a connective tissue degeneration in elderly strabismic patients. *Journal of American Association for Pediatric Ophthalmology and Strabismus*, 13(1):36–44, 2009. 4, 37, 140

O. Sadowsky, G. Chintalapani, and R. H. Taylor. Deformable 2D-3D registration of the pelvis with a limited field of view, using shape statistics. *Proceedings of the 10th International Conference on Medical Image Computing and Computer-Assisted Intervention (MICCAI'07)*, 4792:519–526, 2007. 21

K. Schittkowski. QL: A fortran code for convex quadratic programming - user's guide. Technical report, Department of Computer Science, University of Bayreuth, 2005. 83

C. Schnablok and T. Raphan. Modeling three-dimensional velocity to position transformation in oculomotor control. *Journal of Neurophysiology*, 71:623–638, 1994. 7, 40, 93

S. Schutte, S.ven P.W. van den Bedem, F. van Keulen, F. C.T. van der Helm, and H. J. Simonsz. A finite-element analysis model of orbital biomechanics. *Vision Research*, 46:1724–1731, 2006. 19, 39, 41, 80

X. Shan, J. Tian, H. S. Ying, C. Quaia, L. M. Optican, M. F. Walker, R. J. Tamargo, and D. S. Zee. Acute superior oblique palsy in monkeys: I. changes in static eye alignment. *Investigative Ophthalmology & Visual Science*, 48(6):2602–2611, June 2007a. 119

X. Shan, J. Tian, H. S. Ying, C. Quaia, L. M. Optican, M. F. Walker, R. J. Tamargo, and D. S. Zee. Acute superior oblique palsy in monkeys: II. changes in dynamic properties during vertical saccades. *Investigative Ophthalmology & Visual Science*, 48(6):2612–2620, June 2007b. 120, 121

A. Sheffer, E. Praun, and K. Rose. Mesh parameterization methods and their applications. *Foundations and Trends in Computer Graphics and Vision*, 2(2):105–171, 2006. 80

H. J. Simonsz and H. Spekreijse. Robinson's computerized strabismus model comes of age. *Strabismus*, 4(1):25–40, 1996. 94

K. D. Singh, N. S. Logan, and B. Gilmartin. Three-dimensional modeling of the human eye based on magnetic resonance imaging. *Investigative Ophthalmology and Visual Science*, 47:2272–2279, 2006. 18, 49

S. Sklavosa, J. Porrill, C. R.S. Kanekoc, and P. Dean. Evidence for wide range of time scales in oculomotor plant dynamics: Implications for models of eye-movement control. *Vision Research*, 45(12):15251542, June 2005. 95

T. Srinark and C. Kambhamettu. Multiple snakes: a guiding scheme for object segmentation. *Asian Conference on Computer Vision*, January 27-30 2004. 22

S. Sueda, A. Kaufman, and D. K. Pai. Musculotendon simulation for hand animation. *ACM Trans. Graph. (Proc. SIGGRAPH'08)*, 27(3), 2008. 39, 80, 97, 99, 105

P.A. Sylvestre and K. E. Cullen. Quantitative analysis of abducens neuron discharge dynamics during saccadic and slow eye movements. *J Neurophysiol*, 82:2612–2632, 1999. 106, 113, 114

D. Terzopoulos, J. Platt, A. Barr, , and K. Fleischer. Elastically deformable models. *Computer Graphics (Proc. SIGGRAPH87)*, 21(4):205–214, 1987. 21

S. Tian, Yasuhiro Nishida, Bengt Isberg, and Gunnar Lennerstrand. MRI measurements of normal extraocular muscles and other orbital structures. In *Graefe's Archive for Clinical and Experimental Ophthalmology*, volume 238, pages 393–404. 2000. 4

G. M. Treece, R. W. Prager, and A. H. Gee. Regularised marching tetrahedra: improved iso-surface extraction. *Computers & Graphics*, 23(4):583–598, 1999. 21

C. L. Trestik and R. L. Lieber. Relationship between achilles tendon mechanical properties and gastrocnemius muscle function. *Journal of Biomechanical Engineering*, 115(3):225–230, 1993. 58, 59

D. B. Tweed and T. Vilis. Implications of rotational kinematics for the oculomotor system in three dimensions. *J Neurophysiol*, 58:823–849, 1987. 40

D. Tweedw, E. Adera, and T. Ile. Computing three-dimensional eye position quaternions and eye velocity from search coil signals. *Vision Research*, 30(1):97–110, 1990. 14

C. C. van Donkelaar, P. J. B. Willems, A. M. M. Muijtjens, and M. R. Drost. Skeletal muscle transverse strain during isometric contraction at different lengths. *Journal of Biomechanics*, 32(8):755–762, 1999. 58, 59

F. G. Velez, N. Thacker, M. T. Britt, and A. L. Rosenbaum. Cause of v pattern strabismus in craniosynostosis: a case report. *British Journal of Ophthalmology*, 88(12):15981599, December 2004. 4

G. K. von Noorden and E. C. Campos. *Binocular Vision and Ocular Motility: Theory and Management of Strabismus*. Mosby, 6 edition, 2001. 2, 9, 10, 12, 15, 16, 24, 119, 128, 131, 134, 135

X. Wang, T. Chen, S. Zhang, D. N. Metaxas, and L. Axel. LV motion and strain computation from tMRI based on meshless deformable models. *Medical Image Computing and Computer-Assisted Intervention (MICCAI 2008)*, pages 636–644, 2008. 58

Q. Wei and D. K. Pai. Physically consistent registration of extraocular muscle models from MRI. *Proceedings of 30th Annual International Conference of the IEEE Engineering in Medicine and Biology Society*, pages 2237–2241, 2008. iv

Q. Wei and D. K. Pai. Longitudinal strain estimation in incompressible cylindrical tissues from magnetic resonance imaging. *In Proceedings of the 31st International Conference of the IEEE Engineering in Medicine and Biology Society*, pages 105–108, 2009. iv

Q. Wei, S. Sueda, J. M. Miller, J. L. Demer, and D. K. Pai. Subject-specific reconstruction of the human orbit from magnetic resonance images. *In Proceedings of the IEEE International Symposium on Biomedical Imaging*, pages 105–108, 2009. iv, 9

Q. Wei, S. Sueda, and D. K. Pai. A model of musculotendon dynamics of the human orbit in three dimensions. In *Abstract in the Society for Neuroscience Annual Meeting*. 2008. iv

Q. Wei, S. Sueda, and D. K. Pai. Biomechanical simulation of human eye movement, 2010. Submitted to the 5th International Symposium on Biomedical Simulation (ISBMS 2010). iv

W. Welch and A. Witkin. Variational surface modeling. *ACM Transactions on Graphics (SIGGRAPH 1992)*, pages 157–166, 1992. 83

R. S. Witte, K. Kim, B. J. Martin, and M. O'Donnell. Effect of fatigue on muscle elasticity in the human forearm using ultrasound strain imaging. *Proceedings of the 28th Annual International Conference of the IEEE Engineering in Medicine and Biology Society*, pages 4490–4493, 2006. 57

T. A. L. Wren, S. A. Yerby, G. S. Beaupre, and D. R. Carter. Mechanical properties of the human achilles tendon. *Clinical Biomechanics*, 16(3):245–251, 2001. 58, 59

J. Xie, H. T. Tsui, and D. Xia. Multiple objects segmentation based on maximum-likelihood estimation and optimum entropy-distribution (mle-oed). *Proceedings of 16th International Conference on Pattern Recognition (ICPR'02)*, 1:707–710, 2002. 22

L. Yoo, H. Kim, V. Gupta, and J. L. Demer. Quasi-linear viscoelastic behavior of bovine extra-ocular muscle tissue. *Investigative Ophthalmology and Visual Science*, 50:3721–3728, 2009. 96

H.K. Zhao, S. Osher, and R. Fedkiw. Fast surface reconstruction using the level set method. *VLSM Workshop*, page 194, 2001. 20

X. Zhong, F. H. Epstein B. S. Spottiswelde, P. A. Helm, and S.S. Blemker. Imaging two-dimensional displacements and strains in skeletal muscle during joint motion by cine DENSE MR. *Journal of Biomechanics*, 41(3):532–540, 2008. 58

Vita

Qi Wei

2001–2004 M. Sc. in Computer Science from the University of British Columbia

1997–2001 B. E. in Computer Engineering from Beijing Institute of Technology

2007–08 Visiting Scholar, Department of Computer Science, The University of British Columbia

2004–08 Graduate/Teaching assistant, Department of Computer Science, Rutgers University

2001–03 Research/Teaching assistant, Department of Computer Science, The University of British Columbia

Publications

Q. Wei, S. Sueda, and D. K. Pai. Biomechanical Simulation of Human Eye Movement. *To Appear in Proceedings of the 5th International Symposium on Biomedical Simulation (ISBMS 2010)*, 2010.

Q. Wei and D. K. Pai. Longitudinal Strain Estimation in Incompressible Cylindrical Tissues from Magnetic Resonance Imaging. *In Proceedings of the 31st International Conference of the IEEE Engineering in Medicine and Biology Society*, 2009.

Q. Wei, S. Sueda, J. M. Miller, J. L. Demer, and D. K. Pai. Subject-specific Reconstruction of the Human Orbit from Magnetic Resonance Images. *In Proceedings of the IEEE International Symposium on Biomedical Imaging*, pages 105–108, 2009.

Q. Wei and D. K. Pai. Physically Consistent Registration of Extraocular Muscle Models From MRI. *Proceedings of 30th Annual International Conference of the IEEE Engineering in Medicine and Biology Society*, pages 2237–2241, 2008.

Q. Wei, S. Sueda, and D. K. Pai. A model of musculotendon dynamics of the human orbit in three dimensions. *Abstract in the Society for Neuroscience Annual Meeting*, 2008.

D. K. Pai, S. Sueda, and Q. Wei. Fast physically based musculoskeletal simulation. *ACM Siggraph Sketches*, 2005.

T. Edmunds, D. Kaufman, P.G. Kry, D.K. Pai, S. Sadhukhan, S. Sueda, D. Wang, and Q. Wei. Interactive Character Animation with Vision. In *SCA '04: Poster Proceedings of the 2004 ACM SIGGRAPH/Eurographics Symposium on Computer Animation*, pages 42–43. 2004.